Quantitative Modelling of the Shifts and Splitting in the IR Spectra of SF_6 in an Ar Matrix

by

Tao Peng

A thesis
presented to the University of Waterloo
in fulfilment of the
thesis requirement for the degree of
Master of Science
in
Chemistry

Waterloo, Ontario, Canada, 2005

I hereby declare that I am the sole author of this thesis.

This is a true copy of the thesis, including any required final revisions, as accepted by my examiners.

I understand that my thesis may be made electronically available to the public.

Abstract

An infrared active polyatomic molecule has several vibrational modes, each of which has a characteristic frequency. If the molecule is trapped in a matrix of perturbing atoms, those vibrational frequencies will shift, and if the vibrational mode is degenerate, the perturbation may lift the degeneracy. Such shifts and splitting are due to the dependence of the chromophore/matrix-atom interaction potential on the internal vibrational motion of the chromophore. Applying a previously-developed model for the shifting and splitting of the triply degenerate ν_3 mode of SF_6 perturbed by a rare gas atom, we use Monte Carlo simulations to sample the accessible equilibrium configurations of the system and to predict the associated thermally averaged perturbed IR spectra. Since the experimental spectrum has 10 peaks while the triply degenerate ν_3 mode of SF_6 in a particular environment could have at most 3 peaks, the observed spectrum must be a combination of spectra for SF_6 trapped in different types of lattice sites. A fit to experiment of simulated spectra generated from a family of lattice sites is then used to identify the peaks in the experimental spectrum, determine the relative importance of the various lattice sites, and semi-quantitatively reproduce the experimental spectrum.

Acknowledgements

Many thanks to my supervisor Dr. Robert J. Le Roy. When I entered this university two years ago, I was an absolute rookie in the area of theoretical chemistry. It is Dr. Le Roy who gives me much guidance and inspires me to move forward. I learned a lot from him, not only the knowledge of computational chemistry, but also the attitude and enthusiasm to explore the unknown world. He also helped me to settle down at this new country and to get accustomed to western culture.

Dr. Deiter Eichenauer and Dr. Robert J. Le Roy laid the ground work for this study in their earlier work on the SF_6-$(Ar)_n$ clusters. Jeffrey J. Sylvestre's earlier work also gave me much help.

I must also thank Dr. Peter F. Bernath who has been a great help to me. Attending his lectures is a great pleasure. Thanks also go to Dr. Marcel Nooijen for his great help and guidance during the last two years. I am deeply impressed by his broad and profound knowledge of chemical and mathematical theories. I would also like to thank Dr. Frederick R. W. McCourt who provided me with a lot of help in my research.

The theoretical chemistry group at the University of Waterloo must be thanked and acknowledged for all the help I have received from them. In particular, I would like to thank Yiye Huang, Marjan Mohammadi and Dr. Hua Wei for all their help of both a scientific and personal nature.

The biggest thank you goes to my parents. Their tremendous understanding, encouragement, guidance and support have made this thesis possible.

Contents

List of Tables

List of Figures

Chapter 1

Introduction

Since their inception, matrix-isolation techniques for producing and trapping chemical species have been applied to a wide range of chemical and physical problems [1]. This methodology was originally developed as a way of trapping species, especially free radicals, ions, metal clusters, and unstable molecules, in an inert cryogenic environment where their properties may be studied usually using spectroscopic methods. When molecular diffusion is repressed, which can be achieved by decreasing the temperature well below the melting point of the host matrix atoms, the complicating effects of intermolecular interactions, molecular rotation, and reactivity are also suppressed [1, 2, 3]. The low temperatures employed result in fairly rigid matrix environments in which rotational structure and hot bands present for gaseous systems are largely eliminated. As a result, the spectra of matrix-isolated species are generally fairly sharp, and due to the "pressure broadening" caused by the matrix atoms, the observed transitions have Lorentzian line shapes.

The first application of matrix-isolation techniques was Lewis's studies of aromatic molecules doped into a rigid glassy solid [4, 5]. Pimentel [1] and Porter [2] were the first to apply matrix-isolation methods using rare gas and N_2 solids in order to stabilize transient species. Initially, the trapped species studied were unstable molecules. In the 1980's the range of transient species studied in this way was extended to include metal clusters [6] and ions [7], as well as radicals, high temperature species, and photochemical reaction products. Thanks to the development of high resolution infrared spectroscopy, the behavior of SF_6 in rare gas matrices was examined by Swanson and Jones [3, 8, 9, 10, 11, 12].

The underlying premise in many MIS (Matrix-Isolated System) studies is that guest-host interactions are minimal, and therefore that the molecular properties of the trapped species should be very similar to those in the gas phase. For most systems, especially stable molecules isolated in rare gas lattices, this approximation is reasonable. In fact, the vibrational frequencies obtained for molecules isolated in neon

matrices, for which the shifts are usually small, are sometimes more reliable than those obtained from gas phase studies where rovibrational structure and hot bands complicate the spectra [3]. Matrix studies of several diatomics and a few other small molecules have shown evidence for rotational sub-structure, indicating that the intermolecular potentials hindering molecular rotation may be quite small [13]. Experimental results and the theories developed to explain molecular rotation in matrices have been reviewed by Hallam [14] and Barnes [15].

While the guest-host interactions are weak, they perturb the trapped species in many ways. First, the vibrational frequencies and energies of electronic transition are rarely the same for a matrix-isolated molecule as they are in the gas phase. Second, since the energy levels of the trapped particle are perturbed, its characteristic vibrational transition frequencies are shifted. The gas-to-matrix frequency shifts for molecular vibrations can be quite large even for very stable species such as the hydrogen halides [15]. Perutz and Turner showed that direct interactions between a photo-product and a host matrix would often occur, thereby giving rise to substantial perturbation of the electronic states [16].

A more subtle matrix effect is the occurrence of multiple trapping sites, each with its own discrete molecular spectrum. The electronic transitions can be significantly perturbed. For example, Davies *et al.* showed that $Fe(CO)_4$ occupies several discrete sites in N_2 and Ar matrices, and that infrared laser-induced rearrangement is site selective [17].

Guest-host interactions can also give rise to a splitting of degenerate modes because the symmetry of the trapping site is lower than that experienced by the isolated molecule. With improvements in experimental instrumentation, particularly the increased resolution and decreased time required to obtain high-quality spectra over a large spectral region, it becomes possible to separate the effects of multiple trapping sites from the possible occurrence of a site symmetry splitting. Hallam [14] has provided an excellent early review of matrix effects, and Barnes [15] has discussed the theories which have been developed to model matrix-molecule interactions.

In the early years, the vibrational spectroscopic studies of matrix effects were limited by the spectral resolution employed (typically 1 cm^{-1}). In the late 1970's and 1980's, high resolution infrared studies were performed using diode laser and Fourier transform systems. Those experimental results have shown that matrix-molecule interactions can be very complex. Gunthard and Dubbs [18, 19] pioneered the use of diode laser spectrometers in studying matrix-isolated molecules. In addition to obtaining accurate line shapes [18], they were able to observe hole burning for one isomer of trans-difluoroethane isolated in argon [19]. This kind of high resolution experiment offers a direct means of obtaining the homogeneous line shapes, and by

Table 1.1: Character Table for O_h molecules (From Ref. [23]).

O_h	$\hat{\mathrm{E}}$	$8\hat{\mathrm{C}}_3$	$3\hat{\mathrm{C}}_2$	$6\hat{\mathrm{C}}_4$	$6\hat{\mathrm{C}}_2'$	$\hat{\mathrm{i}}$	$8\hat{\mathrm{S}}_6$	$3\hat{\sigma}_h$	$6\hat{\mathrm{S}}_4$	$6\hat{\sigma}_d$		
A_{1g}	1	1	1	1	1	1	1	1	1	1		$x^2+y^2+z^2$
A_{2g}	1	1	1	-1	-1	1	1	1	-1	-1		
E_g	2	-1	2	0	0	2	-1	2	0	0		$(2z^2-x^2-y^2, x^2-y^2)$
$\mathrm{T}_{1g}(\mathrm{F}_{1g})$	3	0	-1	1	-1	3	0	-1	1	-1	(R_x, R_y, R_z)	
$\mathrm{T}_{2g}(\mathrm{F}_{2g})$	3	0	-1	-1	1	3	0	-1	-1	1		(xy, xz, yz)
A_{1u}	1	1	1	1	1	-1	-1	-1	-1	-1		
A_{2u}	1	1	1	-1	-1	-1	-1	-1	1	1		
E_u	2	-1	2	0	0	-2	1	-2	0	0		
$\mathrm{T}_{1u}(\mathrm{F}_{1u})$	3	0	-1	1	-1	-3	0	1	-1	1	(x, y, z)	
$\mathrm{T}_{2u}(\mathrm{F}_{2u})$	3	0	-1	-1	1	-3	0	1	1	-1		

comparison with the absorption line shapes, obtaining information concerning inhomogeneous broadening. Bristow *et al.* [20] have also used high resolution absorption spectra obtained using laser diode spectrometers as a means of unravelling matrix-molecule dynamics.

The system that will be discussed here is a model for SF_6 in an Ar matrix. The SF_6 molecule possesses O_h symmetry. Consequently, from the relevant character table (Table 1.1) and appropriate selection rules, it can be seen that such a structure will give rise to one non-degenerate A_{1g} vibration (ν_1), one doubly degenerate E_g vibration (ν_2), two triply degenerate T_{1u} vibrations (ν_3, ν_4), one triply degenerate T_{2g} vibration (ν_5), and one triply degenerate T_{2u} vibration (ν_6). The character table shows that the T_{1u} vibrations are infrared active and the A_{1g}, E_g, and T_{2g} vibrations are Raman active, while the T_{2u} vibration is inactive both in the Raman effect and the infrared. The ν_1, ν_2, and ν_3 modes are associated with bond stretching vibrations, and ν_4, ν_5, and ν_6 with deformational vibrations [21]. Fig. 1.1 illustrates the normal mode motions of SF_6 [22].

Since SF_6 has seven nuclei, it has $3N-6 = 3\times 7-6 = 15$ vibrational modes. Attention in this project is focussed on the triply degenerate ν_3 mode (asymmetric F-S-F stretch) [21], for which the characteristic fundamental band transition energy is 948 cm^{-1} [24, 22]. As mentioned earlier, one may expect the host environment to shift the transition frequency and split it into at most three components.

Swanson and Jones employed an FTIR spectrometer capable of 0.035 cm^{-1} resolution to study several high symmetry molecules in a variety of host matrices [8, 10, 11, 12, 25, 26]. Fig. 1.2 shows their spectra for the ν_3 vibrational mode of SF_6 trapped in an Ar matrix, observed at 0.5 cm^{-1} and 0.035 cm^{-1} resolution. At 0.5 cm^{-1} resolution, a single asymmetric line is observed. When observed at 0.035 cm^{-1} resolution,

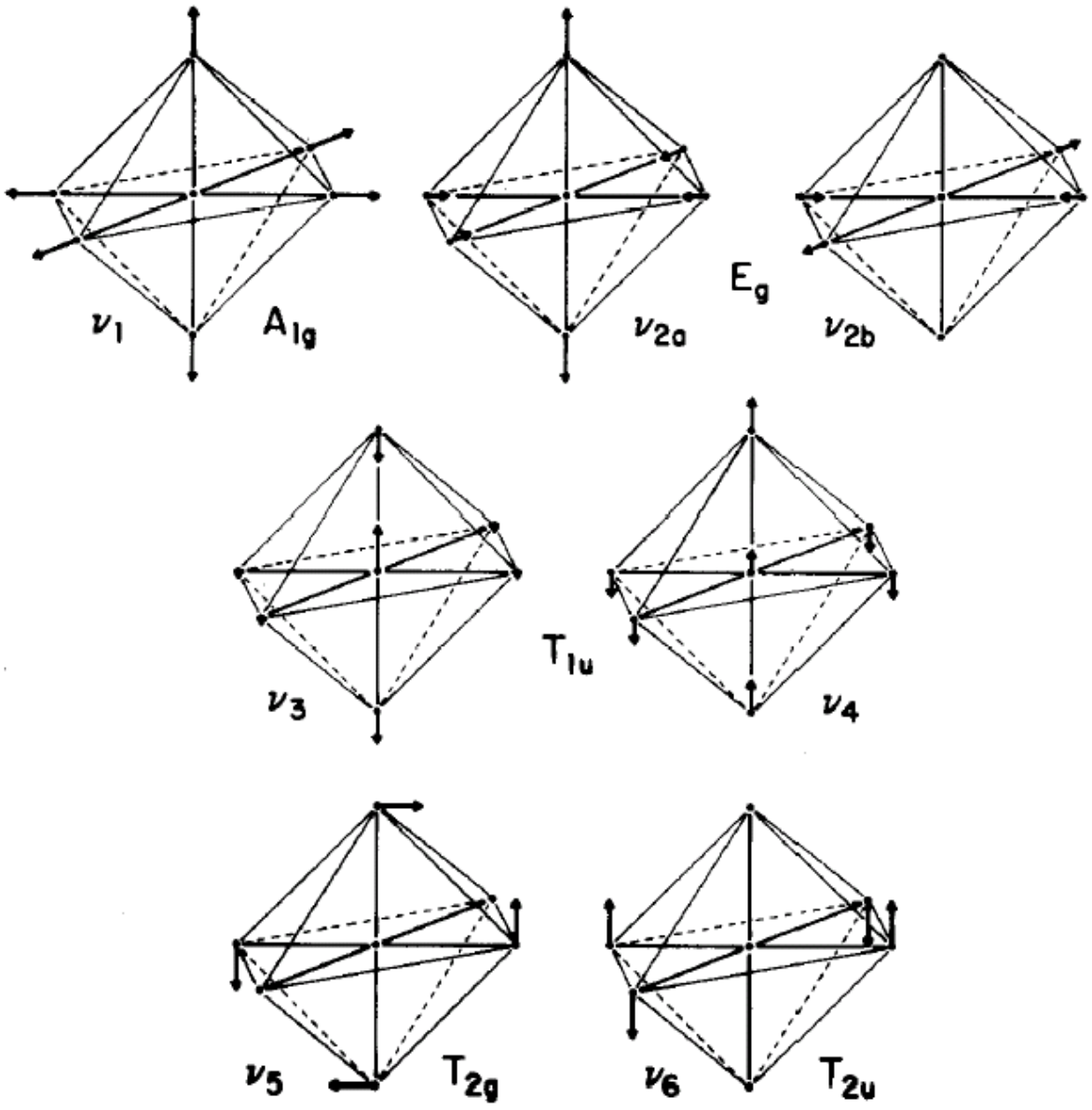

Figure 1.1: Normal modes of SF_6, showing the vector displacements of the nuclei. The two mutually orthogonal components of ν_2 are both shown. For the triply degenerate ν_3 - ν_6 modes, only one component is illustrated; in each case the other components are identical in form but are oriented orthogonally in space [22].

that single broad peak splits into several discrete sharp peaks.

Figure 1.2 shows that the host matrix causes the fundamental band transition frequency to shift from 948 cm^{-1} to the 938 cm^{-1} region. Moreover, under the high resolution condition, 9 peaks were observed, while at most 3 peaks were expected to arise from the the splitting of the triply degenerate ν_3 vibrational mode. Swanson and Jones believed that several distinct trapping sites, as well as site symmetry splittings gave rise to this phenomenon. By annealing the system at different temperatures, they tried to assign these peaks to several distinct sites and give a qualitative explanation for them [3]. However, due to the complexity of the system, they were not able to assign the peaks to particular vacancy sites, nor did they give an explanation for the composition of each peak or the population of any sites. To our knowledge, there has been no other published work addressing these questions.

The specific goal of this project is to attempt to explain quantitatively the high-resolution infrared spectrum of SF_6 in an argon matrix. We utilize a perturbation model introduced by Eichenauer and Le Roy [27] to simulate the infrared spectrum of SF_6 in an Ar matrix. Their model is based on a calculation of the energy shifts of the ground state and that of the first excited state, and the frequency shifts are obtained from the simple equation $\Delta\tilde{\nu}_i = (\Delta E_{1_i} - \Delta E_0) / h\,c$, where $i = 1, 2, 3$, representing the three components of this "triply degenerate" band. In order to obtain the values of the energy shifts, they treated the interaction between the chromophore molecule and the host atoms as the result of an instantaneous-dipole/induced-dipole (IDID) mechanism. They employed this model to predict the frequency shifts for $SF_6{-}(Ar)_n$ clusters and qualitatively compared their results with the experimental data [28, 29]. This model proved to be effective and efficient in interpreting the spectral behavior of molecules in clusters of helium [30, 31, 32, 33, 34, 35, 36, 37, 38], argon [39, 40, 41], and krypton [41, 42].

Chapter 2 will outline the perturbation theory description of level splitting, as well as the model utilizing the IDID mechanism. Argon atoms at low temperature form a face-centered cubic (FCC) configuration [43]. The edge length of a unit cell is 5.313 Å at 10 K [43], and the distance from the exterior of one fluorine atom to the exterior of the *trans* fluorine atom is about 6.2 Å [8]. It is clear that it would be difficult to admit an SF_6 into the matrix and avoid excess crowding without removing one or more argon atoms. The number of argon atoms removed, as well as the geometry of the vacancy sites may differ from one case to another. In the smallest vacancies with only zero or one argon atom removed, one can expect that the site would be highly crowded. On the other hand, if the number of the removed argon atoms becomes too large, the matrix vacancy tends to become unstable, and could collapse on annealing. For this reason, there is no need to study vacancy sites with large numbers of argon atoms removed. In this project, we

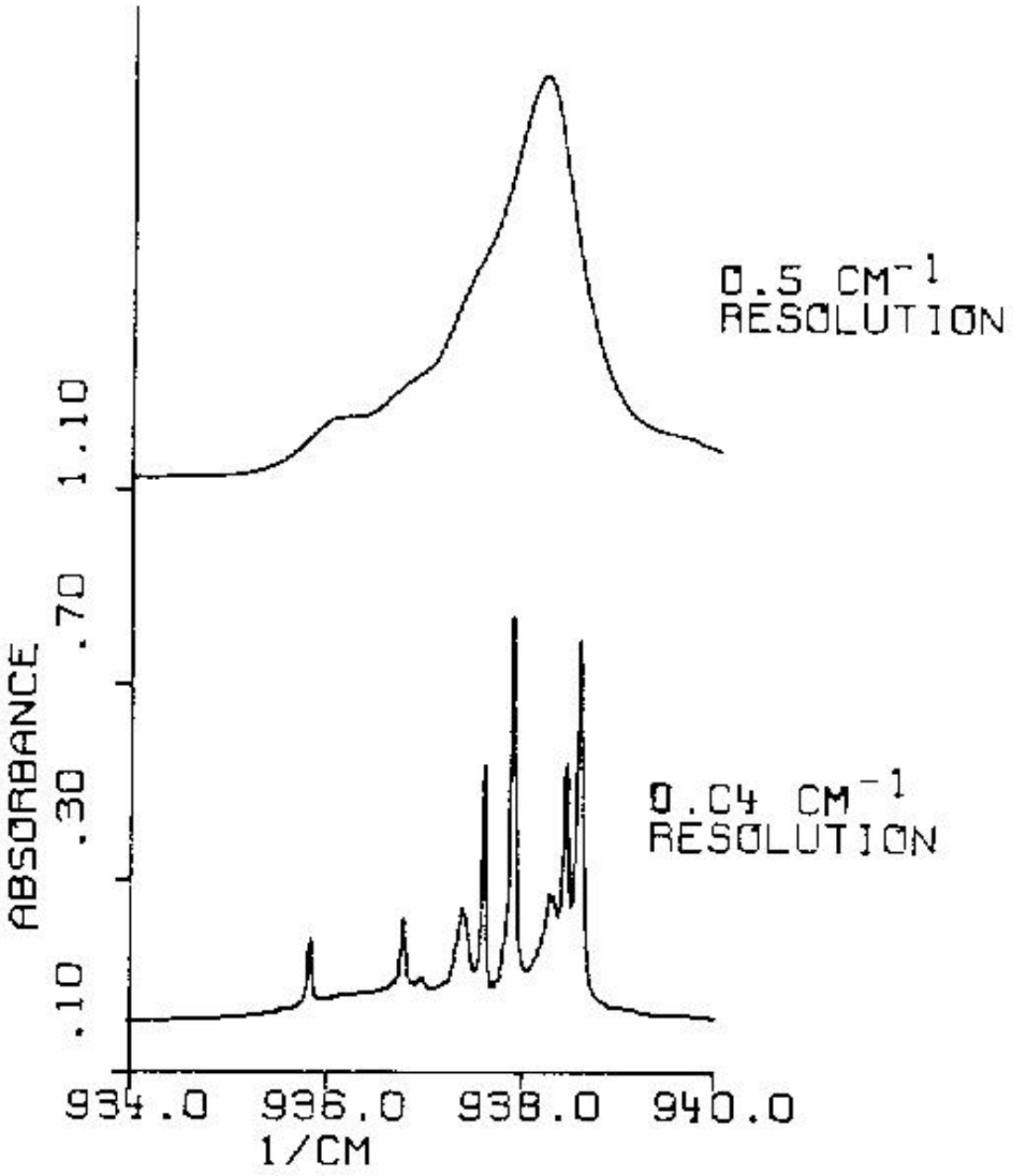

Figure 1.2: ν_3 region for $Ar/SF_6 = 10\,000$ at 9 K after 30 K anneal; 0.5 cm^{-1} vs. 0.035 cm^{-1} resolution [3].

examined vacancy sites for which the number of removed atoms varies from zero to six. More details will be presented in Chapter 4.

In order to simulate the behavior of the SF_6 molecule and the surrounding argon atoms, it is necessary to determine the most stable configuration of the system and to calculate the thermally averaged vibrational frequency shifts. We shall utilize the Monte Carlo (MC) method introduced by Metropolis *et al.* [44]. In the MC method, the first step is to randomly select one particle in the system, either the SF_6 molecule or an argon atom. We then move the selected particle in a random direction by a small randomly chosen distance; if it is the SF_6 molecule that is selected, it can also be rotated in random directions by small random angles. After each such move, the change in energy of the system is calculated and employed to decide whether or not the proposed move is to be accepted, based on the standard Metropolis MC acceptance criterion. This acceptance criterion ensures that after a sufficiently large number of moves, the results reproduce a Boltzmann distribution. We shall discuss these steps in detail in Chapter 4. Chapter 4 also presents some convergence tests of the parameters controlling the simulation.

It is clear from the previous discussion that it is necessary to calculate the potential energy of the system to carry out the Monte Carlo simulation and to determine the frequency shifts. The potential energy of the system is treated as the pairwise sum of the Ar-SF_6 and argon-argon interaction energies. Only two-body interactions were taken into account in our simulations. To calculate the Ar-SF_6 interaction potential, we employed an accurate anisotropic multiparameter M3SV (Morse-Morse-Morse-Spline-Van der Waals) potential model introduced by Pack *et al.* [45]. In order to save computing time, a simple form of Ar-Ar potential was utilized. Additional information on these potential models is presented in Chapter 3.

Chapter 5 will describe how the simulated spectra of SF_6 in an Ar matrix were obtained. After the system reached its stable configuration, at each Monte Carlo move, the three frequency shifts were obtained. After a large enough number of frequency shifts was collected, the simulation was ended. Chapter 5 also determines the spectrum for each vacancy site.

Because of the stochastic averaging associated with Monte Carlo simulation, the simulated spectra have Gaussian line shapes. Thus, simulated spectra were fitted to Gaussian functions to obtain the peak positions, peak height, and full width at half-maximum (FWHM). In contrast, the experimental spectrum has peaks with Lorentzian line shapes, due to the homogeneous "pressure" broadening caused by the perturbing matrix atoms [9]. Using the peak positions and relative intensities obtained by fitting a simulated spectrum to Gaussians, one can generate a Lorentzian-based spectrum for each vacancy site. A non-linear least-squares technique was then employed to fit the experimental spectrum to the Lorentzian spectra

generated for the various matrix sites considered. This fit allows us to assign the peaks in the experimental spectra and to determine the relative populations of the different types of vacancy sites. Chapter 6 will discuss the theory and details of these fits. Chapter 7 then presents a summary of and conclusions for the work presented in this thesis.

Chapter 2

Simulating matrix shifts

2.1 Perturbation theory

This section does not attempt to present a comprehensive exposition of perturbation theory, but rather to describe the essential features of this theory as it is used in this thesis. For a more complete discussion of this theory, readers are referred to Ref. [46].

Suppose the Schrödinger equation for the system of interest is

$$\hat{H}\,\Psi \;=\; E\,\Psi \tag{2.1}$$

and we are unable to solve this equation. Suppose also that there is a similar system with the relevant Schrödinger equation having the form

$$\hat{H}^{(0)}\,\Psi^{(0)} \;=\; E^{(0)}\,\Psi^{(0)} \tag{2.2}$$

and that this equation can be solved exactly; in other word, $\Psi^{(0)}$ and $E^{(0)}$ are known. We may write the Hamiltonian operator of Eq. 2.1 in the form

$$\hat{H} \;=\; \hat{H}^{(0)} \;+\; \hat{H}^{(1)} \tag{2.3}$$

in which the first term on the right side is the *unperturbed Hamiltonian operator* and the additional term is the *perturbation*. Standard first-order perturbation theory defines the *first-order correction* to $E^{(0)}$ to be

expressed as

$$E^{(1)} = \int \Psi^{(0)*} \hat{H}^{(1)} \Psi^{(0)} \, d\tau \tag{2.4}$$

Using Dirac notation [47], Eq. 2.4 can be expressed as

$$E^{(1)} = \left\langle 0 \left| \hat{H}^{(1)} \right| 0 \right\rangle \tag{2.5}$$

If the energy level E is d-fold degenerate, the first-order perturbation $E^{(1)}$ will be determined by solving

$$\begin{vmatrix} \left\langle 1 \left| \hat{H}^{(1)} \right| 1 \right\rangle - E^{(1)} & \left\langle 1 \left| \hat{H}^{(1)} \right| 2 \right\rangle & \cdots & \left\langle 1 \left| \hat{H}^{(1)} \right| d \right\rangle \\ \left\langle 2 \left| \hat{H}^{(1)} \right| 1 \right\rangle & \left\langle 2 \left| \hat{H}^{(1)} \right| 2 \right\rangle - E^{(1)} & \cdots & \left\langle 2 \left| \hat{H}^{(1)} \right| d \right\rangle \\ & & \cdots & \\ \left\langle d \left| \hat{H}^{(1)} \right| 1 \right\rangle & \left\langle d \left| \hat{H}^{(1)} \right| 2 \right\rangle & \cdots & \left\langle d \left| \hat{H}^{(1)} \right| d \right\rangle - E^{(1)} \end{vmatrix} = 0 \tag{2.6}$$

2.2 Harmonic-oscillator approximation and normal modes

2.2.1 Harmonic oscillator

Before introducing the perturbation model used to predict the spectral frequency shifts, we will briefly review the harmonic-oscillator approximation and normal modes. A concrete example of a single harmonic oscillator is a mass m coupled to a spring of force constant k. For small deformations x, the spring will exert the force given by Hooke's law, $F = -kx$, where k is the force constant, and give rise to a potential $V = kx^2/2$. The Hamiltonian for this system is

$$H = T + V = \frac{p^2}{2m} + \frac{1}{2} m\omega^2 x^2 \tag{2.7}$$

where $\omega = (k/m)^{1/2}$ is the classical angular frequency of oscillation. Any Hamiltonian of the above form, quadratic in the coordinate and momentum, is called a *harmonic oscillator Hamiltonian*. The Schrödinger equation for the quantum harmonic oscillator has the form

$$\left(-\frac{\hbar^2}{2m} \frac{d^2}{dx^2} + \frac{1}{2} m\omega^2 x^2 \right) \Psi = E \Psi \tag{2.8}$$

The solutions to this equation that lie in the physical Hilbert space are [48]

$$E = E_n = \left(n + \frac{1}{2}\right)\hbar\omega \tag{2.9}$$

$$\begin{aligned}\Psi &= \Psi_{E_n}(x) \equiv \Psi_n(x) \\ &= \left(\frac{m\omega}{\pi\hbar\, 2^{2n}\,(n!)^2}\right)^{1/4} \exp\left(-\frac{m\omega x^2}{2\hbar}\right) H_n\left[\left(\frac{m\omega}{\hbar}\right)^{1/2} x\right]\end{aligned} \tag{2.10}$$

in which $n = 0, 1, 2, \cdots$ labels the allowed energy levels for a quantum-mechanical harmonic oscillator, and $H_n(y)$, with $y = (m\omega/\hbar)^{1/2}\, x$, is an n'th order Hermite polynomial [46]. The energy is quantized and the wave functions are orthonormal.

From the Hermite polynomials $H_0(y) = 1$ and $H_1(y) = 2y$, one can obtain the wave functions for the ground state and the first excited state of the one-dimensional harmonic oscillator:

$$\Psi_0(x) = \left(\frac{\alpha}{\pi}\right)^{1/4} e^{-\alpha x^2/2} \tag{2.11}$$

$$\Psi_1(x) = \left(\frac{4\alpha^3}{\pi}\right)^{1/4} x\, e^{-\alpha x^2/2} \tag{2.12}$$

with $\alpha = (km/\hbar^2)^{1/2}$. For these wave functions,

$$\langle 0\,|x|\,0\rangle = \langle 1\,|x|\,1\rangle = 0 \tag{2.13}$$

2.2.2 Harmonic-oscillator approximation and normal coordinates

The vibrational spectrum of a polyatomic molecule may be readily understood if the molecule is thought of as a multi-dimensional harmonic oscillator. Consider a diatomic molecule whose equilibrium bond length is r_e. The potential energy $V(r)$ can be written as a Taylor series expansion

$$V(r) = V(r_e) + \left(\frac{dV}{dr}\right)_{r=r_e}(r - r_e) + \frac{1}{2!}\left(\frac{d^2V}{dr^2}\right)_{r=r_e}(r - r_e)^2 + \frac{1}{3!}\left(\frac{d^3V}{dr^3}\right)_{r=r_e}(r - r_e)^3 + \cdots \tag{2.14}$$

The first term on the right side of Eq. 2.14 is a constant and is usually chosen to be zero. Because the point $r = r_e$ is the minimum of the potential energy curve, the derivative $(dV/dr)_{r=r_e}$ vanishes. Therefore, the second term in Eq. 2.14 is also zero. Moreover, if the displacements are small, then $r - r_e$ will be small

and the terms beyond the quadratic term in Eq. 2.14 can be neglected, giving rise to the potential energy

$$V(r) = \frac{1}{2}\left(\frac{d^2V}{dr^2}\right)_{r=r_e}(r - r_e)^2 = \frac{1}{2}kx^2 \tag{2.15}$$

where $k = \left(d^2V/dr^2\right)_{r=r_e}$ and $x = r - r_e$. Eq. 2.15 shows that the general potential energy function $V(r)$ can be approximated by a harmonic-oscillator potential. The neglected high-order terms in Eq. 2.14 are called *anharmonic terms*.

The harmonic-oscillator approximation may also be applied to polyatomic molecules. If there are no external fields, the potential energy of a polyatomic molecule which contains N nuclei is a function of only the $3N - 5$ or $3N - 6$ vibrational coordinates. Denoting the displacement about the equilibrium values of these coordinates by $q_1, q_2, q_3, \cdots, q_{N_{vib}}$, where N_{vib} is the number of vibrational degrees of freedom, the potential energy is given by the multi-dimensional generalization of the one-dimensional case given by Eq. 2.14:

$$\begin{aligned}\Delta V &= V(q_1, q_2, \cdots, q_{N_{vib}}) - V(0, 0, \cdots, 0) = \frac{1}{2}\sum_{i=1}^{N_{vib}}\sum_{j=1}^{N_{vib}}\left(\frac{\partial^2 V}{\partial q_i \partial q_j}\right) q_i\, q_j \\ &= \frac{1}{2}\sum_{i=1}^{N_{vib}}\sum_{j=1}^{N_{vib}} f_{ij}\, q_i\, q_j \end{aligned} \tag{2.16}$$

in which the f_{ij} are quadratic force constants. In general, there exist terms that contain higher powers of q_i, but such anharmonic terms will be neglected here. The presence of cross terms in Eq. 2.16 makes the corresponding Schrödinger equation difficult to solve. Following the procedure discussed in Chapter 7 of Ref. [23], a new set of coordinates $\{Q_i\}$ can be found for which Eq. 2.16 becomes

$$\Delta V = \frac{1}{2}\sum_{i=1}^{N_{vib}} F_i\, {Q_i}^2 \tag{2.17}$$

in which the cross terms have been eliminated. These new coordinates $\{Q_i\}$ are called normal coordinates and the vibrations associated with them are called normal modes.

In terms of normal coordinates $\{Q_i\}$, the vibrational Hamiltonian may be written as

$$H_{vib} = \sum_{i=1}^{N_{vib}}\left(-\frac{\hbar^2}{2\mu_i}\frac{d^2}{dQ_i^2} + \frac{1}{2}F_i\, Q_i^2\right) \tag{2.18}$$

Since this Hamiltonian operator is written as a sum of independent terms, the total wave function is a

product of individual wave functions, and the energy is a sum of independent energies [46]

$$\Psi_{vib}\left(Q_1, Q_2, \cdots, Q_{N_{vib}}\right) = \Psi_{vib,1}\left(Q_1\right)\Psi_{vib,2}\left(Q_2\right)\cdots\Psi_{vib,N_{vib}}\left(Q_{N_{vib}}\right) \quad (2.19)$$

$$E_{vib} = \sum_{i=1}^{N_{vib}} h\nu_i\left(v_i + \frac{1}{2}\right) \quad \text{each } v_i = 0, 1, 2, \cdots \quad (2.20)$$

The practical consequence of introducing normal coordinates is that under the harmonic-oscillator approximation, the vibrational motion of a polyatomic molecule will appear as N_{vib} independent harmonic oscillators, with each normal mode having its own characteristic fundamental frequency ν_i if there is no degeneracy.

2.3 Frequency shifts of the ν_3 band of SF_6

SF_6 is an octahedral molecule. Eichenauer and Le Roy have developed a perturbation model which can be used to predict spectral frequency shifts for the vibrations of the SF_6 in an $SF_6-(Rg)_n$ clusters [27]. Interest here is focused on the ν_3 vibrational mode. This mode is an asymmetric stretching vibration in which the sulfur atom moves in one direction along one of the F−S−F axes, and all the fluorine atoms move in the opposite direction (See Fig. 2.1). In the absence of any perturbing forces, the ν_3 vibrational mode is triply degenerate, since the stretching motion may be along either the *x, y* or *z* axes. We choose a coordinate system with the center of mass of SF_6 defining the origin and the S−F bonds aligned along the *x, y* and *z* axes. For the *z* component of the triply-degenerate ν_3 vibrational mode, the displacement of the atoms of the chromophore during a vibrational motion is illustrated in Fig. 2.1. Each atom oscillates about its equilibrium position with the same frequency and phase, but the sulfur atom and fluorine atoms have different amplitudes of oscillation. The model for the simulated spectral shifts developed by Eichenauer and Le Roy is presented briefly below.

The eigenstates of interest here are the ground state, which is denoted by $|0\rangle$, and the three degenerate first excited vibrational states $|1_i\rangle$, where $i = 1, 2, 3$ represent antisymmetric stretching motion along the *x, y* and *z* molecular axes, respectively. Fig. 2.2 illustrates the shifts and splitting of the triply degenerate ν_3 transition of an SF_6 surrounded by several argon atoms. The fundamental transition frequency of a free SF_6 molecule in the gas phase is 948 cm^{-1} [24, 22]. On trapping the SF_6 molecule in an Ar matrix, both the ground state and the first excited state energy levels are shifted. A larger lowering of the vibrationally excited level(s) leads to a net red shift. The values of these energy level shifts are necessary to calculate

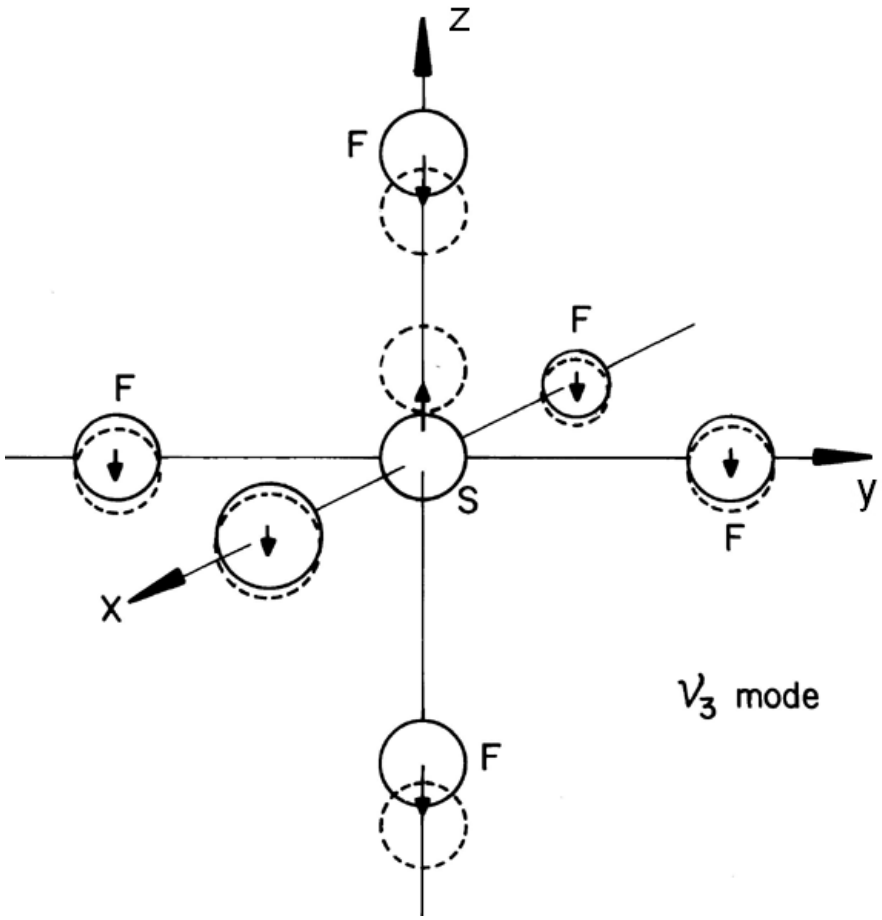

Figure 2.1: Coordinate System and configuration of SF_6 molecule: solid circles denote the equilibrium positions and the dashed circles denote the displacements associated with the Z component of the ν_3 mode [22]. (From Ref. [27])

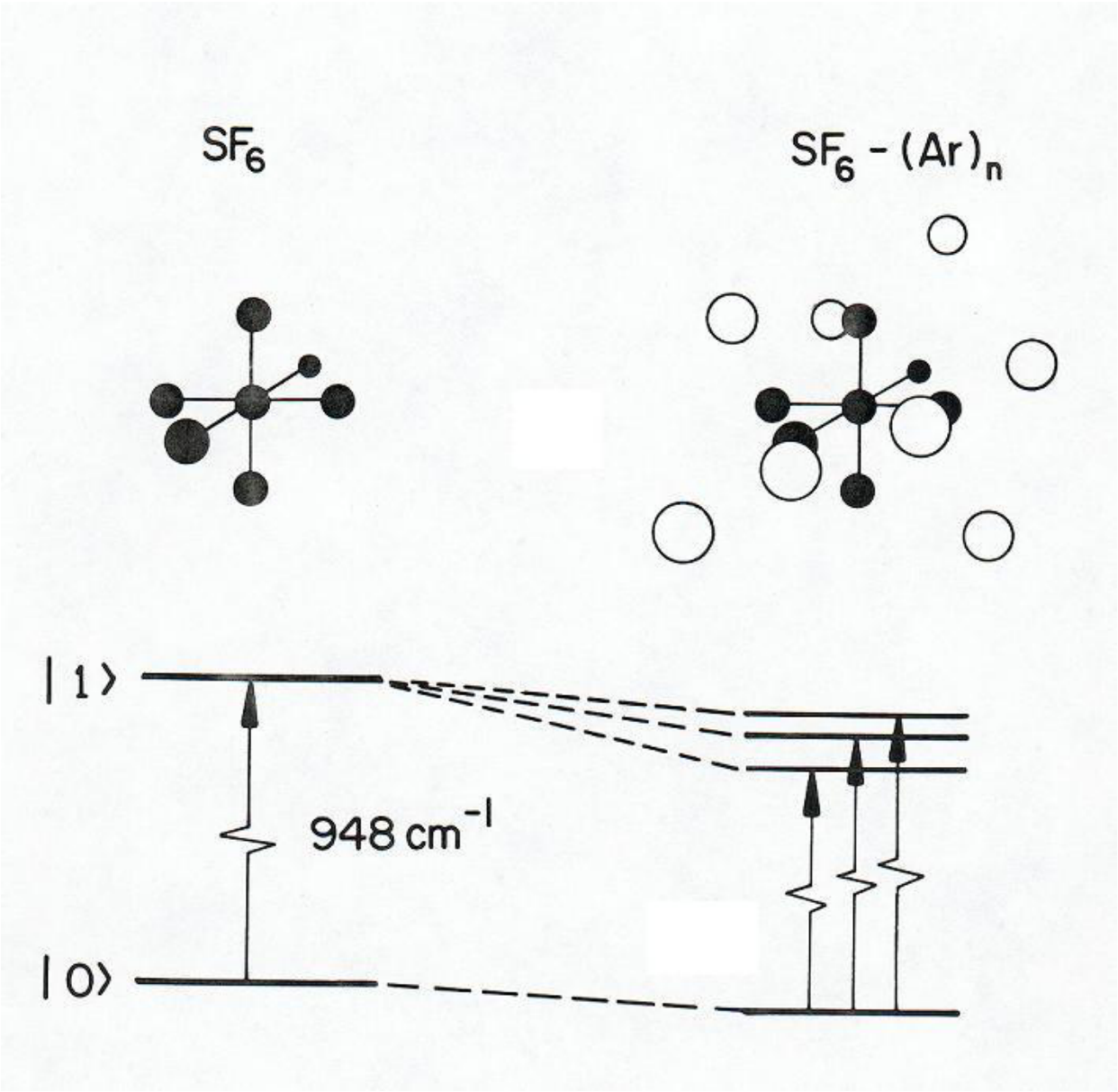

Figure 2.2: Schematic representation of the shifts and splitting of the triply degenerate ν_3 transition of SF_6 on formation of an $SF_6-(Ar)_n$ matrix. (From Ref. [27])

the frequency shifts.

From conventional first-order perturbation theory, the energy shift of the ground state is given by

$$E_0^{(1)} = \langle 0 \left| V_p \right| 0 \rangle \tag{2.21}$$

while for the first excited state of the triply degenerate band, the energy shifts $E_{1_i}^{(1)}$ (i = 1,2,3) are the roots of the characteristic equation

$$\begin{vmatrix} \langle 1_1 \left| V_p \right| 1_1 \rangle - E_{1_1}^{(1)} & \langle 1_1 \left| V_p \right| 1_2 \rangle & \langle 1_1 \left| V_p \right| 1_3 \rangle \\ \langle 1_2 \left| V_p \right| 1_1 \rangle & \langle 1_2 \left| V_p \right| 1_2 \rangle - E_{1_2}^{(1)} & \langle 1_2 \left| V_p \right| 1_3 \rangle \\ \langle 1_3 \left| V_p \right| 1_1 \rangle & \langle 1_3 \left| V_p \right| 1_2 \rangle & \langle 1_3 \left| V_p \right| 1_3 \rangle - E_{1_3}^{(1)} \end{vmatrix} = 0 \tag{2.22}$$

where $|0\rangle$ is the ground state, $|1_i\rangle$ (i = 1,2,3) are the first excited states, and V_p is the total perturbing potential. As is illustrated schematically in Fig. 2.2, the frequency shifts in the infrared spectrum then arise from the differences between the energy shifts of the $|1_i\rangle$ and $|0\rangle$ states,

$$\Delta\widetilde{\nu}_i = \left(E_{1_i}^{(1)} - E_0^{(1)}\right) / hc \tag{2.23}$$

and in order to solve Eqs. 2.21 – 2.23, V_p needs to be known.

If its anharmonicity and rotational degrees of freedom are neglected, the ν_3 mode of the SF_6 molecule may be treated simply as a three-dimensional harmonic oscillator. The total perturbing potential $V_p\left(\{\mathbf{R}_j\}, \{Q_i\}\right)$, is a function of the positions $\{\mathbf{R}_j\}$ $(j = 1, 2, \cdots, n)$ of the n Ar atoms in the matrix, and of the normal coordinates $\{Q_i\}\,(i = 1, 2, 3)$ that characterize the displacements of the sulfur and fluorine atoms within the SF_6 molecule. Three-body and higher-order interactions are neglected in this model, because the error of this pairwise potential approximation is expected to be much smaller than the uncertainty of the potential functions [27]. Therefore, the perturbing potential may be written as a sum over the individual Ar-SF_6 pair potentials:

$$V_p\left(\{\mathbf{R}_j\}, \{Q_i\}\right) = \sum_{j=1}^{n} V_j\left(\mathbf{R}_j, \{Q_i\}\right) \tag{2.24}$$

The maximum normalized, orthogonal displacements for the sulfur atom, for the two axial fluorine atoms, and for the four equatorial fluorine atoms are, respectively, 0.0458, -0.0320, and -0.0033 Å for the ν_3

vibrational mode [22]. Since the equilibrium value of the S−F bond length, 1.564 Å [49], is much larger than those intramolecular displacements, $V(\mathbf{R}_j, \{Q_i\})$ may be expanded in the form of Taylor series:

$$V_j(\mathbf{R}_j, \{Q_i\}) = V_0(\mathbf{R}_j) + \sum_{i=1}^{3} \frac{\partial V_j}{\partial Q_i} Q_i + \frac{1}{2} \sum_{i,k=1}^{3} \frac{\partial^2 V_j}{\partial Q_i \, \partial Q_k} Q_i \, Q_k + \cdots \tag{2.25}$$

in which $V_0(\mathbf{R}_j)$ is the pair potential when $\{Q_i\} = 0$, that is, when all the atoms are located in their equilibrium positions, and the additional terms reflect perturbation of the SF_6 energy levels due to interactions with the matrix atoms.

Because $V_0(\mathbf{R}_j)$ does not depend on the normal coordinates $\{Q_i\}$, its contribution to $E_0^{(1)}$ and $E_{1_i}^{(1)}$ is the same, and hence it has no effect on the $\Delta\nu_i$. Moreover, for any symmetric potential, $\langle 0 \,|Q_i|\, 0 \rangle = \langle 1_i \,|Q_i|\, 1_k \rangle = 0$. Thus, since the potential of a harmonic oscillator is symmetric and SF_6 is treated as a harmonic oscillator, the expectation values of the terms linear in Q_i, namely $\sum_{i=1}^{3} (\partial V_j \,/\, \partial Q_i) \, Q_i$, vanish. One can also obtain this result from the property of a harmonic oscillator: the average displacement of a harmonic oscillator is zero for all the quantum states of a harmonic oscillator (from Eq. 2.13). Similarly, the terms containing all higher odd powers of (products of) the Q_i have no contributions. It is therefore the quadratic term involving the products Q_iQ_k and the second derivatives of $V(\mathbf{R}_j, \{Q_i\})$ with respect to ν_3 stretching normal coordinates that provide the leading contribution to the shifting and splitting of the vibrational lines.

Eichenauer and Le Roy argued that higher-order perturbation theory terms, the anharmonicity of the SF_6 molecule, and higher-order terms in Eq. 2.25 would have little contribution to the frequency shifts [50]. Since the dependence of the SF_6−Ar intramolecular potential on the internal coordinates $\{Q_i\}$ was not well known, they estimated the importance of these assumptions using the potential energy surface of one of the few atom-molecule species for which a chromophore-stretching dependent potential energy surface is known [51]. The contributions arising from these approximations were a fraction of 1% of those due to the first-order quadratic terms for an Ar−H_2 system [50]. On these grounds, they argued that it was unlikely that such approximations would introduce significant errors into the case of Ar−SF_6.

In terms of the normal coordinates, a three-dimensional harmonic oscillator may be treated as a combination of three one-dimensional harmonic oscillators. The Hamiltonian of the three-dimensional harmonic may be written as

$$H = H_x + H_y + H_z$$

$$= \left(\frac{p_x^2 + p_y^2 + p_z^2}{2m}\right) + \frac{1}{2}m\omega^2\left(x^2 + y^2 + z^2\right) \tag{2.26}$$

with corresponding wave functions and eigenvalues given by

$$\Psi = \Psi_x\,\Psi_y\,\Psi_z \tag{2.27}$$

$$\begin{aligned} E &= E_x + E_y + E_z \\ &= \left(n + \frac{3}{2}\right)\hbar\omega \\ &= \left(n_x + \frac{1}{2}\right)\hbar\omega + \left(n_y + \frac{1}{2}\right)\hbar\omega + \left(n_z + \frac{1}{2}\right)\hbar\omega \end{aligned} \tag{2.28}$$

where $n = n_x + n_y + n_z;\ n_x, n_y, n_z = 0, 1, 2, \cdots$

Using Eqs. 2.11 − 2.12 and 2.26 − 2.28, one can obtain

$$\left\langle 0 \left| \sum_{i,k=1}^{3} \frac{\partial^2 V_j}{\partial Q_i \partial Q_k} Q_i Q_k \right| 0 \right\rangle = \frac{\hbar}{2\omega} \sum_{i=1}^{3} \frac{\partial^2 V_j}{\partial Q_i^2} \tag{2.29}$$

$$\left\langle 1_i \left| \sum_{i,k=1}^{3} \frac{\partial^2 V_j}{\partial Q_i \partial Q_k} Q_i Q_k \right| 1_k \right\rangle = \begin{cases} \dfrac{\hbar}{2\omega}\left(2\dfrac{\partial^2 V_j}{\partial Q_i^2} + \displaystyle\sum_{l=1}^{3} \frac{\partial^2 V_j}{\partial Q_l^2}\right) & i = k \\ 2\,\dfrac{\hbar}{2\omega}\dfrac{\partial^2 V_j}{\partial Q_i \partial Q_k} & i \neq k \end{cases} \tag{2.30}$$

in which ω is the angular frequency associated with the fundamental band of the ν_3 mode of the free SF_6 molecule ($\omega/2\pi c = 948\,\mathrm{cm}^{-1}$) [22]. The following equations may be generated from Eqs. 2.29 and 2.30:

$$\langle 0\,|V_j|\,0\rangle = V_0(\mathbf{R}_j) + \frac{\hbar}{4\omega} \sum_{i=1}^{3} \frac{\partial^2 V_j}{\partial {Q_i}^2} \tag{2.31}$$

$$\langle 1_i\,|V_j|\,1_k\rangle = V_0(\mathbf{R}_j)\,\delta_{i,k} + \frac{\hbar}{4\omega}\left(2\,\frac{\partial^2 V_j}{\partial Q_i \partial Q_k} + \delta_{i,k} \sum_{l=1}^{3} \frac{\partial^2 V_j}{\partial {Q_l}^2}\right) \tag{2.32}$$

By substituting Eqs. 2.31 and 2.32 into Eqs. 2.24, 2.21, 2.22, one may obtain the energy shifts of the ground state and the first-excited state due to a single perturbing Ar atom located at $\mathbf{R}_j$. Examining Eqs. 2.31 and 2.32, one can see that two terms needed to be determined. One term, $V_0\,(\mathbf{R}_j)$, is the rigid SF_6−Ar pair potential. More details of this potential will be discussed in Chapter 3. The other term, $\partial^2 V_j\,/\,\partial Q_i \partial Q_k$, was successfully described by using the IDID model introduced by Eichenauer and Le Roy [27].

2.4 The instantaneous-dipole/induced-dipole mechanism

SF_6 is an octahedral molecule. Due to this high symmetry, an SF_6 molecule has no dipole moment when all the atoms are at their equilibrium positions. Moreover, for vibrations governed by a symmetric (not necessarily harmonic) potential, such as that for the ν_3 mode, the average value of the dipole moment is zero. However, when the system is displaced from equilibrium in the course of the ν_3 vibrational motion, an instantaneous electric dipole moment arises. For small displacements, which is the case for the ν_3 vibration, the instantaneous electric dipole moment $\mathbf{p}$ may be approximated as a linear function of the displacement coordinates $\{\mathrm{Q}_i\}$:

$$\mathbf{p} = \left|\frac{\partial \mathbf{p}}{\partial Q}\right| \sum_{i=1}^{3} Q_i \, \hat{\mathbf{e}}_i \tag{2.33}$$

where the $\{\hat{\mathbf{e}}_i\}$ are unit vectors in the x, y, and z directions and the coefficient $|\partial \mathbf{p}/\partial Q|$ was determined from the measured intensity of the ν_3 band of an isolated SF_6 molecule to have a value of 226.1 esu $\mathrm{g}^{-1/2}$ ($e = 1.602062 \times 10^{-19}\,\mathrm{C} = 4.80287 \times 10^{-10}\,\mathrm{esu}$) [52].

The electric potential at a position $\mathbf{r}$ relative to this instantaneous dipole moment $\mathbf{p}$ is written as

$$U(\mathbf{r}, \mathbf{p}) = \frac{\mathbf{p} \cdot \mathbf{r}}{|\mathbf{r}|^3} = \frac{\mathbf{p} \cdot \hat{\mathbf{r}}}{r^2} = \frac{p \cos\theta}{r^2} \tag{2.34}$$

where $\mathbf{r}$ is the vector from the dipole with the length r, $\hat{\mathbf{r}}$ is the unit vector in the $\mathbf{r}$ direction, and θ is the angle between $\mathbf{p}$ and $\mathbf{r}$. The electric field of this dipole $\mathbf{p}$ is given by

$$\begin{aligned} \mathbf{E}(\mathbf{r}, \mathbf{p}) &= -\nabla U \\ &= -\nabla\left(\frac{\mathbf{p} \cdot \hat{\mathbf{r}}}{r^2}\right) = -\frac{1}{r^2}\nabla(\mathbf{p} \cdot \hat{\mathbf{r}}) - (\mathbf{p} \cdot \hat{\mathbf{r}})\,\nabla\left(\frac{1}{r^2}\right) \\ &= -\frac{1}{r^2}\nabla(\mathbf{p} \cdot \hat{\mathbf{r}}) + \frac{2\,(\mathbf{p} \cdot \hat{\mathbf{r}})\,\hat{\mathbf{r}}}{r^3} \end{aligned} \tag{2.35}$$

where the symbol ∇ is the usual vector operator

$$\nabla = \hat{\mathbf{e}}_1 \frac{\partial}{\partial x} + \hat{\mathbf{e}}_2 \frac{\partial}{\partial y} + \hat{\mathbf{e}}_3 \frac{\partial}{\partial z} \tag{2.36}$$

Because $\mathbf{p}$ is independent of $\hat{\mathbf{r}}$, $\nabla(\mathbf{p} \cdot \hat{\mathbf{r}})$becomes

$$\nabla(\mathbf{p} \cdot \hat{\mathbf{r}}) = \frac{\mathbf{p} - \hat{\mathbf{r}}\,(\mathbf{p} \cdot \hat{\mathbf{r}})}{r} \tag{2.37}$$

Substituting Eq. 2.37 into Eq. 2.35, one obtains

$$\begin{aligned} \mathbf{E}(\mathbf{r},\mathbf{p}) &= -\frac{1}{r^2}\,\frac{\mathbf{p}\,-\,\hat{\mathbf{r}}\,(\mathbf{p}\cdot\hat{\mathbf{r}})}{r}\,+\,\frac{2\,(\mathbf{p}\cdot\hat{\mathbf{r}})\,\hat{\mathbf{r}}}{r^3}\,=\,\frac{3\,(\mathbf{p}\cdot\hat{\mathbf{r}})\,\hat{\mathbf{r}}\,-\,\mathbf{p}}{r^3} \\ &= \frac{3\,(\mathbf{p}\cdot\mathbf{r})\,\mathbf{r}\,-\,r^2\,\mathbf{p}}{r^5} \end{aligned} \tag{2.38}$$

Therefore, the electric field at the positions $\mathbf{R}_j$ of Ar atom j is

$$\mathbf{E}(\mathbf{R}_j,\mathbf{p})\,=\,\left[3\,(\mathbf{R}_j\cdot\mathbf{p})\,\mathbf{R}_j\,-\,R_j^2\,\mathbf{p}\right]/R_j^5 \tag{2.39}$$

where $R_{j,i}\,=\,\mathbf{R}_j\cdot\hat{\mathbf{e}}_i$ denotes the i-th Cartesian component of the vector $\mathbf{R}_j$ in the molecule-fixed coordinate system of Fig. 2.1, and $R_j\,=\,|\mathbf{R}_j|$ is the distance from the j-th Ar atom to the center of mass of the SF_6 molecule. The dipole moment induced at the j-th Ar atom is simply $\alpha\mathbf{E}(\mathbf{R}_j,\mathbf{p})$, where α ($=\,1.642\,\text{Å}^3$) is the dipole polarizability of Ar atoms [53]. The interaction energy between this induced dipole moment at the j-th Ar atom and the instantaneous dipole moment at the SF_6 molecule is therefore

$$\begin{aligned} V^{int}(\mathbf{R}_j,\mathbf{p}) &= -\,\mathbf{p}^{id}\cdot\mathbf{E}\,=\,-\,\alpha\mathbf{E}\cdot\mathbf{E} \\ &= -\,\alpha\,|\mathbf{E}(\mathbf{R}_j,\mathbf{p})|^2 \end{aligned} \tag{2.40}$$

Substituting Eq. 2.39 into Eq. 2.40,

$$\begin{aligned} V^{int}(\mathbf{R}_j,\mathbf{p}) &= -\,\alpha\,|\mathbf{E}(\mathbf{R}_j,\mathbf{p})|^2 \\ &= -\,\alpha\left\{\left[3\,(\mathbf{R}_j\cdot\mathbf{p}_i)\,\mathbf{R}_j\,-\,R_j^2\,\mathbf{p}_i\right]\cdot\left[3\,(\mathbf{R}_j\cdot\mathbf{p}_k)\,\mathbf{R}_j\,-\,R_j^2\,\mathbf{p}_k\right]\right\}/R_j^{10} \\ &= -\,\frac{\alpha}{R_j^6}\left(3\,\frac{R_{j,i}R_{j,k}}{R_j^2}\,+\,\delta_{i,k}\right)\,p_i\,p_k \end{aligned} \tag{2.41}$$

The second-order partial derivative of $V^{int}(\mathbf{R}_j,\mathbf{p})$ with respect to the normal coordinates may be written as

$$\frac{\partial^2\,V^{int}}{\partial\,Q_i\partial\,Q_k}\,=\,-\,\frac{\alpha}{R_j^6}\left(3\,\frac{R_{j,i}R_{j,k}}{R_j^2}\,+\,\delta_{i,k}\right)\,\frac{\partial^2\,(p_i\,p_k)}{\partial\,Q_i\partial\,Q_k} \tag{2.42}$$

Eq. 2.33 defines $p_i\,=\,|\partial\,\mathbf{p}/\partial\,Q|\;Q_i$ and $p_k\,=\,|\partial\,\mathbf{p}/\partial\,Q|\;Q_k$, thus

$$\frac{\partial^2\,(p_i\,p_k)}{\partial\,Q_i\partial\,Q_k}\,=\,\left|\frac{\partial\,\mathbf{p}}{\partial\,Q}\right|^2 \tag{2.43}$$

so Eq. 2.42 becomes

$$\frac{\partial^2 V^{int}}{\partial Q_i \partial Q_k} = -\frac{\alpha}{R_j^6}\left(3\frac{R_{j,i}R_{j,k}}{R_j^2} + \delta_{i,k}\right)\left|\frac{\partial \mathbf{p}}{\partial Q}\right|^2 \tag{2.44}$$

This IDID interaction is taken to be the main vibrational stretching dependent contribution to the SF_6-Ar interactions [27]. Therefore, on replacing V_j in the derivatives in Eqs. 2.31 and 2.32 by V^{int} and substituting Eq. 2.44 into Eqs. 2.31 and 2.32, one obtains

$$\langle 0\,|V_j|\,0\rangle = V_0(\mathbf{R}_j) - \frac{\xi}{R_j^6} \tag{2.45}$$

$$\langle 1_i\,|V_j|\,1_k\rangle = V_0(\mathbf{R}_j)\,\delta_{i,k} - \frac{\xi}{R_j^6}\left(\frac{R_{j,i}R_{j,k}}{R_j^2} + \frac{4}{3}\delta_{i,k}\right) \tag{2.46}$$

where $\xi = 3\alpha\hbar\,|\partial\,\mathbf{p}/\partial\,Q|^2\,/2\omega = 0.4641$ eV·Å^6 is a constant.

Summing over all perturbing Ar atoms then allows Eqs. 2.21 - 2.23 to be used to calculate the vibrational frequency shifts and splitting pattern for any particular arrangement of perturbers. Examination of the secular determinant obtained by substituting Eq. 2.46 into Eq. 2.22 shows that the three eigenvalues $E_{1_i}^{(1)}$ $(i = 1, 2, 3)$ depend only upon relative positions of the Ar atoms and their distances from the center of mass of the SF_6 molecule. However, as described in Chapter 3, the overall potential energy depends not only on the distances from the Ar atoms to the sulfur atom, but also on the orientation and the position of the SF_6 molecule.

Chapter 3

Potential energy functions

3.1 Introduction

As discussed above, in order to calculate the values of level energy shifts, the rigid molecule−surrounding atoms potential, $V_0(\mathbf{R}_j)$, is the next term needed. Moreover, as we will see in Chapter 4, the potential energy is necessary in performing Monte Carlo simulations. In this chapter, we shall examine this potential in detail.

The overall potential energy of this matrix plus impurity system is a sum of two independent parts

$$V_0 = \sum_{j=1}^{n} V_{\mathrm{Ar}_j-\mathrm{SF}_6} + \sum_{i=1}^{n-1} \sum_{j=i+1}^{n} V_{\mathrm{Ar}_i-\mathrm{Ar}_j} \tag{3.1}$$

in which n is the number of the argon atoms in the model used for the matrix. The first term on the right side of Eq. 3.1 is the Ar−SF_6 interaction potential; it will be discussed in Section 3.2. The second term is the Ar−Ar interatomic potential, described in Section 3.3. No three-body or higher-order interactions are considered. This approximation is necessary to save computing time, and it is not expected to introduce significant errors into the calculations [27].

3.2 The Ar−SF_6 interaction potential

Pack *et al.* point out that although an SF_6 molecule is octahedral and is often treated as a heavy "spherical" perturber in experiments with other molecules, this is not true [45]. In particular, SF_6 is known to be rotationally relaxed rapidly by itself [54, 55] and by noble gases [56, 57], and some scattering experiments [58]

have shown some effects due to potential function anisotropy.

An early attempt to determine the anisotropic potential for an Ar−SF_6 system was reported by Isnard *et al.* [59, 60]. However, that model shows unphysical behavior and gives very poor results for properties other than the virial coefficient [45]. A better approximation to the strongly anisotropic atom plus rigid-molecule portion of this potential, $V_0(\mathbf{R}_j)$, was determined by Pack *et al.* [61] using the damping of oscillations in the total differential cross section (DCS), which is directly related to the potential anisotropy, in an analysis based on the infinite order sudden approximation (IOSA) [45, 62]. This section will discuss their anisotropic potential model in detail.

The SF_6–Ar interaction is sensitive to the relative orientation of Ar and SF_6. The intermolecular potential may be written in the form

$$V_0(R_j, \theta_j, \phi_j) = \sum_{l,m} v_{lm}(R_j)\, Y_{lm}(\theta_j, \phi_j) \tag{3.2}$$

in which $l = 0, 1, 2, \cdots$, $m = 0, \pm1, \pm2, \cdots, \pm l$, and the $v_{lm}(R_j)$ represents the radial parts of the potential with R_j being the distance from the center of mass of the SF_6 molecule to the j-th Ar atom. The angular part of the potential is represented by the spherical harmonic functions $Y_{lm}(\theta_j, \phi_j)$.

For the low energy collisions studied by Pack *et al.* [45, 62], vibrational excitation is very unlikely, so SF_6 can be treated as a rigid rotor. Following Ref. [45, 62], we employed a Morse-Morse-Morse-Spline-Van der Waals (M3SV) potential to calculate the Ar−SF_6 interaction energies. The M3SV potential is illustrated in Fig. 3.1. In regions i = I, II, and III, it is represented by Morse potentials

$$V_i(R) = \epsilon_i \left\{ \exp\left[-2\alpha_i \left(R - \mathrm{r_{mi}}\right)\right] - 2\exp\left[-\alpha_i \left(R - \mathrm{r_{mi}}\right)\right] \right\} \tag{3.3}$$

which are chosen so that they are continuous and have continuous first derivatives at the points at which they join. The first derivative of a Morse function V is

$$\frac{\partial V_i}{\partial R} = 2\,\alpha_i\,\epsilon_i\, e^{-\alpha_i(R - r_{mi})} \left[1 - e^{-\alpha_i(R - r_{mi})}\right] \tag{3.4}$$

Examining the first derivatives of the potentials at $\mathrm{r_m}$, the position of the overall potential minimum, one has

$$\left.\frac{\partial V_{\mathrm{II}}}{\partial R}\right|_{r_{\mathrm{m}}} = \left.\frac{\partial V_{\mathrm{III}}}{\partial R}\right|_{r_{\mathrm{m}}} = 0 \tag{3.5}$$

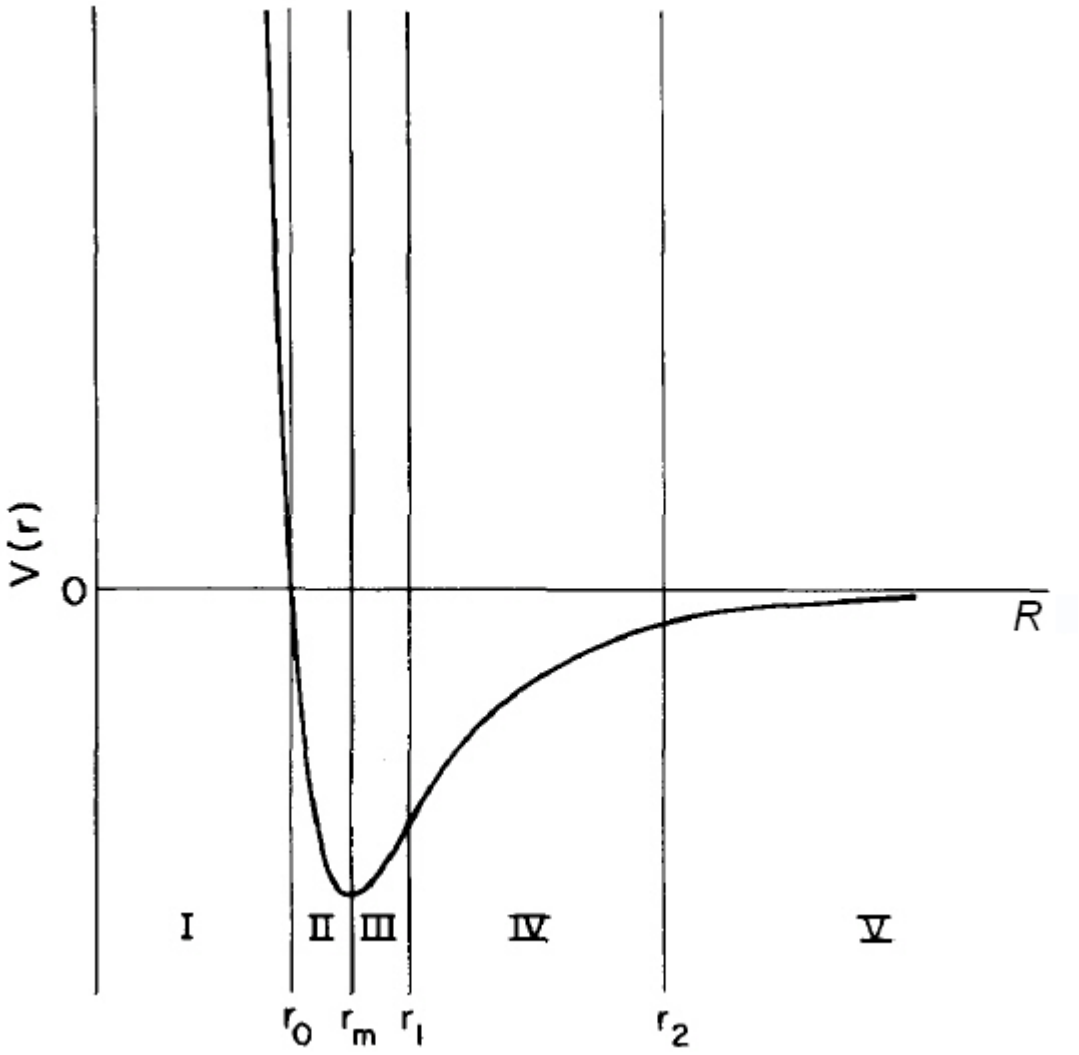

Figure 3.1: Typical M3SV potential with regions to scale. Regions I, II, and III are the Morse potential regions; IV is the spline region, and V is the long range van der Waals region (from Ref. [62]).

which turns out to be

$$r_{\mathrm{m,II}} = r_{\mathrm{m,III}} = r_{\mathrm{m}} \tag{3.6}$$

and the potentials at $\mathrm{r_m}$ satisfy the relation

$$V_{\mathrm{II}}(\mathrm{r_m}) = V_{\mathrm{III}}(\mathrm{r_m}) \tag{3.7}$$

Substituting Eq. 3.6 into Eq. 3.7, one has

$$\epsilon_{\mathrm{II}} = \epsilon_{\mathrm{III}} = \epsilon \tag{3.8}$$

Therefore, the only different parameters of V_{II} and V_{III} are α_{II} and α_{III}. Moreover, at $\mathrm{r_0}$, the requirements that

$$V_{\mathrm{I}}(\mathrm{r_0}) = V_{\mathrm{II}}(\mathrm{r_0}) = 0 \tag{3.9}$$

and

$$\left.\frac{\partial V_{\mathrm{I}}}{\partial R}\right|_{r_0} = \left.\frac{\partial V_{\mathrm{II}}}{\partial R}\right|_{r_0} \tag{3.10}$$

yield the relationship

$$\epsilon_1 = \frac{\alpha_{\mathrm{II}}}{\alpha_{\mathrm{I}}}\,\epsilon \tag{3.11}$$

$$\mathrm{r_0} = \mathrm{r_m} - \frac{\ln 2}{\alpha_{\mathrm{II}}} \tag{3.12}$$

and

$$\mathrm{r_{m\,I}} = \mathrm{r_0} + \frac{\ln 2}{\alpha_{\mathrm{I}}} \tag{3.13}$$

Thus α_{I} is the only independent parameter in $\mathrm{V_I}$.

The potential in region IV is represented by a single cubic spline function

$$V_{\mathrm{IV}}(x) = \beta_1 + (x - x_1)\{\beta_2 + (x - x_2)\,[\beta_3 + (x - x_3)\beta_4]\} \tag{3.14}$$

where $x = R/\mathrm{r_m}$ is a reduced distance.

In region V, the potential has the form of a Van der Waals expansion

$$V_{\mathrm{V}}(R) = -\frac{C_6}{R^6} - \frac{C_8}{R^8} - \frac{C_{10}}{R^{10}} \tag{3.15}$$

Given $V_{\rm III}$ and $V_{\rm V}$, $V_{\rm IV}$ is completely determined by the requirements of continuity of the potential and its slope via the relations

$$\begin{aligned}
\beta_1 &= V_{\rm IV}(x_1) \\
&= V_{\rm III}(\mathrm{r}_1) \qquad (3.16)\\
\beta_2 &= \frac{1}{x_2 - x_1}\left[V_{\rm IV}(x_2) - \beta_1\right] \\
&= \frac{1}{x_2 - x_1}\left[V_{\rm V}(\mathrm{r}_2) - \beta_1\right] \qquad (3.17)\\
\beta_3 &= -\frac{1}{x_2 - x_1}\left(\left.\frac{\partial V_{\rm IV}}{\partial x}\right|_{x_1} - \beta_2\right) \\
&= -\frac{1}{x_2 - x_1}\left(\left.\frac{\partial V_{\rm III}}{\partial R}\right|_{\mathrm{r}_1} \mathrm{r_m} - \beta_2\right) \qquad (3.18)\\
\beta_4 &= \frac{1}{x_2 - x_1}\left[\frac{1}{x_2 - x_1}\left(\left.\frac{\partial V_{\rm IV}}{\partial x}\right|_{x_2} - \beta_2\right) - \beta_3\right] \\
&= \frac{1}{x_2 - x_1}\left[\frac{1}{x_2 - x_1}\left(\left.\frac{\partial V_{\rm IV}}{\partial R}\right|_{\mathrm{r}_2} \mathrm{r_m} - \beta_2\right) - \beta_3\right] \qquad (3.19)
\end{aligned}$$

Thus, although this M3SV form appears to have 18 parameters, only ten (ϵ, $\mathrm{r_m}$, $\alpha_{\rm I}$, $\alpha_{\rm II}$, $\alpha_{\rm III}$, x_1, x_2, C_6, C_8 and C_{10}) are independent, the remaining parameters being determined by the continuity requirements. In practice the three C_n values are assumed known, and varied only if the data cannot be fit otherwise. Similarly, x_1 is usually taken as the inflection point of $V_{\rm III}$,

$$x_1 = \mathrm{r}_1/\mathrm{r_m} = [\mathrm{r_m} + {\alpha_{\rm III}}^{-1} \ln 2]/\mathrm{r_m} \qquad (3.20)$$

and x_2 is usually held fixed at some value (about 1.5) such that r_2 ($= \mathrm{r_m} x_2$) is large enough that the series in Eq. (3.15) is expected to be adequate, but small enough to prevent the spline in Eq. (3.14) from oscillating [62]. Furthermore, we use $\alpha = \alpha_{\rm I} = \alpha_{\rm II}$. Thus, there are really only *four* parameters (ϵ, $\mathrm{r_m}$, α and $\alpha_{\rm III}$) that are freely varied, with limited or no variation of the others.

Anisotropy is introduced by allowing ϵ, $\mathrm{r_m}$, and α_i to depend on the relative orientation of Ar and SF_6, and as illustrated in Fig. 3.2, the anisotropy of the potential depends upon the direction in which the argon atom approaches the SF_6. Following Ref. [45], we have

$$\epsilon = \bar{\epsilon}\left[1 + a_4 T_4 + a_6 T_6 + \cdots\right] \qquad (3.21)$$

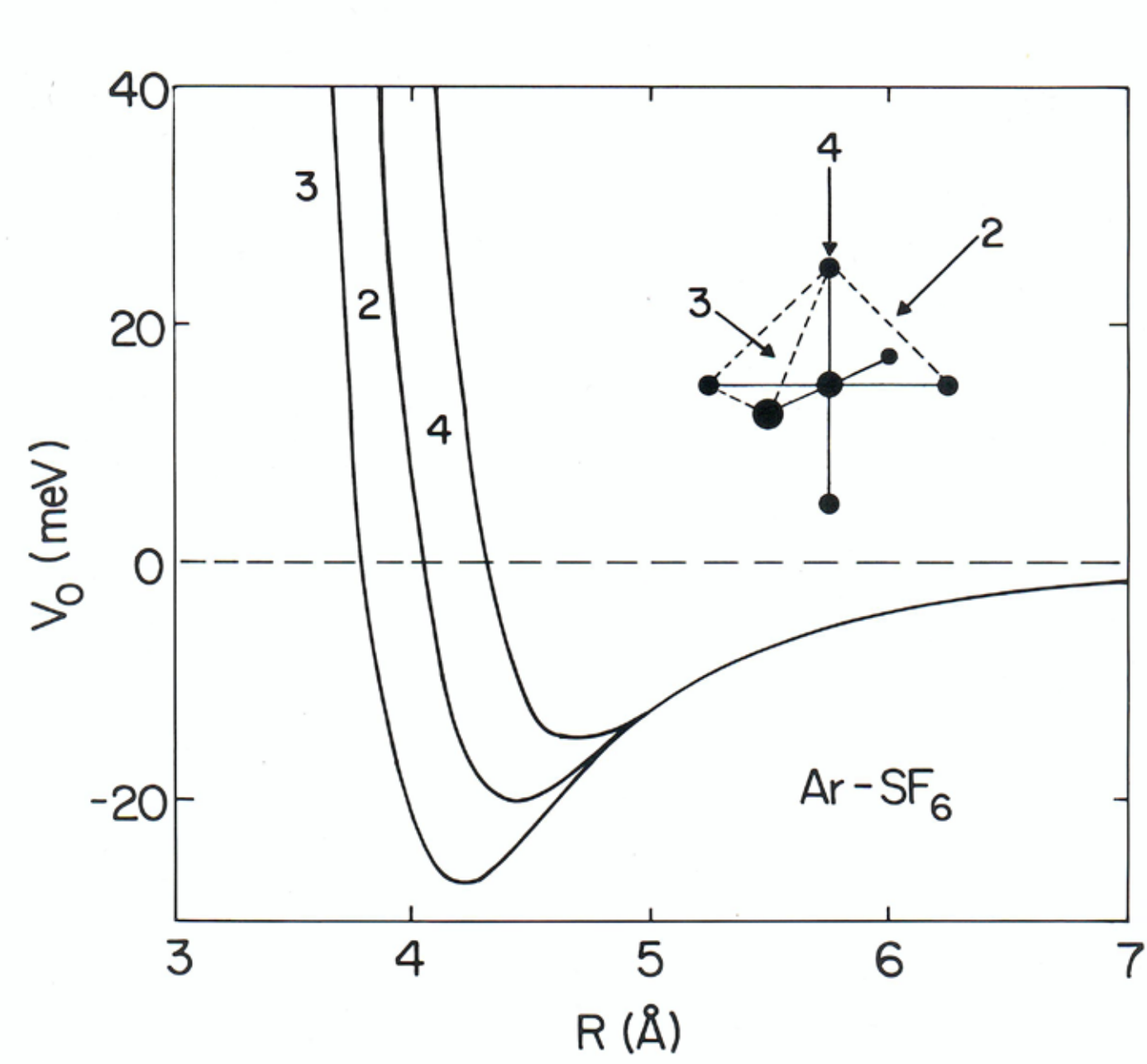

Figure 3.2: Radial behavior of the empirical Ar−SF_6 potential energy surface of Pack *et al.* [45, 62] along the two, three, and fourfold molecular symmetry axes of SF_6.

Table 3.1: Ar-SF_6 Potential parameters. The first seven are in atomic units, while the last six are dimensionless (From Ref. [45]).

Parameter	$\bar{\epsilon}$	$\bar{\mathrm{r}}_\mathrm{m}$	$\bar{\alpha}_\mathrm{I} = \bar{\alpha}_\mathrm{II}$	$\bar{\alpha}_\mathrm{III}$	C_6	C_8	C_{10}
	$(7.5 \pm 0.1) \times 10^{-4}$	8.39 ± 0.02	0.97 ± 0.03	0.88 ± 0.03	252 ± 10	6100	180 000
	a_4	a_6	b_4	b_6	x_1	x_2	$d_{4i/6i}$
	-0.5±0.1	+0.15±0.10	+0.10±0.03	-0.02±0.01	Infl. pt.	1.4	0

$$\mathrm{r_m} \;=\; \bar{\mathrm{r}}_\mathrm{m}\,[\,1 \,+\, b_4 T_4 \,+\, b_6 T_6 \,+\, \cdots\,] \tag{3.22}$$

$$\alpha_i \;=\; \bar{\alpha}_i\,[\,1 \,+\, d_{4i} T_4 \,+\, d_{6i} T_6 \,+\, \cdots\,] \tag{3.23}$$

in which the T_n are the spherical tensor elements

$$T_4 \,=\, \frac{1}{2}\left\{\sqrt{\frac{5}{6}}\,[\,Y_{4,\,4}(\theta,\phi) \,+\, Y_{4,\,-4}(\theta,\phi)\,] \,+\, \sqrt{\frac{7}{3}}\,Y_{4,\,0}(\theta,\phi)\right\} \tag{3.24}$$

$$T_6 \,=\, \sqrt{\frac{1}{8}}\left\{-\sqrt{\frac{7}{2}}\,[\,Y_{6,\,4}(\theta,\phi) \,+\, Y_{6,\,-4}(\theta,\phi)\,] \,+\, Y_{6,\,0}(\theta,\phi)\right\} \tag{3.25}$$

The parameters of the Pack *et al.* [45] potential for Ar-SF_6 are listed in Table 3.1.

3.3 The Ar−Ar interatomic potential

An accurate Ar−Ar pair potential reported by Aziz and Slaman [63] has the form

$$V(r) \,=\, \epsilon\left[A\cdot\exp\left(-\,\alpha\cdot(r/r_m) \,+\, \beta\cdot(r/r_m)^2\right) \,-\, \left(\frac{C_6}{(r/r_m)^6} \,+\, \frac{C_8}{(r/r_m)^8} \,+\, \frac{C_{10}}{(r/r_m)^{10}}\right)\cdot f(r)\right] \tag{3.26}$$

in which

$$f(r) \;=\; \exp\left(-\,(1-(D\cdot r_m)/r)^2\right) \quad \text{if } \frac{r}{r_m} \le D \tag{3.27}$$

$$\;=\; 1 \qquad\qquad\qquad\qquad\quad \text{otherwise} \tag{3.28}$$

The relevant parameters are: $r_m = 3.7565$ Å, $\alpha = 10.77874743$, $\beta = -1.812004$, $D = 1.36$, $C_6 = 1.10785136$, $C_8 = 0.56072459$, $C_{10} = 0.34602794$, $A = 2.26210716 \times 10^5$, $\epsilon = 99.5\,\mathrm{cm}^{-1}$ [63].

Monte Carlo simulations will require the calculation of many Ar−Ar pair interactions. For example, for a system containing an SF_6 molecule surrounded by 1000 Ar atoms, after each move of the SF_6 molecule, 1000 Ar−SF_6 potentials will need to be re-calculated; if an argon atom moved, one Ar−SF_6 potential and

Table 3.2: Parameters of the approximate potentials of Eq. 3.29

	A_6 (eV Å^6)	A_9 (eV Å^9)	A_{12} (eV Å^{12})
Ar−Ar	-59.7	-6.94×10^2	10.97×10^4

999 Ar−Ar potentials will need to be re-calculated. Moreover, the possibility of the latter case occurring is 1000 times larger than that of the former, and there may be about 10^6 trial moves per atom to occur in the whole simulation, resulting in about 6×10^8 calculation for Ar−Ar potentials if the acceptance ratio is 60 percent. Moreover, when the overall potential is calculated the first time, one needs to calculate 1000 Ar−SF_6 potentials and $(1000 \times 999/2 =)$ 499 500 Ar−Ar potentials. Therefore, use of the actual Aziz-Slaman Ar−Ar potential would be very time-consuming and a simple, yet good approximation would be reasonable. For the sake of computational efficiency, we therefore followed Eichenauer and Le Roy [27] and used this interaction energy by employing a simple form

$$V(r) = \frac{A_{12}}{r^{12}} + \frac{A_9}{r^9} + \frac{A_6}{r^6} \tag{3.29}$$

with parameters A_{12}, A_9 and A_6 determined from a least squares fit of Eq. 3.29 to the well region of the Ar−Ar potential recommended by Aziz and Slaman [63]. The resulting parameters are listed in Table 3.2. Figure 3.3 shows how this simple Ar−Ar potential model (dotted curve) agrees with the Aziz-Slaman model (solid curve).

Although this simplified potential is a rough approximation, its inadequacies were believed to be much smaller than the uncertainties in the Ar−SF_6 potential, especially at the energies associated with the low temperature matrices of interest [27]. Thus, the gain in computational speed is considered to be well worth the slight loss of accuracy.

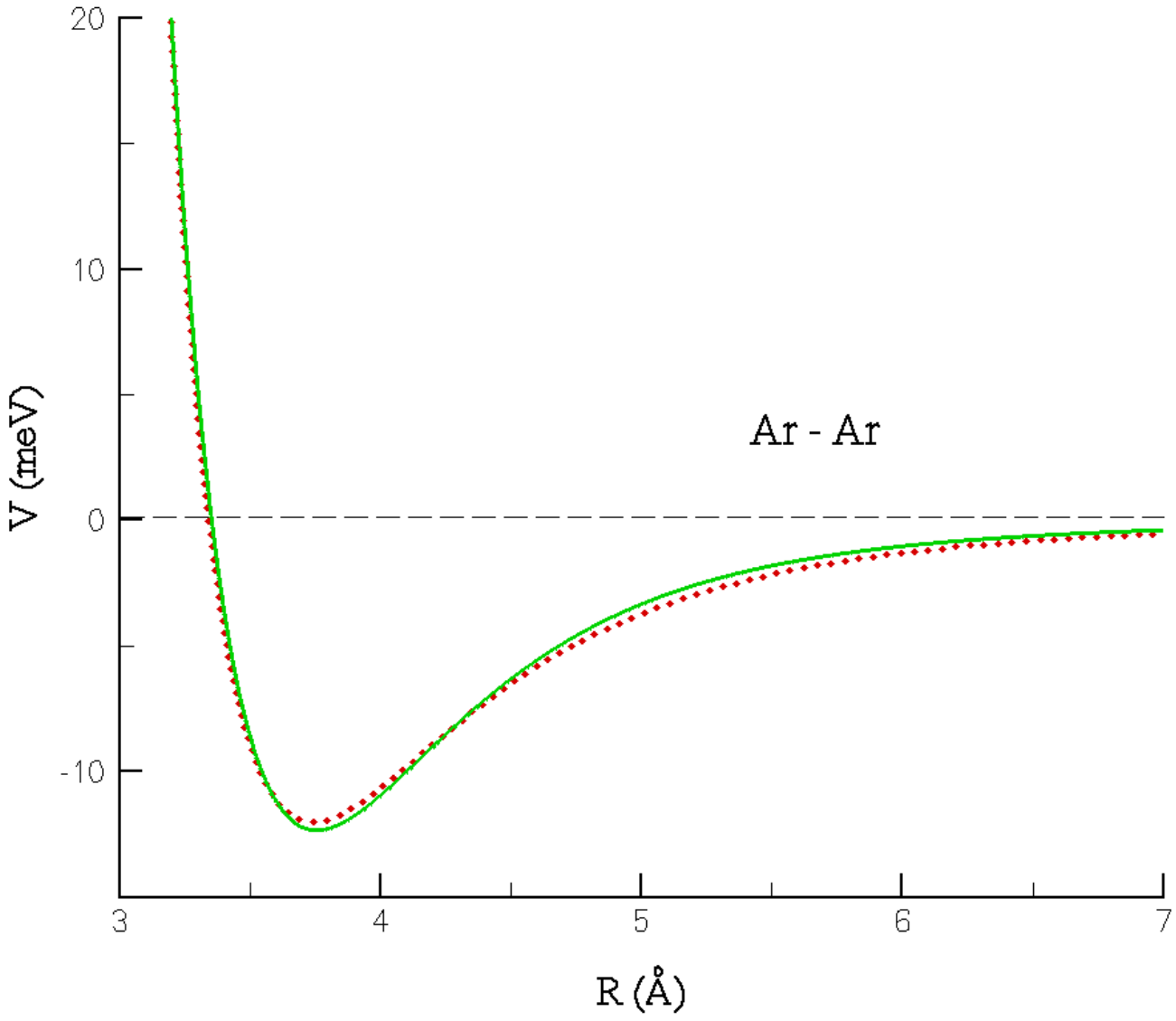

Figure 3.3: Ar−Ar interaction potential. Dotted curve: simple model with the form as Eq. 3.29. Solid curve: accurate model reported by Aziz and Slaman [63].

Chapter 4

Thermal averaging procedure

Using the perturbation theory model and potential functions described in the preceding chapters, one can readily calculate the frequency shifts of the components of the ν_3 band of SF_6 for any given SF_6 and lattice atom arrangement. However, the number of energetically accessible arrangements contributing to the thermal average is quite large at most temperatures. Monte Carlo (MC) and molecular dynamics (MD) simulations are two methods for obtaining the thermally averaged arrangement. In this project, the MC method was utilized to simulate the "relaxation" of an SF_6 molecule in an argon matrix, and to determine the thermal average of the frequency shifts of the three-component ν_3 mode. The reason that an MC calculation was employed is that simulations are easier to perform using MC than using MD, since no velocities, forces, or accelerations need to be calculated. The focus of this project is on the pattern of the ν_3 frequency shifts in a thermally equilibrated system, and on the assignment of the peaks in the experimental spectrum. While this type of information may in principle be obtained by both methods, MC is utilized here, as it is simpler to implement and less time consuming than analogous MD calculations. The following sections will first outline the standard Monte Carlo simulation procedures, and will then describe some details of our Monte Carlo simulation program.

4.1 Monte Carlo simulations

Monte Carlo methods for molecular simulation were first introduced in 1953 when Metropolis *et al.* reported a simulation of a system of 224 hard disks [44]. The name *Monte Carlo* was initially applied to a class of mathematical methods by scientists working on the development of nuclear weapons in Los Alamos in the 1940s, and today many types of calculations are referred to as Monte Carlo calculations. All Monte

Carlo methods are built around some sort of random sampling which involves the use of a random-number-generating algorithm. In the present context, a Monte Carlo simulation is one in which the locations and orientations of molecules are chosen according to a statistical distribution. In particular, many possible conformations of a molecule could be examined by choosing the conformation angles randomly. If enough iterations are done and the results are weighted by a Boltzmann distribution, the resulting average is the correct thermodynamic value of that property. The steps in a Metropolis Monte Carlo simulation for a molecular system are as follows.

1. Choose an initial set of particle positions. For a molecule, this would include a randomly selected orientation. In liquid simulations the molecules are often started with a lattice arrangement. For solvent-solute systems, the solute is often placed at the center of a collection of solvent molecules located in positions obtained from a simulation of the pure solvent [64]. For our matrix impurity problem, the Ar atoms will initially be arranged in a face-centered cubic (FCC) lattice with zero or one or more atoms removed to form a vacancy in which we shall place an SF_6 molecule.

2. Compute the potential energy of the system. In our case, this will be done by summing over all pairwise interactions.

3. Randomly choose a trial move for the system. This could involve moving all particles at once, but more often it involves moving one atom or molecule at a time, for reasons of computational efficiency. In the present work, this step will be broken into two parts: (i) randomly choose a particle to be moved, and then (ii) move that particle with the vector displacement $(\delta X,\ \delta Y,\ \delta Z)$, with increments $\delta X,\ \delta Y$ and δZ randomly chosen with uniform probability subject to the constraint that

$$-\Delta \leq |(\delta X, \delta Y, \delta Z)| \leq \Delta \tag{4.1}$$

   where Δ is a critical parameter governing the efficiency of the simulation (see below).

4. Compute the potential energy of the system in the new configuration.

5. Decide whether to accept the new configuration. The acceptance criterion in the Metropolis method is based on the old and new energies, and ensures that after a sufficiently large number of moves, the collection of all accepted and rejected moves represents a Boltzmann distribution. This criterion determines whether we keep the new configuration or restore the selected particle to its previous

position. When a move is performed, the new energy will usually differ from the old one. If the move is downhill in energy, that is, the change in potential energy $\Delta V(r)$ is negative, the move is always accepted. When the move is uphill in energy (i.e., $\Delta V(r)$ is positive), then the move is accepted with a probability determined according to the following procedure. First a random number is generated with a value $x \in [0, 1]$. If x is less than or equal to the probability factor P, with P given by

$$P = e^{-\Delta V(r)/kT} \tag{4.2}$$

then the move will be accepted. The probability factor is based on the Boltzmann distribution. This step may be summarized mathematically by noting that we accept any move (uphill or downhill in energy) with probability $min\{1, \exp(-\Delta V(r)/kT)\}$. If the increase in energy is large, then the probability factor is very small and the move is more likely to be rejected. On the other hand, if the rise in potential is small, the factor is relatively large and the move will more likely be accepted. Because this probability has to be greater than the random number x, only small positive changes in lattice energy have a significant probability of being accepted. Accepting moves that are energetically unfavorable allows the simulation to sample a larger configuration space. The sampling procedure allows the system to migrate from a given configuration through slightly more repulsive configurations, to arrive at a more stable structure.

6. Iterate Steps 3 through 5 until the system is thermally equilibrated.

7. Continue iterating and collecting data to compute the desired property. The expectation value of any property is simply its average value, defined by the sum of its calculated values divided by the total number of trial moves considered. This should yield a valid Boltzmann average as long as the acceptance criterion mentioned in Step 5 ensures that the probability of a configuration being accepted is equal to the probability of it being included in a Boltzmann distribution.

The size of the move in Step 3 of the above procedure will affect the computational efficiency of the simulation. An inefficient simulation is one that requires an excessively large number of iterations, i.e., more potential energy calculations to obtain results of a given accuracy. For example, if the step size is too small it will take many iterations for the atom arrangements to change significantly. On the other hand, if the move size is too large few moves will be accepted, and there is little movement through configuration space. In practice, the step size Δ is often adjusted during the simulation so that about half the trial

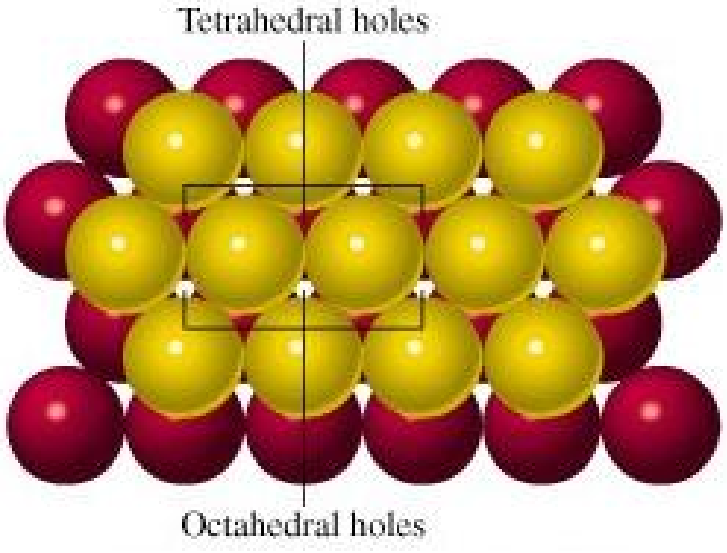

Figure 4.1: Top view of FCC lattice. (From Ref. [68])

moves are accepted, i.e., the acceptance ratio is about 0.5. This ratio is defined as the number of times a move was accepted (Step 5 above) divided by the total number of attempted moves. Efficient calculations are generally associated with an acceptance ratio between 0.5 and 0.7 [64, 65].

4.2 Details of the simulation program

4.2.1 Initial configuration and types of vacancy

As described in Sec. 4.1, the first step of a Monte Carlo simulation is to specify an initial configuration for the whole system. Argon is chemically inert and optically transparent, and its intermolecular forces are relatively weak. The properties of rare gases have been well studied and reviewed [66, 67]. X-ray diffraction studies have shown that the rare gases normally crystallize in a cubic close-packed (CCP) structure with a face-centered cubic (FCC) unit cell [43]. In this geometry, the lattice may be viewed as closed-packed layers of atoms stacked one on the other. Each atom in the lattice has six nearest neighbours in each layer. In CCP structures, the interstitial volume is minimized and each atom is in contact with three other atoms in the plane below and three other atoms in the plane above (see Figs. 4.1 and 4.2). Therefore, each atom has twelve nearest neighbours. Figure 4.3 illustrates the unit cell of a face-centered cube formed by argon atoms. Grey circles denote argon atoms "hidden" behind the visible face of the cube; lines shown there are not meant to represent bonds, but merely to illustrate the framework of the FCC unit cell. The labels

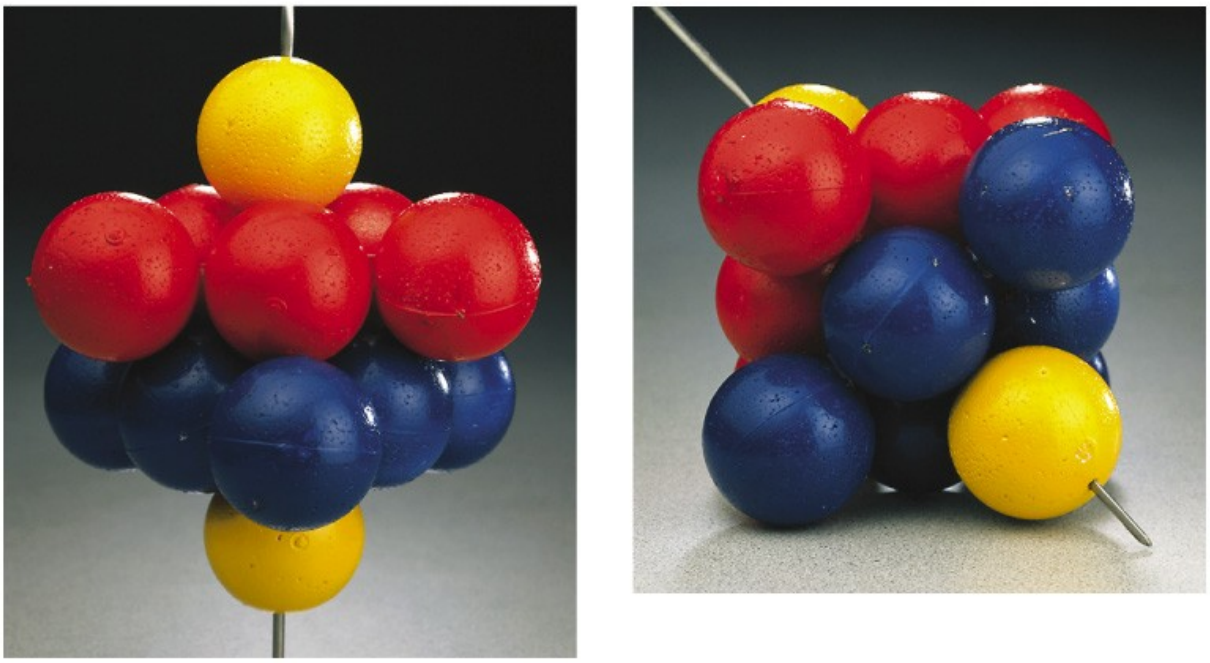

Figure 4.2: The unit cell of the face-centered cube formed by argon atoms. (From Ref. [68])

adjacent to some of the black points of the unit cell illustrate four types of position in the FCC unit cell: one located at the corner with the coordinate (0, 0, 0), one located at the center of the face ($l/2,\ 0,\ l/2$), one located at the center of the bottom ($l/2,\ l/2,\ 0$), and the fourth one located at the center of the side ($0,\ l/2,\ l/2$), where l is the edge length of the unit cell. All the other positions of this unit cell, and then all the other positions of the entire matrix, may be reproduced by moving these four initial points along x, y, or z directions by $n\,l$ (n is an integer) distances. The starting configuration for our simulation is generated by assuming we have a large number of argon atoms in a perfect FCC arrangement.

The model which we use to represent the matrix is an approximately spherical sample of up to 1505 argon atoms with the SF_6 located at the center of that sphere. Since the perturbation of the argon atoms located farther from the SF_6 molecule will decrease drastically, as described in Sec. 2.4, 1505 or so argon atoms is believed to be sufficient to simulate a good matrix environment (See Ref. [69]). After the argon matrix was set up, it is necessary to label the argon atoms in some appropriate manner so that they can be identified and moved during the MC procedure. In our simulation, all the argon atoms were labelled with respect to their distances from the center of the matrix; in other word, the farther away the atom is, the larger its numerical label is. For our 1505-atom spherical lattice, the distance from the center of the matrix to the farthest shell of argon atoms is about 24 Å.

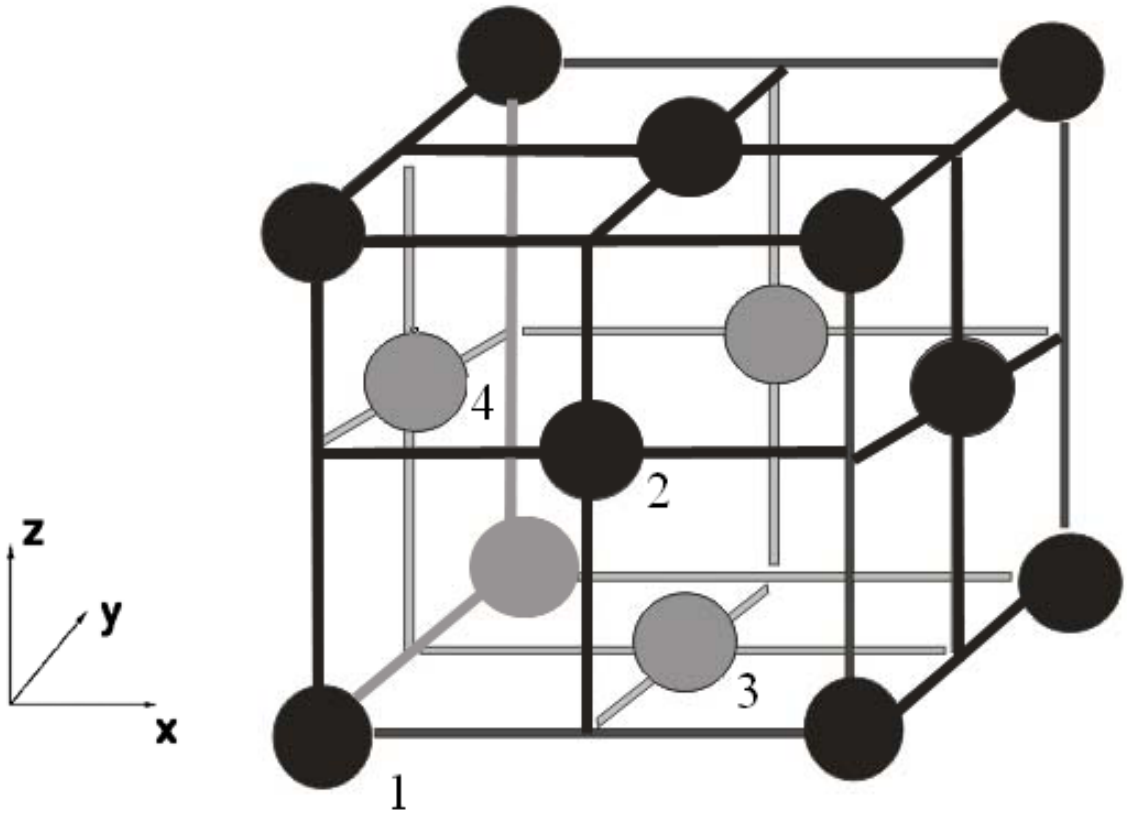

Figure 4.3: The unit cell of the face-centered cube formed by argon atoms. Labels illustrate four types of positions in the unit cell.

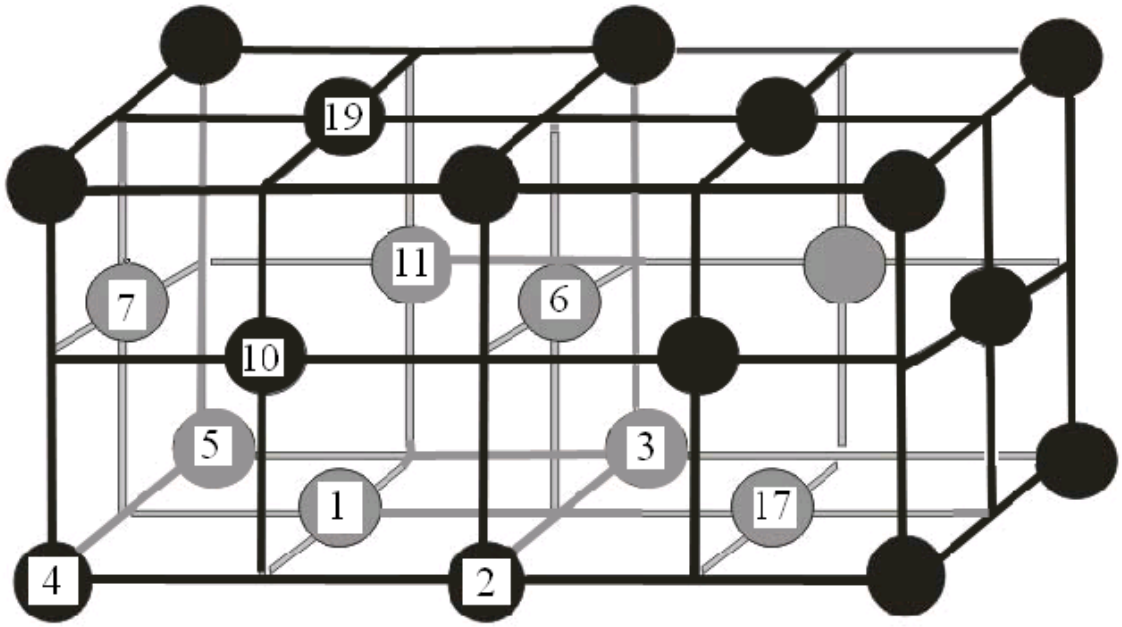

Figure 4.4: Different vacancy sites may be formed by removing different combination of labelled atoms.

Although there are about 1500 argon atoms in the matrix model used in our simulation, not all of the atoms need to move during the simulation. This is also because the perturbing atoms most distant from the SF_6 molecule will make much smaller contributions to the frequency shifts than the inner surrounding atoms will. Moving only the inner atoms can save computer time, and still provides a good approximation to the system. In our project, the number of movable argon atoms varied from about 50 to about 600, and the radius of this sphere of movable atoms was varied from 8 Å to 18 Å.

There are two ways to introduce an SF_6 molecule into the matrix, interstitially, or by removing one or more argon atoms. The edge length of the FCC unit cell for a pure Ar lattice is 5.313 Å at 10 K and 5.328 Å at 30 K [43], while the distance from one fluorine atom to the other along the F−S−F bond is about 6.2 Å [8]. The potential curves for SF_6-Ar and Ar-Ar discussed in Chap. 3 also show that SF_6 is larger than an argon atom (See Fig. 3.2 and 3.3). Thus, it would seem to be energetically very unfavorable to introduce an SF_6 into the matrix interstitially. Thus, it would seem more likely that the chromophore is admitted to be introduced into the matrix and approximately maintain the FCC packing of the lattice through the removal of lattice atoms. Different numbers of argon atoms may be removed, and for a given number of removed argon atoms the geometry of the vacancy site could vary; thus there are several types of vacancy sites that could contain an SF_6 molecule.

Figure 4.4 represents two FCC unit cells of the argon matrix in which a number of atoms are labelled

numerically. These atoms are labelled using the techniques described above, where we assume that argon atom No. 1 defines the center of the system.

Site **0** is the interstitial site formed by placing the SF_6 at the center of a unit cell, without removing any argon atoms from the lattice. One would expect this configuration to be very unstable. Site **1** is formed through the removal of the No. 1 atom from the system. It has the highest symmetry, with twelve nearest neighbors adjacent to the vacancy. The splitting of the ν_3 frequency for an SF_6 molecule in Site **1** is expected to be minimal. Moreover, because this site is heavily crowded, one may expect it to relax to a more stable configuration during the simulation. In Site **2**, formed by removing argon atoms No. 1 and 2, one would expect there to be a distinction between an internal SF_6 vibration parallel to the site axis and one perpendicular to it.

Two possible ways to remove three argon atoms from a lattice were examined: Site **3a** which has a compact triangular form arising from the removal of argon atoms No. 1, 2 and 6, which are all nearest neighbours, and Site **3b** which has a linear form arising from the removal of argon atoms No. 1, 2 and 5, which comprise two nearest-neighbour pairs. In Site **3b** SF_6 vibrational motion perpendicular to the symmetry axis of the vacancy is expected to be the most restricted, while in Site **3a** its vibrations perpendicular to the plane defined by the three removed atoms is restricted. In each case, however, the motion perpendicular to the symmetry axis is expected to be at least approximately doubly degenerate, and the motion along that axis is singly degenerate.

Site **4a** is formed through the removal of argon atoms No. 1, 2, 6 and 10, which are all nearest neighbours; it has tetrahedral symmetry, so the resulting spectrum is not expected to show a large splitting of the degenerate vibration, due to the high symmetry of this type of vacancy. Three more sites with four atoms removed were also examined: Site **4b** formed by removing atoms No. 1, 2, 6 and 5; it may be regarded as a combination of Sites **3a** and **3b**, Site **4c** is formed by removing atoms No. 1, 2, 6 and 17, and Site **4d** is formed by removing atoms No. 1, 2, 3 and 10. These four vacancy sites may all be looked on as Site **3a** plus one other atom. Although the last three sites are not symmetric, in a simulation they could relax to a tetrahedral shape or some other relatively compact site.

Site **5a**, with atoms No. 1, 2, 6, 10, and 3 atoms removed, is similar to Site **4a**, but with an additional atom removed from one of the sides of the tetrahedron. Site **5b**, with atoms No. 1, 2, 6, 10 and 17 removed, is similar to Site **5a**, so these two may be expected to have similar ν_3 frequency shifts. One loose site with five atoms removed is Site **5c** which has atoms No. 1, 2, 3, 4 and 5 removed. Site **5d** is formed through the removal of atoms No. 1, 6, 7, 10, and 11, which is also loose.

Four possible vacancy sites with six atoms removed were considered: Site **6a** has atoms No. 1, 2, 6, 10, 3 and 11 removed, and may be viewed being Site **4a** with two close atoms removed. Site **6b** has atoms No. 1, 2, 3, 4, 5 and 6 removed, and Site **6c** has atoms No. 1, 2, 6, 10, 5 and 11 removed; it may be viewed as being Site **4a** with one close atom and one relatively distant atom removed. Site **6d** has an octahedral configuration, with atoms No. 1, 6, 7, 10, 11, and 19 removed. One might expect Site **6d** would be relatively stable and have little contribution to the frequency splitting of ν_3 band of the SF_6 molecule. The low symmetry of the first three six-atom-vacancy sites makes it difficult to make predictions regarding their vibrational splitting patterns.

The simulations may show, however, that the memory of the initial geometry of the vacancy sites may be at least partly lost when one allows for annealing and thermal averaging. Since the most stable configuration for a pure argon lattice at low temperature is an FCC matrix [43], as the number of removed argon atoms increase, the stability of the system decreases. Therefore, there should be no need to examine too large vacancies. In our simulation, we found that those sites with more than five argon atoms removed have made relatively little contribution to the frequency shifts (see following chapters).

In summary, placing an SF_6 in an interstitial site or a vacancy created by the removal of a single Ar atom is very restrictive, due to the size difference between the chromophore and an Ar atom; the lattice would not be able to remain in a pure FCC configuration. On the other hand, removing too many atoms would create a vacancy that is energetically unfavorable, since it becomes more likely for the vacancy to collapse when the matrix is annealed. However, we expect to find that several types of vacancies will be energetically and thermally accessible, and our modelling of various vacancy types should determine the most likely such sites. In the simulations described herein, SF_6 was initially placed in the center of the chosen vacancy.

4.2.2 Performing a move

The main part of an MC simulation is the movement of particles. This procedure contains three major steps: choosing a particle, moving the particle, and deciding whether the move is to be accepted.

Random number generator

One might expect that computer programs would be able to generate “absolutely random” numbers. If that were the case, by generating random numbers, computer programs would be capable of using the random movements of particles to sample an ensemble perfectly. However, it is impossible for a computer program

to generate absolutely random numbers, since any program can only produce output that is entirely predictable, and hence it cannot be absolutely random. The word "random" in real life and in computer simulations describe concepts at different levels. In real life, to be random means to be unpredictable, and to be uncontrollable. In computer simulations, it is conceptually and physically impossible to reach complete randomness, although one may expect to attain the same statistical result from a sufficiently long simulation.

An imprecise, but working, definition of randomness in the context of computer-generated sequences, is to say that the deterministic program that produces a random sequence should be different from, and, in all measurable respects, statistically uncorrelated with, the computer program that uses its output [70]. In other words, any two different random number generators should be able to produce statistically the same results when coupled to a particular applications program. Otherwise, at least one of them is not a good generator, at least with regard to that particular application.

The above definition is circular, comparing one generator to another. However, there exist several generators which do satisfy this condition over a very broad class of applications programs. It is also found empirically that statistically identical results are obtained from random numbers produced by physical processes [70].

The most common random number generator, usually supplied by the computer system, is a *linear congruential generator*, which generates a sequence of integers $I_1,\ I_2,\ I_3,\ \cdots$, each between 0 and $m-1$ (a large number) by the recurrence relation

$$I_{j+1} = a\,I_j + c \pmod{m} \tag{4.3}$$

where m is the *modulus*, and a and c are positive integers called the *multiplier* and the *increment*, respectively [70]. One always needs to specify a *seed* for a random number generator to begin generating numbers. Each initializing value will typically return a different subsequent random sequence, or at least a different subsequence of some one enormously long sequence. However, the same seed will always return the same random sequence for this linear congruential generator. Eq. 4.3 will eventually repeat itself, with a period that is clearly no greater than m. Moreover, the length of the period depends on how m, a, and c are chosen. This system-supplied random number generator usually runs very rapidly, requiring only a few arithmetic operations per call, and it is almost universally applicable. On the other hand, the disadvantage of this generator is also obvious: it is not free of sequential correlation on successive calls. For example,

one cannot use this random number generator to generate k-random points to "fill up" a k dimensional space, but rather will lie on $(k-1)$-dimensional "planes". There will be at most about $m^{1/k}$ such planes. Another flaw is that with this generator the low-order (least significant) bits are often much less random than their high-order bits [70]. Because of these shortcomings, one might need to be cautious regarding a system-supplied random number generator.

Reference [70] introduced several substitutional random number generators. The generator ran1 passes most statistical tests and is fairly fast. The only disadvantage of ran1 is that its period, which is approximately 1×10^8, is somewhat short. However, ran1 is still a good random number generator for general use. The generator ran2 is about 50 percent slower than ran1. However, ran2 is believed to be able to provide perfect random numbers, within the limits of its floating-point precision. Thanks to its much longer period, ran2 is particularly useful when one needs to generate more than 1×10^8 random numbers in a single calculation. An even better generator is ran4, but it consumes twice the computing time of ran2.

The average number of trial moves per particle during one of our simulations may be as many as 1×10^6 and there are about 1 500 argon atoms in the matrix, so there would be about 1.5×10^9 trial moves in the entire procedure. During a trial move, one needs one random number to choose a particle, three random numbers to translate a particle in the three-dimensional space, three more random numbers to rotate the SF_6 molecule if it is the chosen particle, and one random number to decide whether this trial move is to be accepted. Therefore, more than 7.5×10^9 random numbers need to be generated during a typical simulation. Thus, considering the precision and speed of the simulation, the excellent yet still fast subroutine ran2 from Ref. [70] is utilized.

Choosing a random member

Assuming the number of movable argon atoms is *nmove*, a random variable i is defined by

$$i = \mathsf{INT}\left(\mathsf{ran2}\left(\text{seed}\right)\left(nmove + 3\right)\right) \tag{4.4}$$

where INT is a fortran function, which converts specified types to type integer by truncating toward 0 (the fraction is lost), and ran2 is the random number generator described above. The value of i is therefore within the range $[0,\ nmove + 2]$. Discarding too small i values, since several argon atoms are removed from the matrix to form vacancies, the choosing criteria are described as follows. If $i \leq nmove$, the i-th argon atom is chosen to translate. If $i = nmove + 1$, the SF_6 molecule is chosen to translate. If $i = nmove + 2$,

the SF_6 is chosen to rotate.

Moving a particle

To translate a particle (an argon atom or the SF_6 molecule) is quite straightforward. One can simply use the random number generator to obtain a random vector $(\delta X,\ \delta Y,\ \delta Z)$. The new position for the particle then will be $(X + \delta X,\ Y + \delta Y,\ Z + \delta Z)$.

Because Pack's model for SF_6-Ar interaction potential [45, 62] is anisotropic, the relative orientation of each argon atom with respect to the SF_6 bonds needs to be calculated. When the SF_6 molecule rotates, not only the angles of the F−S−F bonds with respect to the coordinate system but also the angles of every argon with respect to the SF_6 molecule vary, giving rise to complexity when calculating the SF_6-Ar interactions. It was found to be convenient to fix the SF_6 at the origin and to translate and rotate the argon atom lattice in the "opposite" direction. To perform such a rotation, one needs to first generate three random Euler angles, $\delta\phi,\ \delta\theta,$ and $\delta\psi$. Then the matrix of the first rotation by an angle $\delta\phi$ about the z axis is

$$\mathsf{D} = \begin{pmatrix} \cos\delta\phi & \sin\delta\phi & 0 \\ -\sin\delta\phi & \cos\delta\phi & 0 \\ 0 & 0 & 1 \end{pmatrix} \tag{4.5}$$

The matrix of the second rotation by an angle $\delta\theta \in [0, \pi]$ about the x axis is

$$\mathsf{C} = \begin{pmatrix} 1 & 0 & 0 \\ 0 & \cos\delta\theta & \sin\delta\theta \\ 0 & -\sin\delta\theta & \cos\delta\theta \end{pmatrix} \tag{4.6}$$

And the matrix of the third rotation by an angle ψ about the z axis (again) is

$$\mathsf{B} = \begin{pmatrix} \cos\delta\psi & \sin\delta\psi & 0 \\ -\sin\delta\psi & \cos\delta\psi & 0 \\ 0 & 0 & 1 \end{pmatrix} \tag{4.7}$$

Then the whole rotation matrix is

$$\mathsf{A} = \mathsf{BCD} \tag{4.8}$$

and the new coordinates of the argon atom is

$$\begin{pmatrix} X' \\ Y' \\ Z' \end{pmatrix} = \mathsf{A} \begin{pmatrix} X \\ Y \\ Z \end{pmatrix} \tag{4.9}$$

Since the SF_6 doesn't "computationally" rotate (but it is regarded as already "physically" rotated), it is easy to calculate the orientation of an argon atom with respect to the SF_6 molecule by simply using the (rotated) cartesian coordinates of the argon atom.

As Eq. 4.1 illustrated, the magnitude of the steps for the translation and the angles of the rotation must be limited by a carefully chosen step size Δ. The values of Δ were varied in several trial simulations to determine values for which about fifty to seventy percent of trial moves will be accepted. The value of the step size determined in this way are 0.06 Å for translation, and $0.1\,\pi$ for rotation. These values were used in the simulations reported herein.

4.2.3 Flowchart

Figure 4.5 presents a flow chart for our simulation. It shows that our simulation follows the standard Metropolis Monte Carlo procedure. First we set up an initial configuration in which SF_6 is positioned at the center of the particular type of vacancy in the FCC lattice of argon atom. After we calculate the potential energy of the system, we randomly choose a particle and perform a random move. Then we use the acceptance criterion based on the Boltzmann distribution to determine whether this trial move is to be accepted. If it is accepted, we will reset the configuration to the new one. Then the above sequence of steps is iterated until the number of moves reaches M_{EQ}, the assumed value for the number of moves required to equilibrate the system. In our simulation, the potential energy of the system does not change significantly after a relatively short run of about 1 000 moves per moving argon atom. Therefore, M_{EQ} need not be very large. In this equilibration phase, there is no need to perform the additional computational work of calculating the frequency shifts.

The simulation then continues, and in each step the ν_3 frequency shifts are calculated. After enough values (this is controlled by setting the value of M_{AV}) for the ν_3 shifts are collected, the simulation ends. The value of M_{AV} was tested by varying it between 3×10^4 and 1×10^6 moves per moving argon atom.

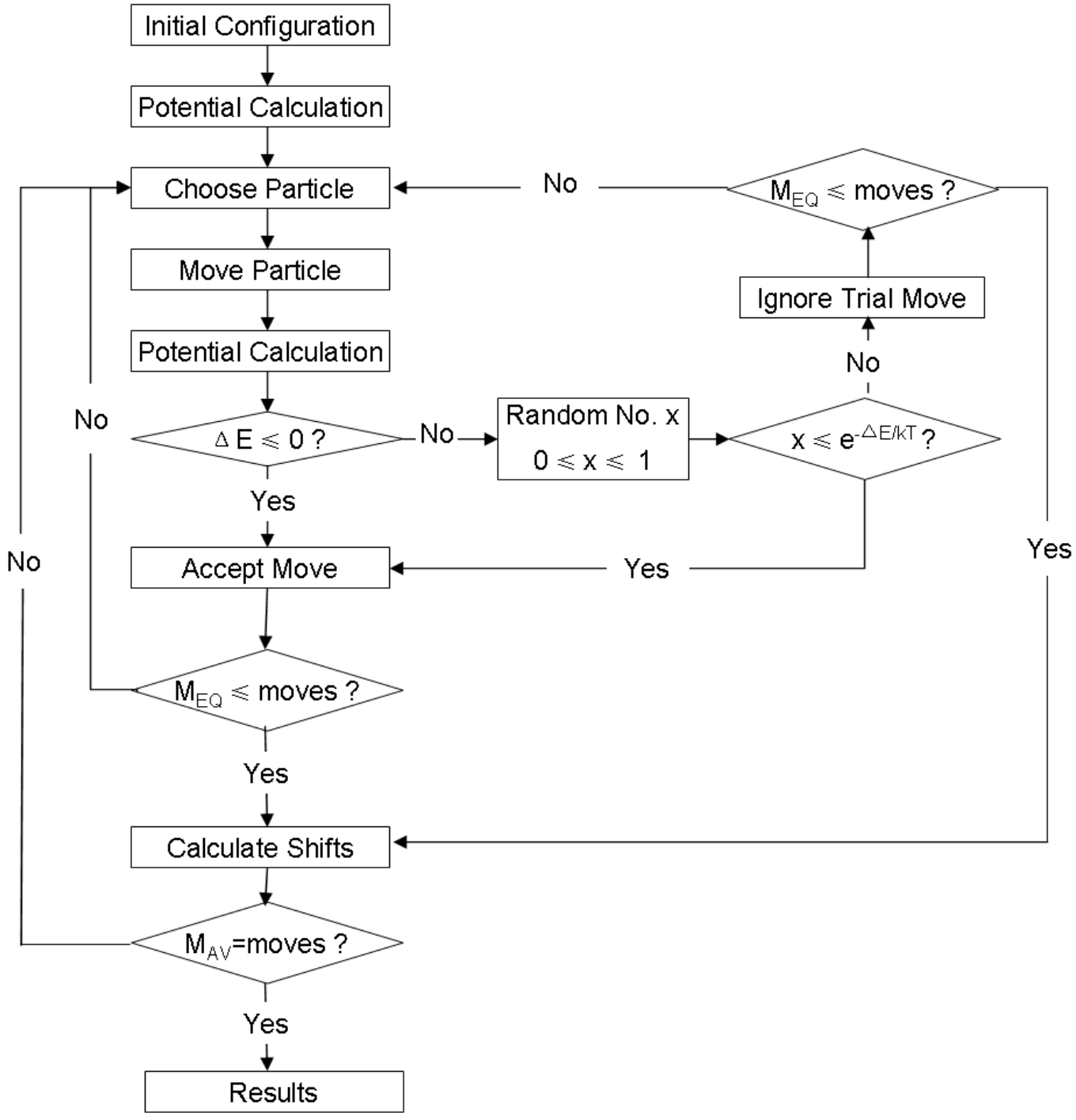

Figure 4.5: A flow chart of the standard Monte Carlo simulation

4.3 Convergence tests

Several parameters determine the computing time and affect the quality of the results. In order to obtain converged results as well as to save computing time, several convergence tests were performed to optimize these parameters.

Ref. [69] found 1 500 argon atoms can form a near perfect argon matrix with respect to the properties examined herein. The number of movable argon atoms was varied from about 50 to over 600, and 650 moving argon atoms was found to be adequate to simulate the behavior of the argon matrix. The system reached equilibrium after about 1 000 moves per moving argon atom. Initially, a total of 100 000 moves per moving argon atom was thought to be sufficient to obtain good simulated spectra for all the vacancy sites. However, the unexpected behavior of Site **2** indicated that about 1×10^6 moves per moving argon atom was necessary for its rational spectrum to be obtained (See Sec. 5.2.2 for more details).

Chapter 5

Frequency shift calculations

Using the IDID model developed by Eichenauer and Le Roy [27], the infrared spectrum of an SF_6 molecule in an argon matrix may be obtained by performing MC simulations. Sec. 5.1 will introduce line shape functions and least-squares fitting methods used herein. Sec. 5.2 will present the simulated spectra for each vacancy site and the results obtained from fits to the raw simulated spectra.

5.1 Fitting spectra to a sum of Gaussian functions

Figure 5.1 illustrates the spectrum for Site **3a** obtained from our simulation. This figure was obtained in the following way: the x-axis was divided into small bins of width 0.001 cm^{-1}. After each step in which frequency shifts were calculated, each of the three values obtained would be associated with one of the bins. After enough MC steps have been carried out for each bin to have a statistically significant number of values, a distribution curve of intensity vs. frequency shift is obtained. In other words, each MC move gives us three sticks on the frequency shift axis, as schematically illustrated in Fig. 5.1, and the distribution curve is obtained by counting the number of sticks within the same frequency-shift bin after M_{AV} MC moves. The curve in Fig. 5.1 has a Gaussian line shape and the peak area ratio appears to be approximately $1:2$. Since Site **3a** has a triangular configuration (see Sec. 4.2.1), one might expect to find that SF_6 vibration within the plane is doubly degenerate while the vibration perpendicular to the plane is singly degenerate. This would explain why the peak area ratio appears to be approximately $1:2$. To examine the area ratio more precisely, least-squares fit methods were utilized (see following discussion).

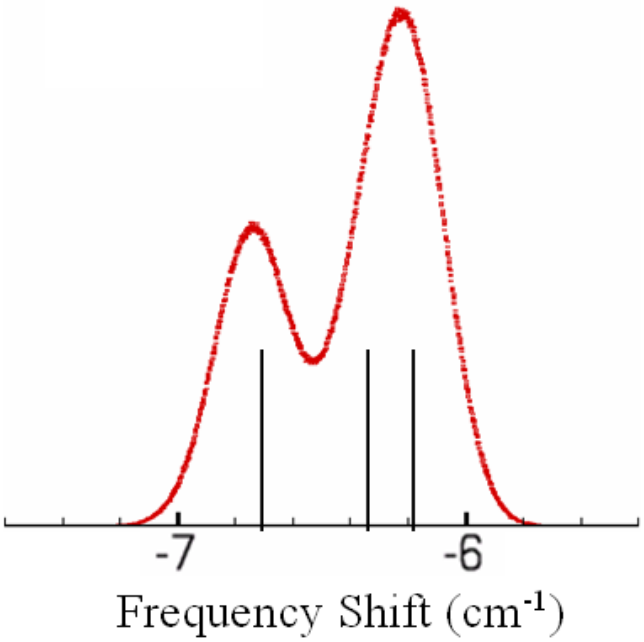

Figure 5.1: Simulated spectrum for Site **3a**. Black sticks represent three frequency shifts obtained from one MC move.

5.1.1 Gaussian and Lorentzian functions

The simulated spectrum may be expected to have a Gaussian line shape due to the stochastic averaging associated with the Metropolis Monte Carlo simulation which reproduces the Boltzmann distribution. In contrast, the experimental spectrum has peaks with Lorentzian line shapes, due to the homogeneous "pressure" broadening caused by the perturbing atoms (See Fig. 1.2) [9].

A Gaussian function has the form

$$G(\nu) = \frac{2}{\Delta\nu_{1/2}} \sqrt{\frac{\ln 2}{\pi}}\, e^{-4\,\ln 2\,\left[(\nu-\nu_0)\,/\,\Delta\nu_{1/2}\right]^2} \tag{5.1}$$

and a Lorentzian function has the form

$$L(\nu) = \frac{\Delta\nu_{1/2}/\,(2\pi)}{\left(\Delta\nu_{1/2}/2\right)^2 + \left(\nu - \nu_0\right)^2} \tag{5.2}$$

in which ν_0 is the peak position, and $\Delta\nu_{1/2}$ is the full width at half maximum (FWHM). The peak heights

for these functions are related to the linewidths $\Delta\nu_{1/2}$ by

$$G(\nu_0) = \frac{2}{\Delta\nu_{1/2}}\sqrt{\frac{\ln 2}{\pi}} \tag{5.3}$$

$$L(\nu_0) = \frac{2}{\pi\,\Delta\nu_{1/2}} \tag{5.4}$$

5.1.2 Least-squares fitting

In order to verify that the spectra obtained from the simulations have Gaussian line shapes, and to obtain the peak positions, peak height, FWHM, and peak area ratio of these spectra, one needs to fit each simulated spectrum to a sum of Gaussian functions. Non-linear least-squares fitting methods were employed to perform these fits. A brief description of the linear and non-linear least-squares fitting methods will be given here. For a thorough and detailed discussion of these techniques, see Chap. 15 of Ref. [70].

A least-squares fit seeks to find the values of a set of M parameters p_j ($j = 1,\ 2,\ \cdots,\ M$) which will optimize the agreement between a set of N experimental (or 'observed') data $y_o(i)$ ($i = 1,\ 2,\ \cdots,\ N$) and calculated values for these data $y_c\left(\{p_j\}; i\right)$ ($i = 1,\ 2,\ \cdots,\ N$) generated from a model defined by the M parameters. If all of the data are weighted equally, the least-squares fitting problem is concerned with determining the set of parameter values for which the weighted dimensionless sum of squares of derivations

$$\mathrm{DSSD} \equiv \mathrm{DSSD}(\{p_j\}) = \sum_{i=1}^{N}\left[\frac{y_o(i) - y_c\left(\{p_j\}\,; i\right)}{u(i)}\right]^2 \tag{5.5}$$

is a minimum [71]. Here $u(i)$ is the uncertainty of the observed datum $y_o(i)$. It is clear that DSSD will reach its minimum when

$$\frac{\partial\,\mathrm{DSSD}(\{p_j\})}{\partial\,p_k} = 0 \tag{5.6}$$

for all parameters p_k, simultaneously.

A least squares problem is called "linear" if the function defining the model may be written as

$$y_c(i) \equiv y_c\left(\{p_j\}; i\right) = \sum_{j=1}^{M} p_j\,\phi_j(i) \tag{5.7}$$

and the partial derivatives

$$\phi_j(i) \equiv \left[\frac{\partial y_c\left(\{p_j\}; i\right)}{\partial p_j}\right]_{\{p_k\},\,k\neq j} \tag{5.8}$$

have no dependence on the parameters p_j; if $\phi_j(i)$ is *not* independent of the p_j's, it is a "non-linear"

least-squares problem. A linear least squares fit has exactly one solution, consisting of a single unique set of p_j values. However, a non-linear problem may in general have a number of sets of p_j's for which the DSSD function has local minima, and there exists no *a priori* way of knowing how many such local minima exist or which one is the global minimum. In practice, however, converged fits may usually be obtained by performing an iterative series of linear fits until convergence is achieved.

Le Roy developed a subroutine NLLSSRR.F which can perform linear or non-linear least-squares fits and (if desired) automatically uses sequential rounding and refitting to minimize the numbers of parameter digits that must be quoted. To employ this subroutine, the following procedure may be followed. When a linear least-squares fit is performed, the only input information required are the experimental data $y_o(i)$'s, their estimated uncertainties $u(i)$'s, and a knowledge of the partial derivatives of each calculated data point $y_c(\{p_j\}; i)$ with respect to each parameter of the model, p_k. When a non-linear least-squares fit is performed, the overall procedure will consist the following steps:

1. Read in the experimental data $y_o(i)$ and generate some initial set of trial values for the parameters defining the model, $\{p_j(trial)\}$.

2. Prepare the arrays $\mathrm{YO}(i) = [y_o(i) - y_c(\{p_j(trial)\}, i)]$ and $\mathrm{DYDP}(i, j)$, the partial derivatives of i-th datum with respect to each of the free parameters p_j ($j = 1, 2, \cdots, M$) varied in the fit.

3. Call the linear least-squares routine and update the parameter values: $p_j(new) = p_j(trial) + \Delta p_j$.

4. Iterate these steps until convergence is reached.

The quality of fit to an experimental data set, and the ability of a given set of parameters to accurately reproduce those data are represented by the *dimensionless standard error* (DSE) of the fit

$$\bar{\sigma}_f = \left\{ \frac{1}{N - M} \sum_{i=1}^{N} \left[\frac{y_c(i) - y_o(i)}{u(i)} \right]^2 \right\}^{1/2} \tag{5.9}$$

where $u(i)$ is the uncertainty of the experimental datum $y_o(i)$ [72]. If the experimental uncertainties used are correct, a $\bar{\sigma}_f$ value of less than 1.0 means that on average, the calculated values generated from the model differ from the experimental data by less than the associated experimental uncertainties, while a value of (say) 4.5 would mean that on average the predictions of the model differ from the experiment by 4.5 times the experimental uncertainties.

It is clear that fitting our simulated spectra to a sum of Gaussian functions is a non-linear least-squares

fit problem. The program PEAKFIT.F developed by Le Roy calls the subroutine NLLSSRR.F and performs such fits. Utilizing PEAKFIT.F, all the simulated spectra were fit to a sum of Gaussians, and the fitting results will be discussed in the next section.

5.2 Frequency shifts for different sites

5.2.1 Frequency shifts for the vacancy sites

Utilizing the non-linear least-squares fit methods described above, the simulated spectrum for each type of vacancy site was fitted to a sum of Gaussian functions. The simulated spectrum for Site **3a** shown in Fig. 5.2 was first normalized by fixing the total peak area to be 3, to reflect presence of the three components in the ν_3 vibrational band. The uncertainties, $u(i)$, of the experimental data were set to be 1.0. The spectrum was then fitted to Gaussians, first with no constraints, and then with the peak area ratio fixed at 1 : 2, yielding the results presented in Table 5.1. Comparing the two sets of results, we see that the peak positions, heights, and FWHM from the two fits are very similar. Although the DSE associated with the area-fixed fit ($\bar{\sigma}_f = 0.1500$) is somewhat larger than that associated with the no-constraints fit ($\bar{\sigma}_f = 0.1322$), there are no obvious differences between the simulated spectrum and the curve generated using the data from the lower part of Table 5.1, as illustrated in Fig. 5.2. One may conclude that the peak area ratio for Site **3a** should be fixed at 1 : 2, as expected from its geometric structure.

The same fit methods and uncertainty settings were employed for the other sites. Their spectra and fitting results are presented in Figs. 5.3 - 5.14 and Tables 5.2 - 5.13. Site **0** is an interstitial site, and is expected to be highly symmetric, but also quite crowded. The single peak of its simulated spectrum represents its high symmetry. Site **1** is formed by removing one argon atom, and the perturbation by the argon atoms again might be expected to be symmetric. However, as illustrated in Fig. 5.4, a "shoulder" is observed, showing that the relaxed configuration of Site **1** is not symmetric. Moreover, the average magnitude of the frequency shift for Site **1** is larger than that for Site **0**. This might to be due to the fact that the number of nearest neighbours for Site **1**, which is 12, is larger than that for Site **0**, which is 6, resulting in a stronger perturbation occurring in the former case even though these neighbours might, on average, be farther away. The simulated spectrum for Site **2** shows unexpected features: three peaks are observed, but the peak area ratio is not the expected 1 : 1 : 1. Instead, the peak area ratio is roughly 3 : 2 : 1, as shown in Table 5.4. Fig. 5.7 shows that the simulated spectra for Sites **4a**, **4b** and **4d** are the same, with one single peak observed. This implies that both Sites **4b** and **4d** collapsed to Site **4a** during

the MC simulation, and the tetrahedral symmetry of Site **4a** gives rise to a single peak in the corresponding simulated spectrum. Several other sites also collapsed during the MC simulation: in particular, Sites **5a** and **5b** have the same simulated spectrum; Sites **6a** and **6b** have the same simulated spectrum. Site **6d** is an octahedral site, and its simulated spectrum shows single peak as might be expected. Site **5d** has a similar geometry to that of Site **6d**, and it also has a single peak in its simulated spectrum.

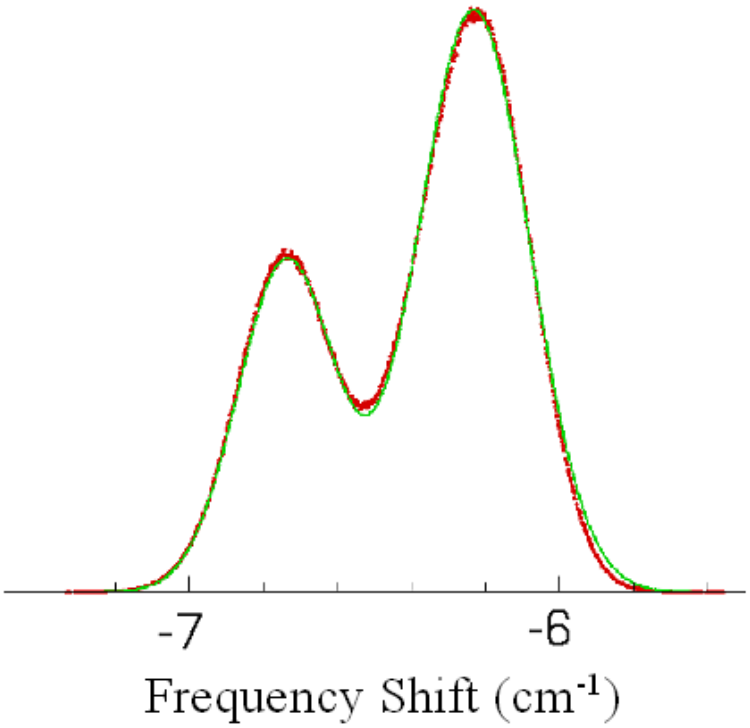

Figure 5.2: Dotted curve: simulated spectrum for Site **3a**. Line curve: the Gaussians generated using the data from the lower part of Table 5.1.

Table 5.1: Non-linear least-squares fitting results for Site **3a**. The upper part is the results for fitting with no constraints, while the lower one is that for fitting with peak area ratio fixed to be 1 : 2

No constraints				DSE = 0.1322
Peak	Type	Parameter	Value	Uncertainty
1	Gaussian	position	-6.7357	0.0003
		width	0.3205	0.0008
		height	12.21	0.02
2	Gaussian	position	-6.2308	0.0002
		width	0.3478	0.0005
		height	21.35	0.02
Area ratio 1:2				DSE = 0.1500
Peak	Type	Parameter	Value	Uncertainty
1	Gaussian	position	-6.7379	0.0003
		width	0.3100	0.0006
		height	12.16	0.02
2	Gaussian	position	-6.2323	0.0002
		width	0.3536	0.0002
		height	21.32	

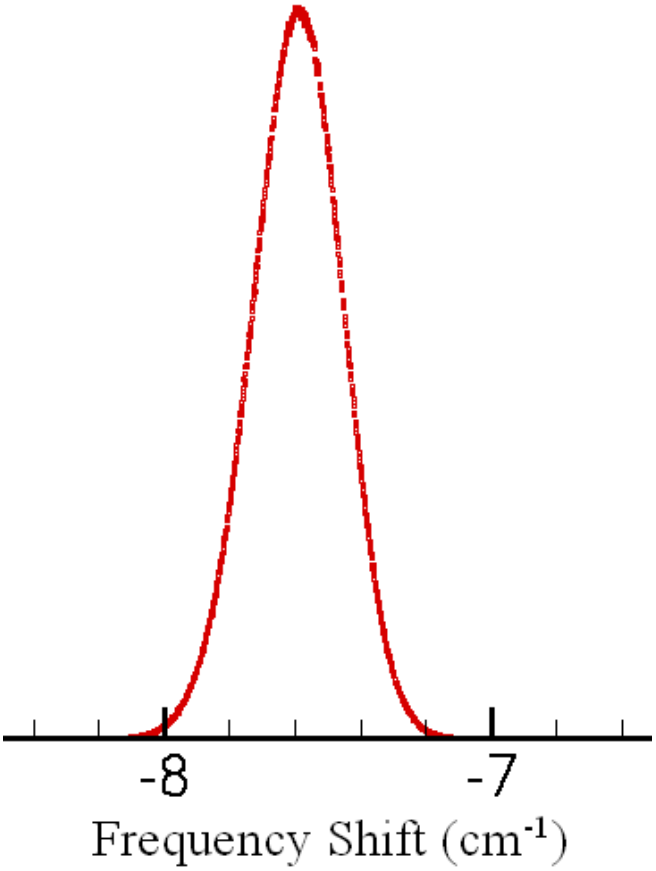

Figure 5.3: Simulated spectrum for Site **0**.

Table 5.2: Non-linear least-squares fitting results for Site **0**.

				DSE = 0.1452
Peak	Type	Parameter	Value	Uncertainty
1	Gaussian	position	-7.5917	0.0001
		width	0.3231	0.0002
		height	34.86	0.02

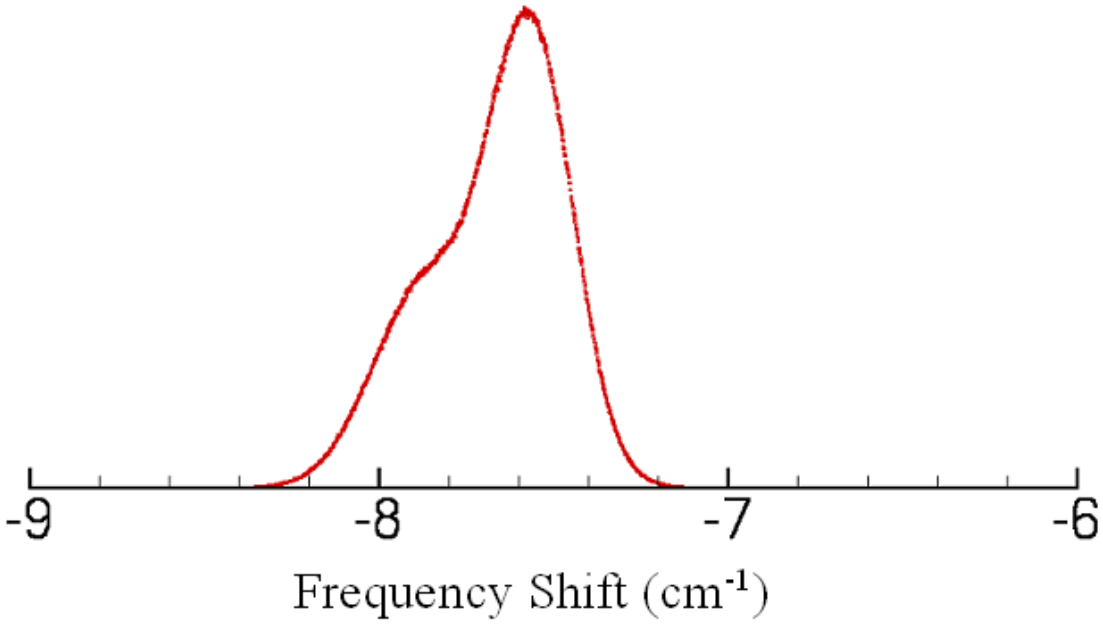

Figure 5.4: Simulated spectrum for Site **1**.

Table 5.3: Non-linear least-squares fitting results for Site **1**. The upper part is the results for fitting with no constraints, while the lower one is that for fitting with peak area ratio fixed to be 1 : 2

No constraints				DSE = 0.0530
Peak	Type	Parameter	Value	Uncertainty
1	Gaussian	position	-7.8683	0.0005
		width	0.3523	0.0008
		height	11.36	0.01
2	Gaussian	position	-7.5633	0.0002
		width	0.2840	0.0002
		height	25.65	0.02
Area ratio 1:2				DSE = 0.0608
Peak	Type	Parameter	Value	Uncertainty
1	Gaussian	position	-7.8778	0.0002
		width	0.3376	0.0003
		height	11.14	0.01
2	Gaussian	position	-7.5666	0.0001
		width	0.2885	0.0001
		height	26.06	

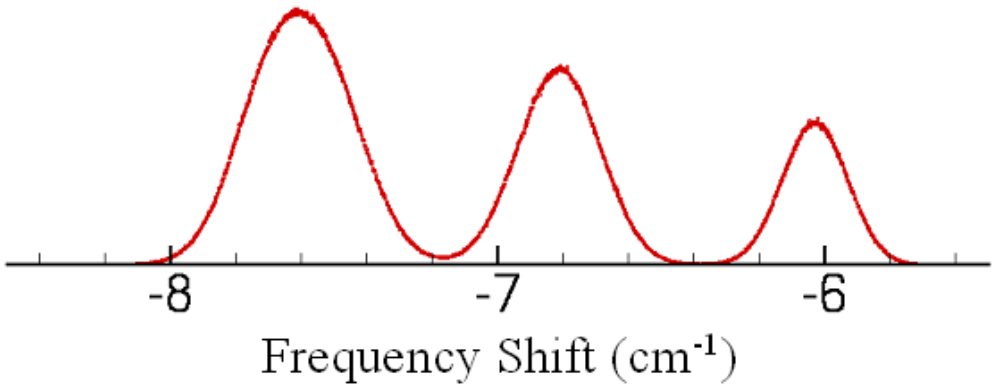

Figure 5.5: Simulated spectrum for Site **2**.

Table 5.4: Non-linear least-squares fitting results for Site **2**. The upper part is the results for fitting with no constraints, while the lower one is that for fitting with peak area ratio fixed to be $3:2:1$

No constraints				DSE = 0.0783
Peak	Type	Parameter	Value	Uncertainty
1	Gaussian	position	-7.612	0.0002
		width	0.3650	0.0004
		height	12.59	0.01
2	Gaussian	position	-6.813	0.0002
		width	0.2876	0.0005
		height	9.10	0.01
3	Gaussian	position	-6.0300	0.0002
		width	0.2301	0.0005
		height	7.04	0.01
Area ratio 3:2:1				DSE = 0.2452
Peak	Type	Parameter	Value	Uncertainty
1	Gaussian	position	-7.613	0.0005
		width	0.3560	0.0001
		height	12.42	0.04
2	Gaussian	position	-6.813	0.0006
		width	0.3120	0.0001
		height	9.45	
3	Gaussian	position	-6.0300	0.0007
		width	0.2160	0.0001
		height	6.82	

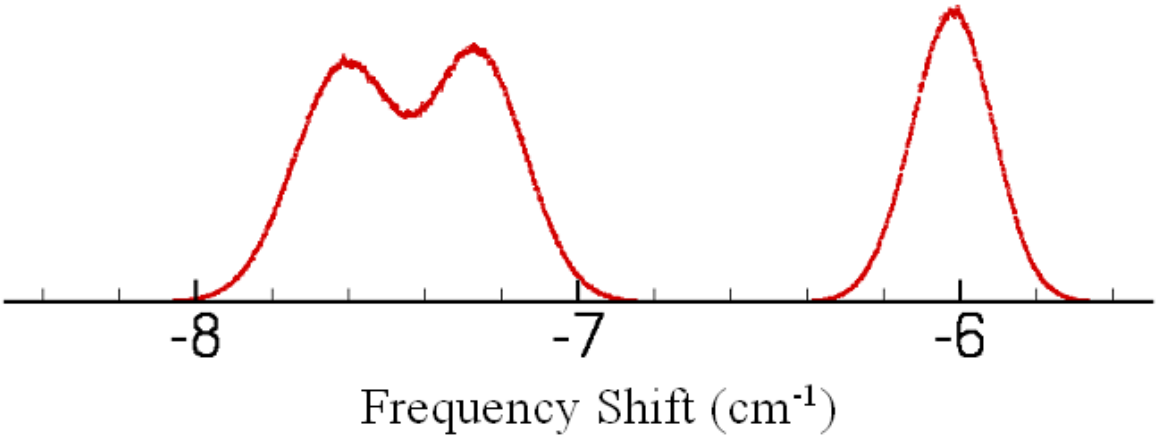

Figure 5.6: Simulated spectrum for Site **3b**.

Table 5.5: Non-linear least-squares fitting results for Site **3b**. The upper part is the results for fitting with no constraints, while the lower one is that for fitting with peak area ratio fixed to be 1 : 1 : 1

No constraints				DSE = 0.0530
Peak	Type	Parameter	Value	Uncertainty
1	Gaussian	position	-7.6120	0.0002
		width	0.3109	0.0005
		height	12.23	0.01
2	Gaussian	position	-7.2618	0.0002
		width	0.2906	0.0004
		height	12.77	0.01
3	Gaussian	position	-6.0201	0.0001
		width	0.2493	0.0002
		height	15.08	0.01
Area ratio 1:1:1				DSE = 0.0543
Peak	Type	Parameter	Value	Uncertainty
1	Gaussian	position	-7.6135	0.0001
		width	0.3078	0.0002
		height	12.21	0.01
2	Gaussian	position	-7.263	0.0001
		width	0.2935	0.0002
		height	12.80	
3	Gaussian	position	-6.0201	0.0001
		width	0.2493	0.0002
		height	15.07	

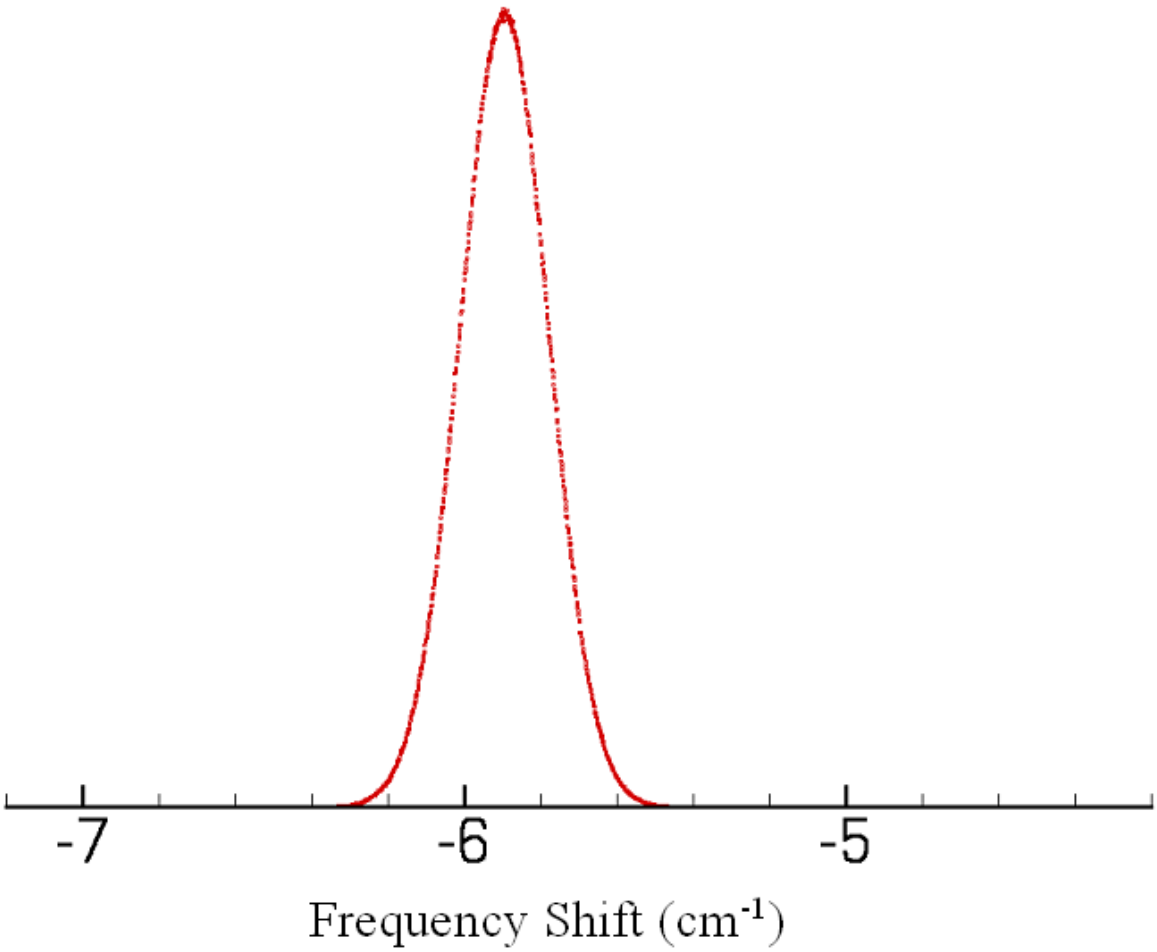

Figure 5.7: Simulated spectrum for Site **4a/4b/4d**.

Table 5.6: Non-linear least-squares fitting results for Site **4a/4b/4d**.

				DSE = 0.0464
Peak	Type	Parameter	Value	Uncertainty
1	Gaussian	position	-5.8950	0.0002
		width	0.2728	0.0006
		height	41.30	0.01

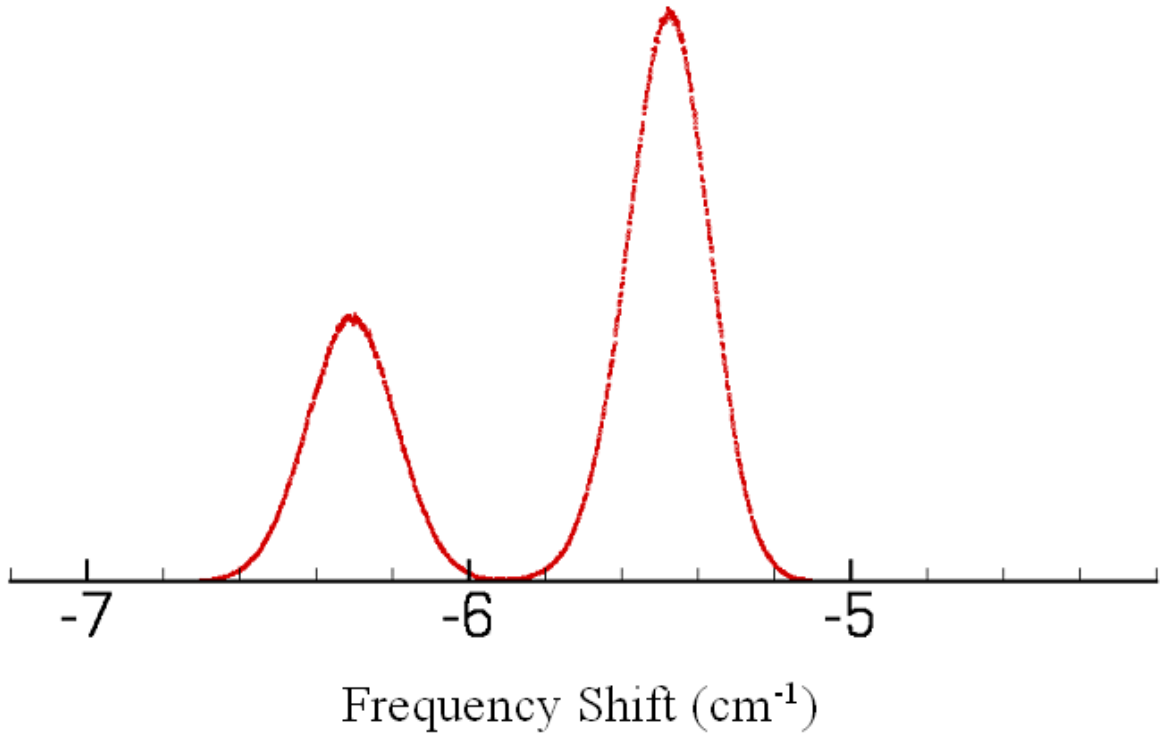

Figure 5.8: Simulated spectrum for Site **4c**.

Table 5.7: Non-linear least-squares fitting results for Site **4c**. The upper part is the results for fitting with no constraints, while the lower one is that for fitting with peak area ratio fixed to be 1 : 2

No constraints				DSE = 0.1230
Peak	Type	Parameter	Value	Uncertainty
1	Gaussian	position	-6.3060	0.0002
		width	0.2742	0.0005
		height	13.71	0.02
2	Gaussian	position	-5.4768	0.0001
		width	0.2540	0.0002
		height	29.47	0.02
Area ratio 1:2				DSE = 0.1233
Peak	Type	Parameter	Value	Uncertainty
1	Gaussian	position	-6.3060	0.0002
		width	0.2735	0.0004
		height	13.69	0.02
2	Gaussian	position	-5.4768	0.0001
		width	0.2541	0.0002
		height	29.48	

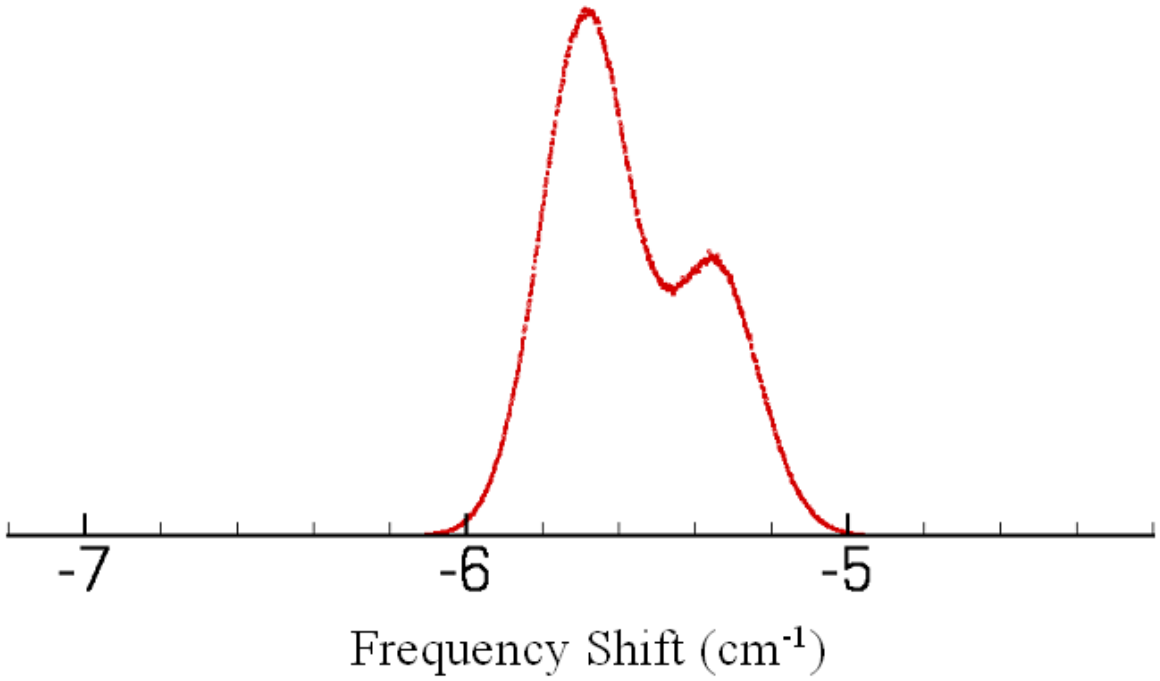

Figure 5.9: Simulated spectrum for Site **5a/5b**.

Table 5.8: Non-linear least-squares fitting results for Site **5a/5b**. The upper part is the results for fitting with no constraints, while the lower one is that for fitting with peak area ratio fixed to be 2 : 1

No constraints				DSE = 0.0491
Peak	Type	Parameter	Value	Uncertainty
1	Gaussian	position	-5.6858	0.0001
		width	0.2770	0.0002
		height	27.12	0.01
2	Gaussian	position	-5.3466	0.0001
		width	0.2697	0.0003
		height	13.92	0.01
Area ratio 2:1				DSE = 0.0491
Peak	Type	Parameter	Value	Uncertainty
1	Gaussian	position	-5.6858	0.0004
		width	0.2770	0.0001
		height	27.12	0.01
2	Gaussian	position	-5.3467	0.0001
		width	0.2698	0.0002
		height	13.92	

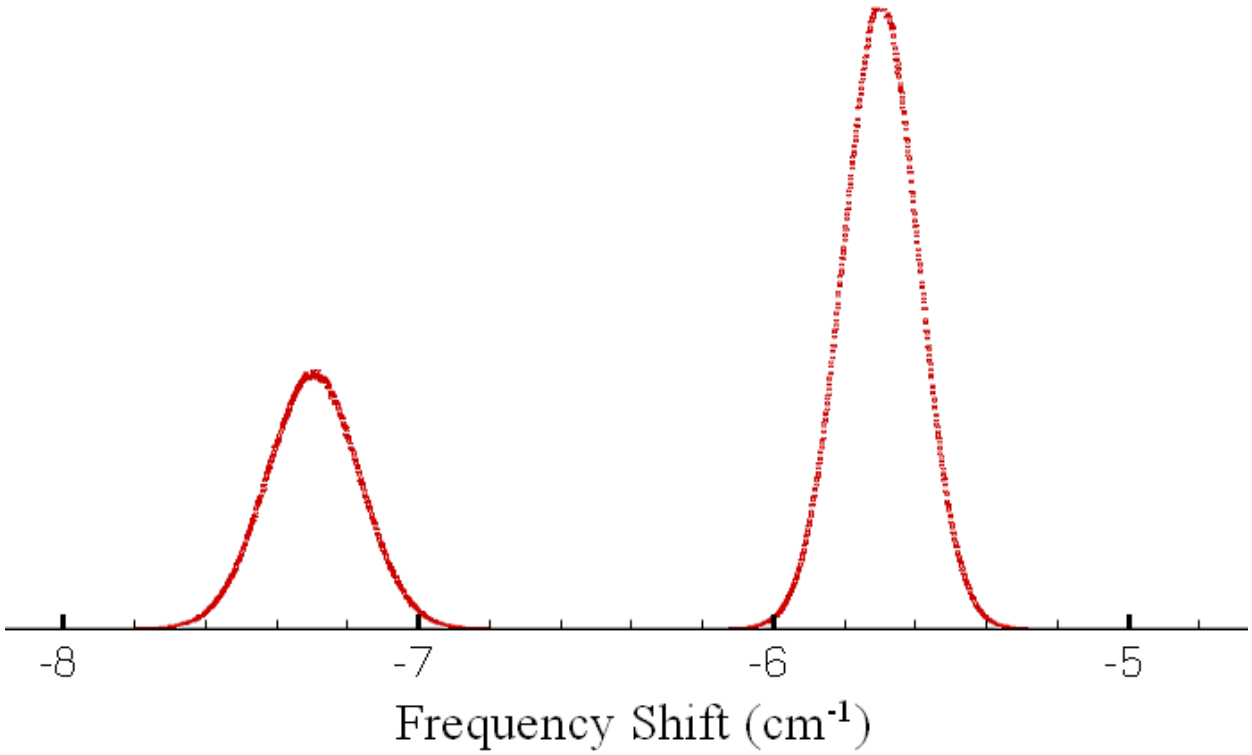

Figure 5.10: Simulated spectrum for Site **5c**.

Table 5.9: Non-linear least-squares fitting results for Site **5c**. The upper part is the results for fitting with no constraints, while the lower one is that for fitting with peak area ratio fixed to be $1:2$

No constraints				DSE = 0.0598
Peak	Type	Parameter	Value	Uncertainty
1	Gaussian	position	-7.296	0.0001
		width	0.3057	0.0003
		height	12.30	0.01
2	Gaussian	position	-5.698	0.0001
		width	0.2495	0.0001
		height	30.11	0.01
Area ratio 1:2				DSE = 0.0598
Peak	Type	Parameter	Value	Uncertainty
1	Gaussian	position	-7.2964	0.0001
		width	0.3055	0.0002
		height	12.29	0.01
2	Gaussian	position	-5.6978	0.0001
		width	0.2495	0.0001
		height	30.11	

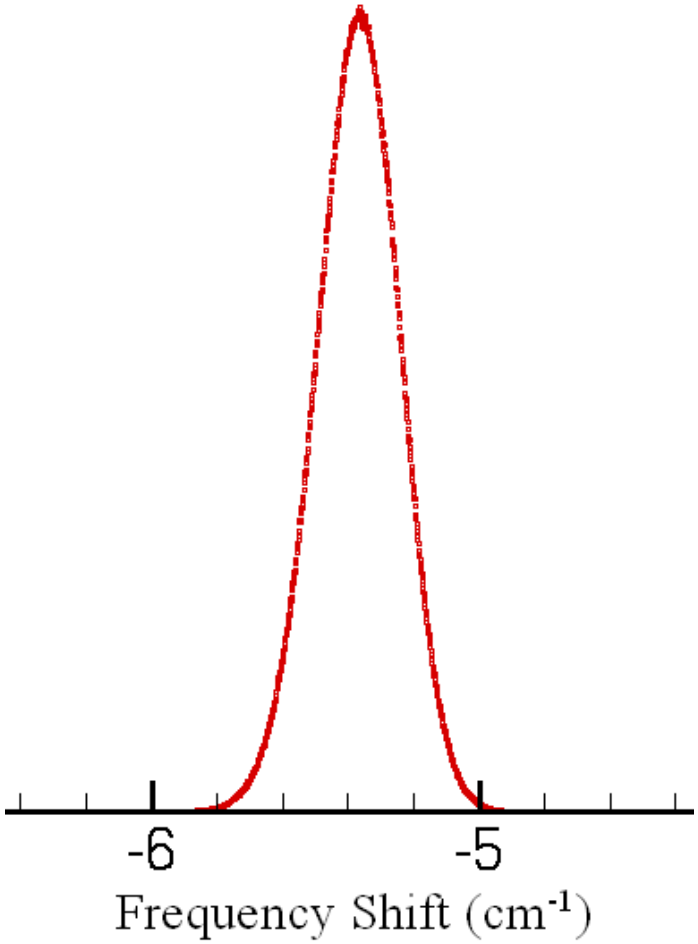

Figure 5.11: Simulated spectrum for Site **5d**.

Table 5.10: Non-linear least-squares fitting results for Site **5d**.

				DSE = 0.1447
Peak	Type	Parameter	Value	Uncertainty
1	Gaussian	position	-5.3678	0.0001
		width	0.2956	0.0002
		height	38.04	0.02

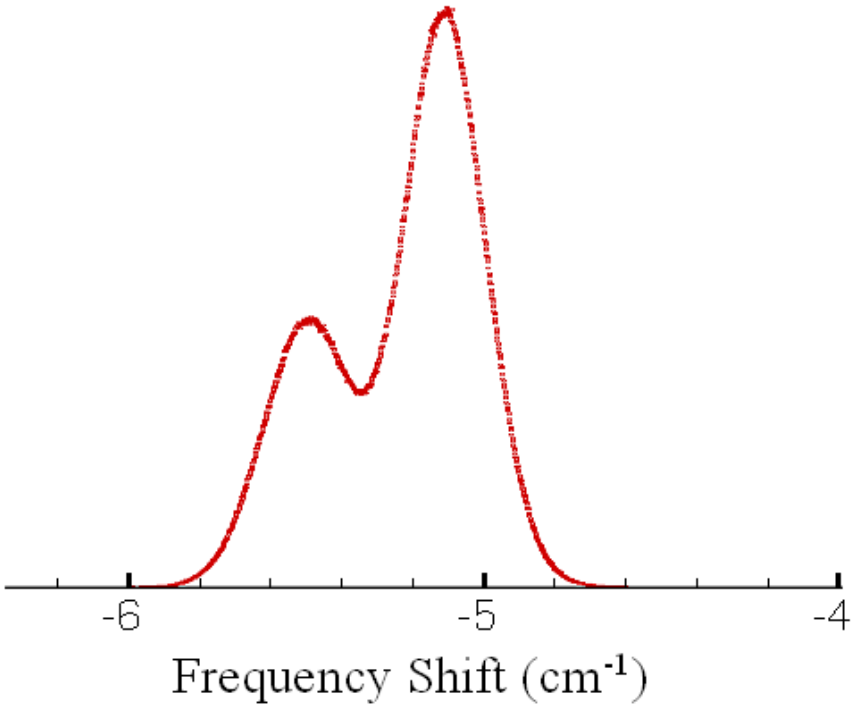

Figure 5.12: Simulated spectrum for Site **6a/6b**.

Table 5.11: Non-linear least-squares fitting results for Site **6a/6b**. The upper part is the results for fitting with no constraints, while the lower one is that for fitting with peak area ratio fixed to be 1 : 2

No constraints				DSE = 0.0650
Peak	Type	Parameter	Value	Uncertainty
1	Gaussian	position	-5.4977	0.0002
		width	0.2890	0.0004
		height	12.86	0.01
2	Gaussian	position	-5.1102	0.0001
		width	0.2729	0.0002
		height	27.59	0.01
Area ratio 1:2				DSE = 0.0667
Peak	Type	Parameter	Value	Uncertainty
1	Gaussian	position	-5.4970	0.0001
		width	0.2916	0.0002
		height	12.86	0.01
2	Gaussian	position	-5.1099	0.0001
		width	0.2719	0.0001
		height	27.59	

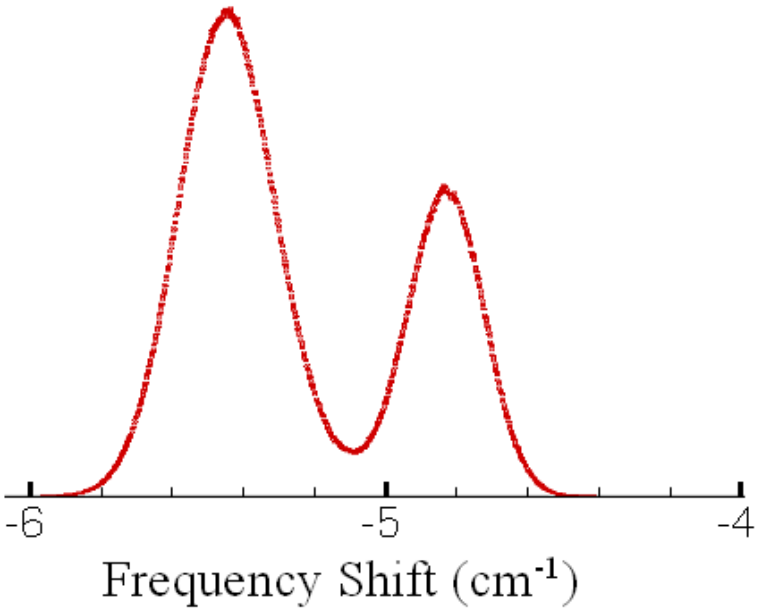

Figure 5.13: Simulated spectrum for Site **6c**.

Table 5.12: Non-linear least-squares fitting results for Site **6c**. The upper part is the results for fitting with no constraints, while the lower one is that for fitting with peak area ratio fixed to be 2 : 1

No constraints				DSE = 0.1258
Peak	Type	Parameter	Value	Uncertainty
1	Gaussian	position	-5.4458	0.0001
		width	0.3225	0.0003
		height	23.28	0.02
2	Gaussian	position	-4.8325	0.0002
		width	0.2559	0.0004
		height	14.74	0.02
Area ratio 2:1				DSE = 0.1261
Peak	Type	Parameter	Value	Uncertainty
1	Gaussian	position	-5.4458	0.0001
		width	0.3228	0.0003
		height	23.29	0.02
2	Gaussian	position	-4.8324	0.0002
		width	0.2552	0.0004
		height	14.73	

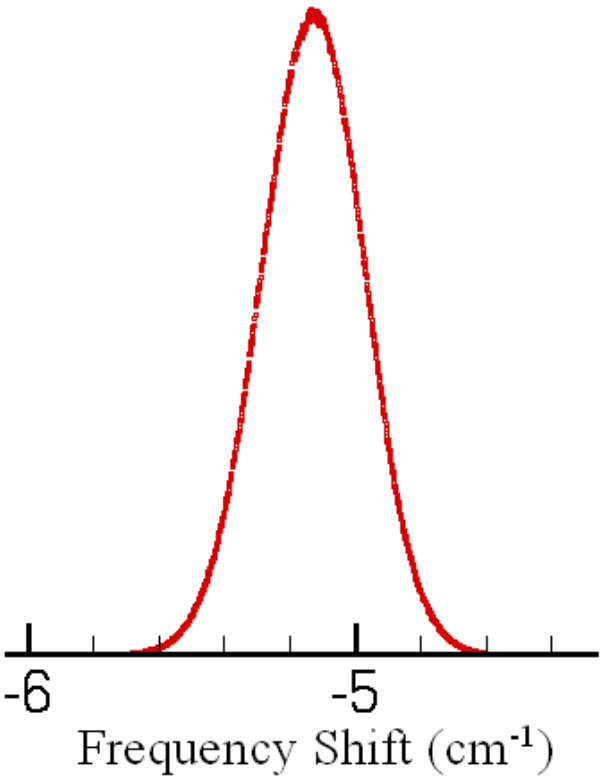

Figure 5.14: Simulated spectrum for Site **6d**.

Table 5.13: Non-linear least-squares fitting results for Site **6d**.

				DSE = 0.0900
Peak	Type	Parameter	Value	Uncertainty
1	Gaussian	position	-5.1293	0.0001
		width	0.3666	0.0002
		height	30.80	0.01

All the spectra presented above were obtained using the following simulation settings.

- The radius defining the size of the matrix sample is 24 Å, which means that up to 1 505 (the value for Site **0**) argon atoms surround the SF_6 molecule.
- The maximum distance from the center of the matrix to the farthest moveable argon atoms is 18 Å, which means that the number of moveable argon atoms is at most 627 (the value for Site **0**). The more distant argon atoms are frozen in perfect FCC positions during the simulation.
- The average number of MC move for one of the movable argon atoms during the simulation is 10^6.
- For the first 10^5 MC steps, the temperature of the system is set at 10 K. After that, the temperature increases to 30 K. After a total of *ca.* 3×10^8 more MC steps, the temperature drops back to 10 K. 10^5 more MC steps later, the frequency shifts begin to be collected.

The simulation for each spectrum requires about eighteen days to run on 1 CPU of a Silicon Graphics Origin 380, or five days on 1 CPU of an IBM 690HP.

For a particular site, one would expect that the ν_3 vibrational band of SF_6 might be split into two to three components. One may therefore expect that the area ratio for the two-components case is 1 : 2 or 2 : 1, and that for the three-components case is 1 : 1 : 1. As one can see from the fitting results, most of the simulated spectra for these vacancies accurately reproduce this behavior, with DSE for each no-constraints case being only slightly smaller than that for the corresponding area-fixed one. As is also expected, as the size of the vacancy increases, the peaks tend to have frequency shifts which are smaller in magnitude, because a larger vacancy leads to a weaker perturbation of the SF_6 molecule.

5.2.2 Site 2 is a special case

As discussed above, if the ν_3 band of SF_6 is split into three components, we would normally expect the peak area ratio to be 1 : 1 : 1. However, Site **2** appears to be an exception to this rule; its spectrum has three peaks, but the area ratio is approximately 3 : 2 : 1. Moreover, the DSE for the no-constraints fit is 0.0783 while that for the area-fixed case is 0.2452, 210 % larger.

At first, it was thought that this result reflected the fact that the simulation had not reached convergence, so the number of MC moves per argon atom was increased from 3×10^4 to 1×10^6; however, the same results were obtained. The number of moveable atoms was then increased from about 55 to about

627, and the number of moves during the annealing procedure was also increased, but the simulation still generated the same spectrum.

The unexpected peak area ratio, $3:2:1$, then drew our attention. One possible explanation was that the simulated spectrum for Site **2** was actually a combination of two (or even more) sites. If this is true, however, it is necessary to find a way to distinguish the two (or more) cases.

This was done in the following manner. First, the average frequency shift was examined at each MC move. Unfortunately, these average values showed no obvious features that demonstrated that the "Site **2**" spectrum was due to more than one type of vacancy. We then examined the *maximum separation among the three ν_3 peaks* during the simulation, and obtained the results shown in Fig. 5.15. From Fig. 5.15, one can see that these peak separation values are distributed between two distinct sets. This figure implies that "Site **2**" is indeed composed of two different types of vacancy. Sorting these points into two groups based on the maximum peak separations yielded the spectra shown in Figs. 5.16 and 5.17. Fitting each of these spectra to a sum of Gaussians using the non-linear least-squares techniques described above yielded the results shown in Tables 5.14 and 5.15, respectively. The fitting results thus proved that the "Site **2**" spectrum of Fig. 5.5 is actually the combination of Site **2a**, for which the area ratio is $2:1$ and peak splitting is about 1.6 cm^{-1}, and Site **2b**, for which the area ratio is $1:2$ and the peak splitting about 0.7 cm^{-1}. The ratio of the probability of finding Site **2a** *vs.* **2b** is about $1.2:1$. These results appear to indicate that at equilibrium there exist two distinct types of two-atom vacancy sites. A summary of the fitting results for all of the various vacancy site types is represented in Table 5.16.

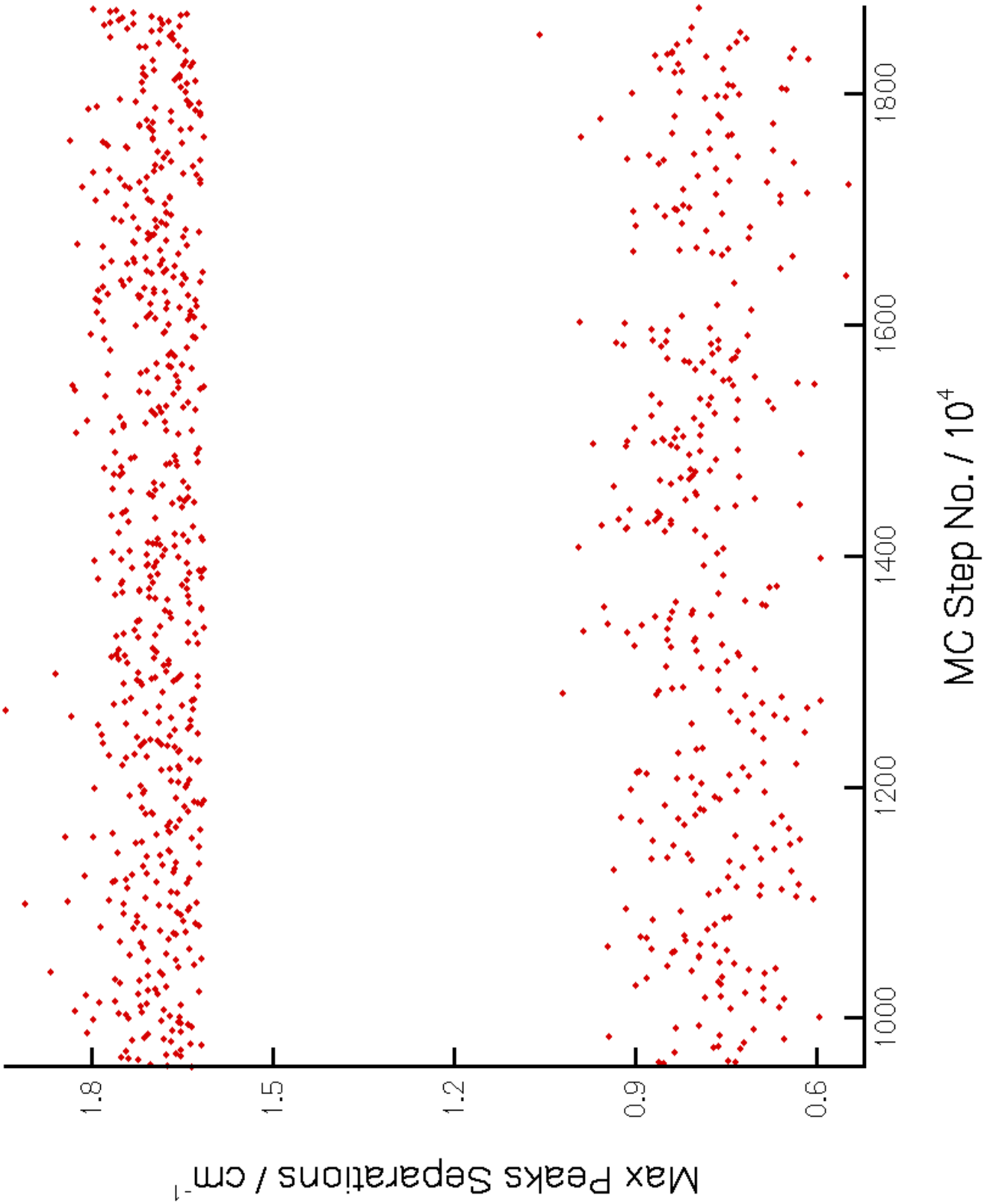

Figure 5.15: Maximum peak separations versus MC moves for Site **2**.

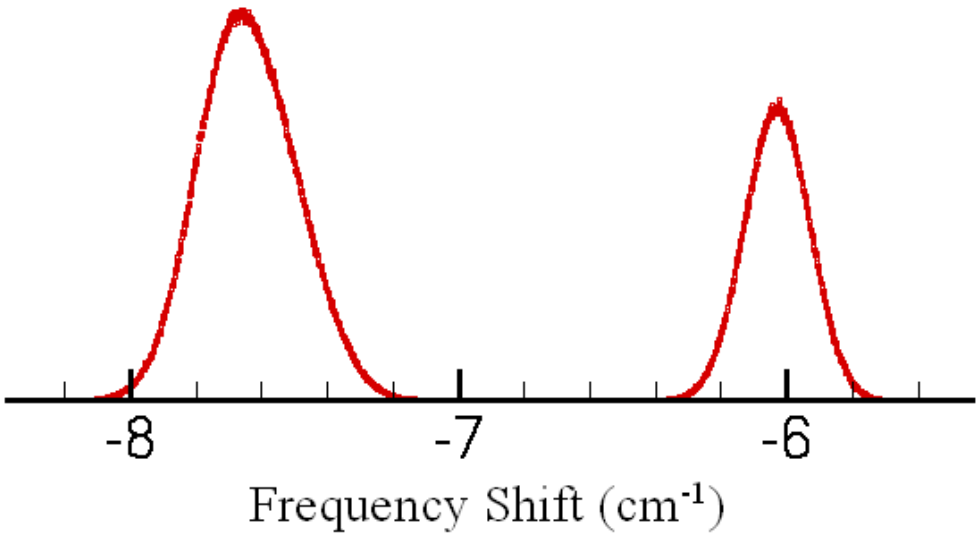

Figure 5.16: Simulated spectrum for Site **2a**.

Table 5.14: Non-linear least-squares fitting results for Site **2a**. The upper part is the results for fitting with no constraints, while the lower one is that for fitting with peak area ratio fixed to be 2 : 1

No constraints				DSE = 0.2201
Peak	Type	Parameter	Value	Uncertainty
1	Gaussian	position	-7.6471	0.0003
		width	0.3525	0.0006
		height	21.42	0.03
2	Gaussian	position	-6.0297	0.0003
		width	0.2333	0.0007
		height	16.14	0.04
Area ratio 2:1				DSE = 0.2201
Peak	Type	Parameter	Value	Uncertainty
1	Gaussian	position	-7.6471	0.0003
		width	0.3523	0.0006
		height	21.42	0.03
2	Gaussian	position	-6.0297	0.0003
		width	0.2336	0.0006
		height	16.15	

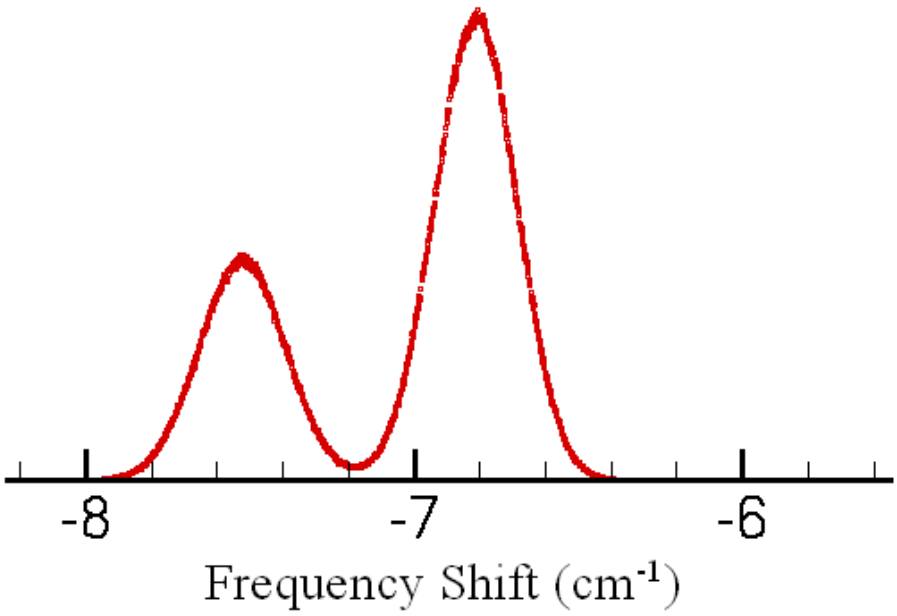

Figure 5.17: Simulated spectrum for Site **2b**.

Table 5.15: Non-linear least-squares fitting results for Site **2b**. The upper part is the results for fitting with no constraints, while the lower one is that for fitting with peak area ratio fixed to be 1 : 2

No constraints				DSE = 0.0765
Peak	Type	Parameter	Value	Uncertainty
1	Gaussian	position	-7.5233	0.0002
		width	0.3094	0.0004
		height	12.16	0.01
2	Gaussian	position	-6.8127	0.0001
		width	0.2946	0.0002
		height	25.54	0.01
Area ratio 1:2				DSE = 0.0764
Peak	Type	Parameter	Value	Uncertainty
1	Gaussian	position	-7.5233	0.0002
		width	0.3094	0.0003
		height	12.16	0.01
2	Gaussian	position	-6.8127	0.0001
		width	0.2946	0.0002
		height	25.54	

Table 5.16: Properties of the simulated spectra for the various vacancy types considered.

Site	No. of peaks	Peak position/cm^{-1}	Peak area
0	1	-7.59	3
1	1	-7.88	1
	2	-7.57	2
2a	1	-7.65	2
	2	-6.02	1
2b	1	-7.52	1
	2	-6.80	2
3a	1	-6.74	1
	2	-6.23	2
3b	1	-7.61	1
	2	-7.26	1
	3	-6.02	1
4a/b/d	1	-5.90	3
4c	1	-6.31	1
	2	-5.48	2
5a/b	1	-5.68	2
	2	-5.35	1
5c	1	-7.30	1
	2	-5.70	2
5d	1	-5.37	3
6a/b	1	-5.50	1
	2	-5.11	2
6c	1	-5.44	2
	2	-4.83	1
6d	1	-5.13	3

5.3 Energies for different sites

Table 5.17 represents the potential energies for different sites considered in this project. The second column of this table shows the total potential energy for the interstitial and vacancy sites in a pure argon system. The third column shows the total potential energy for the interstitial and vacancy sites with an SF_6 molecule in the matrix. The fourth column illustrates the difference ΔE_1 between the second and the third columns. The fifth column shows the value of ΔE_2 ($= \Delta E_1 - \Delta E_1\,(\min)$). The sixth column shows the sum of the SF_6−{Ar matrix} potential energy for the initial configuration of each site and the seventh column shows the energy for the relaxed configuration at each site. The eighth column shows the final SF_6−{Ar matrix} potential energy difference for each site relative to that of Site **0**.

Examining the total potential energy for each site in a pure argon system, one sees that as the size of the vacancy increases its total potential energy also increases. The same trend is observed for the total

Table 5.17: Energies for different sites.

	Total potential energy / eV				SF_6-matrix energy / eV		
	Pure Ar	With SF_6	Difference		Total E $_{SF_6-Ar}$		Difference
Site	E_{tot}	E'_{tot}	ΔE_1 [a]	ΔE_2 [b]	Initial	Relaxed	ΔE_3 [c]
0	-126.36	-125.50(2)[d]	0.86	0.50	90.446	-0.407(3)[d]	0
1	-126.16	-125.56(1)	0.60	0.24	1.140	-0.363(4)	0.044
2a	-125.98	-125.10(6)	0.88	0.52	5.713	-0.369(2)	0.038
2b	-125.98	-125.25(5)	0.73	0.37	5.713	-0.379(2)	0.028
3a	-125.81	-125.31(1)	0.50	0.14	3.641	-0.369(1)	0.038
3b	-125.78	-125.25(2)	0.53	0.17	0.706	-0.348(4)	0.059
4a	-125.65	-125.27(2)	0.38	0.02	-0.353	-0.386(1)	0.021
4b	-125.62	-125.15(1)	0.47	0.11	1.755	-0.365(3)	0.042
4c	-125.64	-125.19(1)	0.45	0.09	1.531	-0.348(2)	0.059
4d	-125.62	-125.26(1)	0.36	0	37.852	-0.385(2)	0.022
5a	-125.48	-125.02(2)	0.46	0.10	-0.206	-0.366(2)	0.041
5b	-125.48	-125.04(1)	0.44	0.08	-8.017	-0.369(1)	0.038
5c	-125.44	-124.93(2)	0.51	0.15	0.427	-0.336(2)	0.071
5d	-125.48	-125.00(2)	0.48	0.12	2.168	-0.340(2)	0.067
6a	-125.32	-124.88(1)	0.44	0.08	-0.273	-0.349(2)	0.058
6b	-125.28	-124.78(2)	0.50	0.14	0.491	-0.317(2)	0.090
6c	-125.31	-124.88(1)	0.43	0.07	0.946	-0.362(2)	0.045
6d	-125.33	-124.91(1)	0.42	0.06	-0.304	-0.353(2)	0.054

[a] $\Delta E_1 \equiv E_{tot} - E'_{tot}$
[b] $\Delta E_2 \equiv \Delta E_1 - \Delta E_1\,(\text{min}) = \Delta E_1 - \Delta E_1\,(\mathbf{4d})$
[c] $\Delta E_3 \equiv E_{SF_6-Ar} - E_{SF_6-Ar}\,(\text{min}) = E_{SF_6-Ar} - E_{SF_6-Ar}\,(\mathbf{0})$
[d] Numbers in parenthesis are uncertainties, defined as $u = \sqrt{\left|\overline{E^2} - \overline{E}^2\right|}$.

potential energy for each site with an SF_6 molecule in the matrix. However, no clear trend could be found for the total SF_6-{Ar matrix} potential energy. The potential energy differences shown in column four decrease as the size of the vacancy increases. This is because for larger sites, the interaction between the SF_6 molecule and the argon atoms are weaker, leading to a smaller difference between the total potential energy for a pure argon system and that for a system containing an SF_6 molecule.

One might expect that $p = \exp(-\Delta E_i / kT)$ ($i = 1,\ 2,$ or 3) would indicate the relative stability of the various sites. However, we found that the magnitudes of most of the energy differences ΔE_i ($i = 1,\ 2,$ or 3) were quite large compared with kT, 8.6×10^{-4} eV, resulting in quite small p values. This indicates that the various sites cannot be in equilibrium, otherwise the site stability would be determined by the corresponding p value. We do not yet understand how to relate these relative energies to the observation that the experimental spectrum shows presence of multiple sites.

Chapter 6

Fitting to the experimental spectrum

Figure 6.1 shows the experimental spectrum for SF_6 in Ar at a concentration ratio of $Ar/SF_6 = 10\,000$, taken from Ref. [8]. This figure shows an unexpectedly large amount of structure, with 9-11 observed peaks. The major goal of this project is to attempt to explain quantitatively the high-resolution spectrum of SF_6 in an argon matrix. Now that the spectra for a set of vacancies have been obtained, one can fit the experimental spectrum to a sum of these simulated spectra, utilizing non-linear least-squares fit methods.

6.1 Representation of the experimental spectrum

The experimental spectrum has peaks with Lorentzian line shapes, due to the homogeneous "pressure" broadening caused by the perturbing atoms [9]. Because of the stochastic averaging associated with the Metropolis Monte Carlo simulation, which reproduces the Boltzmann distribution, the simulated spectra have Gaussian line shapes. The IDID model can predict the frequency shifts for the ν_3 vibrational band of SF_6 in an argon matrix, but it does not consider any lifetime broadening factors. Thus, although the line shapes are different, one may still utilize the peak positions and peak heights from the simulated spectra to reproduce the experimental spectra. Therefore, Lorentzian spectra for all the site types are generated using the peak positions and relative peak heights of the simulated results from Table 5.16 and all the peak widths are set to be $0.07\,cm^{-1}$ which is the average width of the experimental spectral peaks (See Table 6.1). The Lorentzian spectra are illustrated in Fig. 6.2.

Before this simulated spectrum could be fitted to the experimental one, the latter must be digitized. Unfortunately, no digital experimental spectrum could be obtained from Swanson and Jones. However, information about the peaks given in Ref. [3] is listed in Table 6.1. Using the data from the table and

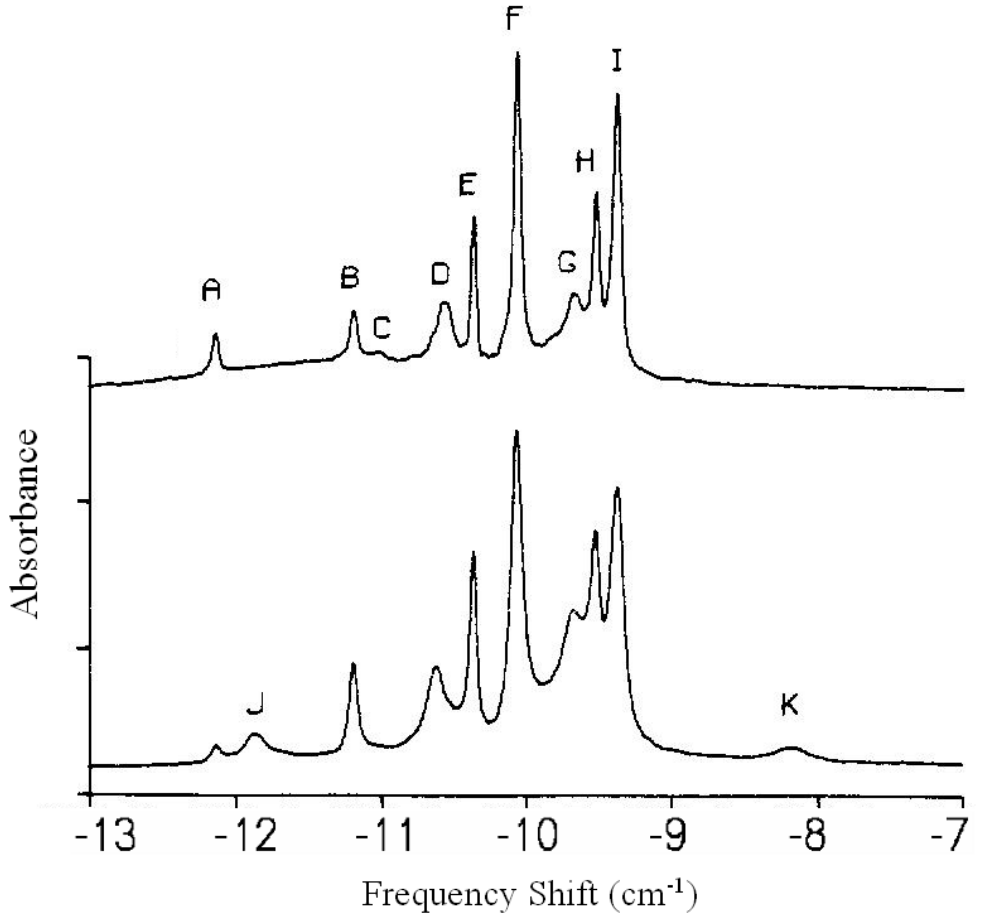

Figure 6.1: ν_3 absorption spectrum at $T = 10\,K$ for $Ar/SF_6 = 10\,000$. *Lower:* unannealed. *Upper:* after being annealed by heating to 30 K [8].

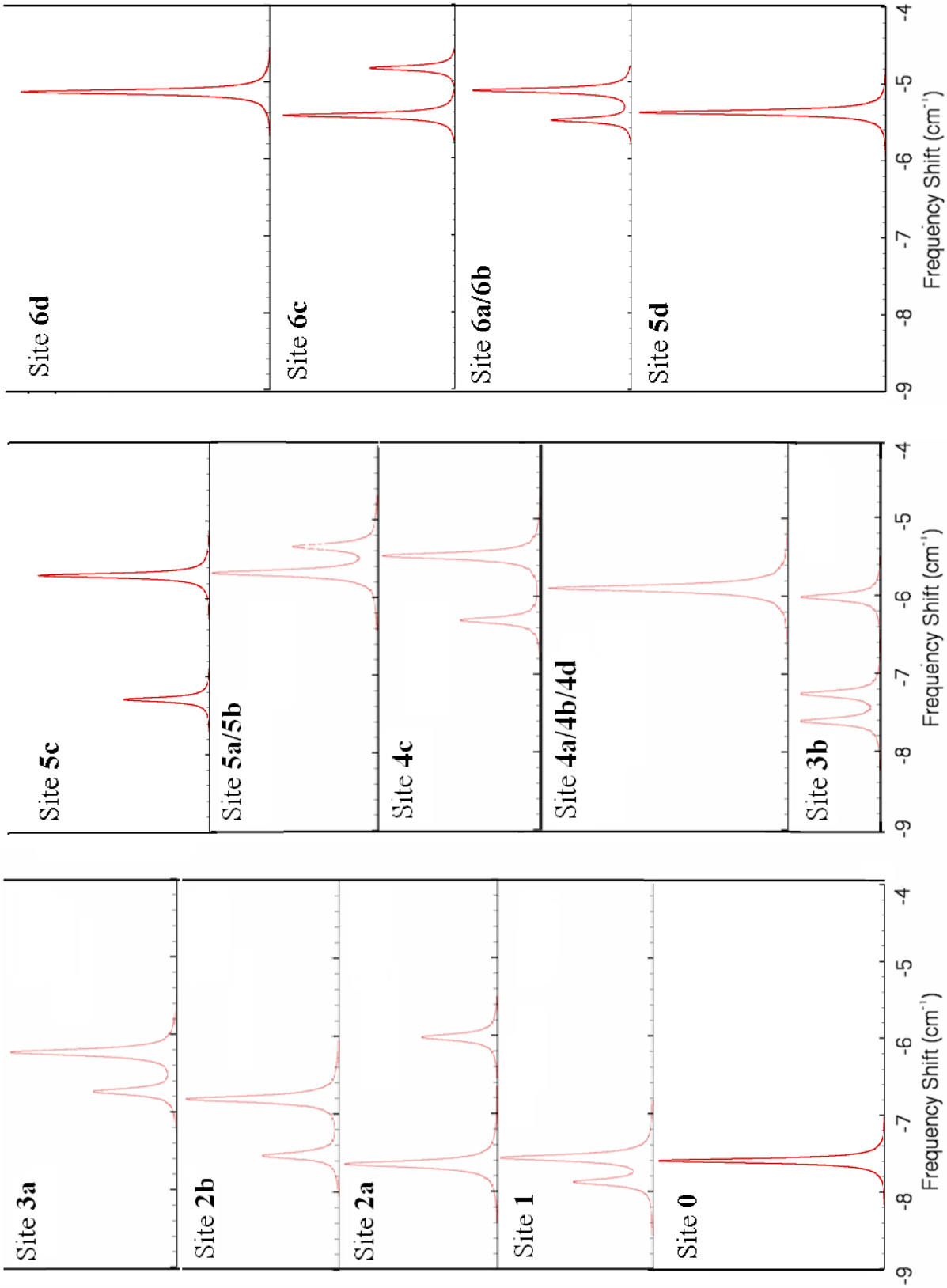

Figure 6.2: Lorentzian spectra generated from the peak positions and peak heights of the simulated results.

Table 6.1: Frequencies and FWHM for ν_3 peaks of SF_6 in argon: 1/10 000 (From Ref. [3])

Peak	FWHM / cm^{-1}	T = 10 K ν / cm^{-1}	T = 30 K ν / cm^{-1}	Height[a] / Arbitrary Units
A	0.05[b]	935.857[c]	936.057	0.35
B	0.08	936.806	936.975	0.52
C	0.12	936.993	···	0.10
D	d	937.416	936.555	0.65
E	0.03	937.631	937.834	1.35
F	0.06	937.930	938.073	3.00
G	0.10	938.321	938.347	0.75
H	0.04	938.475	···	1.50
I	0.07	938.617	938.645	2.70

[a] The values in this column were obtained from UNGRAPH, representing the peak height of the corresponding Lorentzian functions.
[b] Full width at half maximum, estimated by deconvolution from the observed spectrum and instrumental line shape.
[c] Uncertainty of frequencies is $\pm 0.005\,cm^{-1}$.
[d] This is a composite of at least two peaks [3].

those from the program UNGRAPH, which can roughly create digital data from a scanned picture, a new "experimental" spectrum was then generated, and is illustrated by the solid curve in the upper segment of Fig. 6.3. The dotted curve in Fig. 6.3 is made up of points obtained from a scanned experimental spectrum using UNGRAPH. It is clear that the new "experimental" spectrum, which is a sum of Lorentzian functions, does not reproduce the experimental spectrum very well, with somewhat large differences in peak heights between these two curves, especially in the region from 935.3 cm^{-1} to 937.6 cm^{-1}. Therefore, an "asymmetric Lorentzian" baseline was introduced to diminish these differences. This "asymmetric Lorentzian" baseline is defined by a peak located at 937.8 cm^{-1}, its left FWHM being 3.0 cm^{-1} and right one being 1.7 cm^{-1}; it is illustrated by the dashed curve in Fig. 6.4. The "experimental spectrum" with the baseline added is illustrated by the solid curve in the lower segment of Fig. 6.3, and it fits the scanned spectrum fairly well. It appears that one shoulder between peaks F and G cannot be reproduced by this new "experimental spectrum". This may reflect the fact that there is an additional peak there which Swanson and Jones were unable to isolate. Our simulation, in fact, predicts the presence of weak peaks in this region (see Sec. 6.3 for more details).

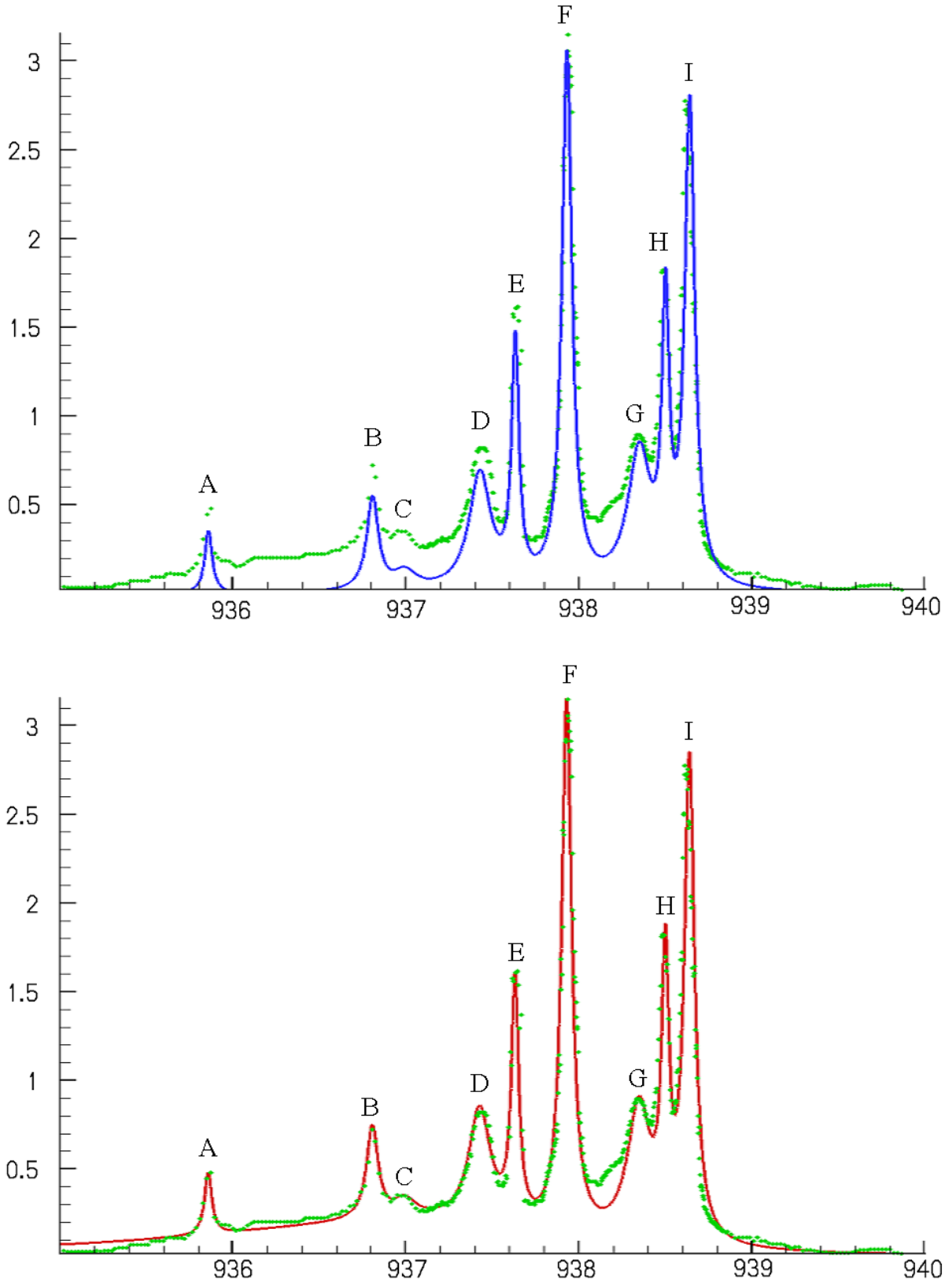

Figure 6.3: Dotted curves: scanned experimental spectrum. Solid curves: Lorentzians generated from the data of Table 6.1. Upper: without a baseline. Lower: with an "asymmetric Lorentzian" baseline added.

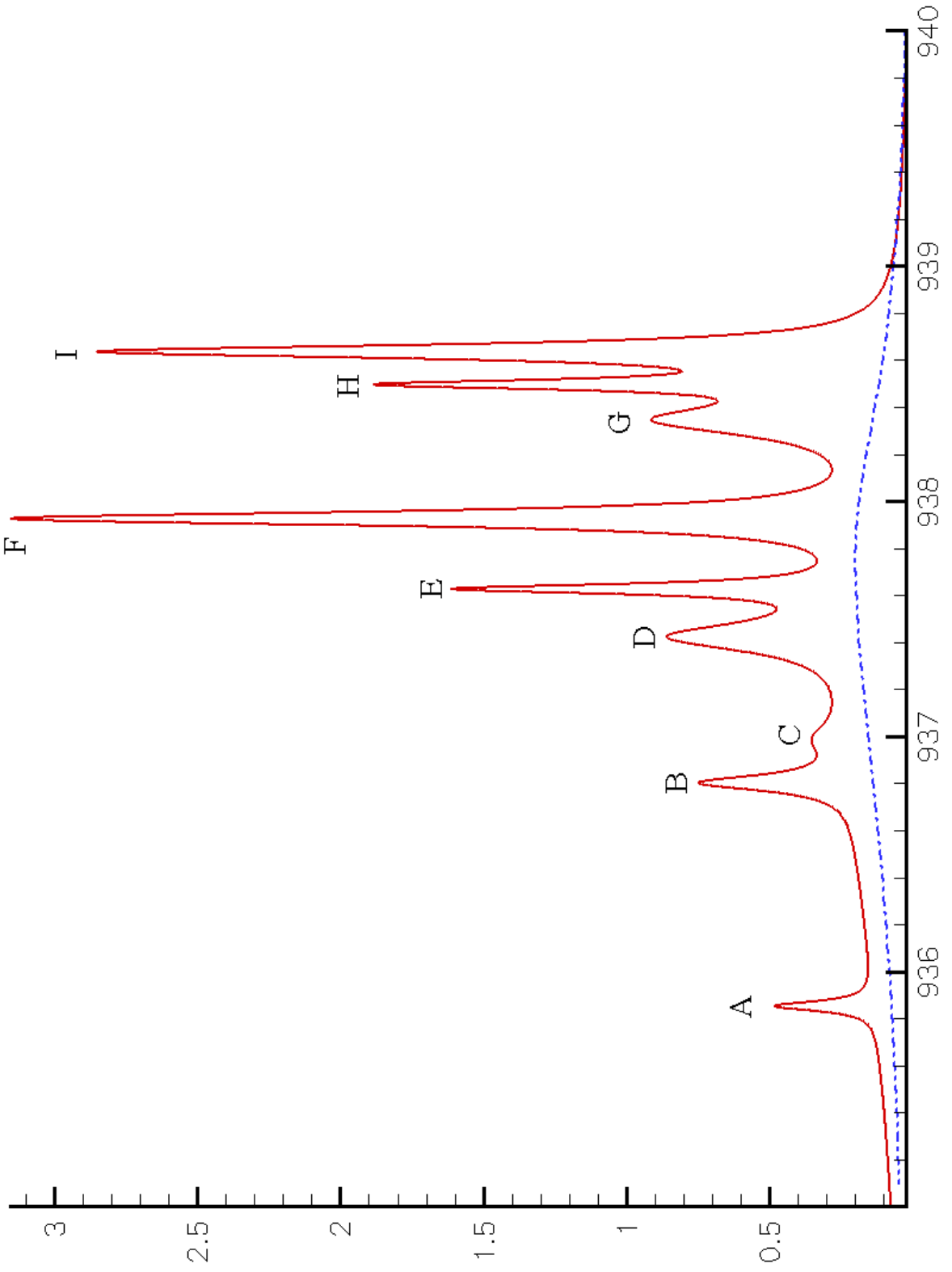

Figure 6.4: New "experimental" spectrum generated from the data of Table 6.1 and those from UNGRAPH. The dashed line is the "experimental" background.

6.2 Fitting of the simulated spectra

Comparing the simulated spectra of Fig. 6.2 with the experimental one of Fig. 6.1, one sees that the simulated spectral peaks are mostly located from -5 cm^{-1} to -8 cm^{-1}, while the experimental ones range from -9.5 cm^{-1} to -12.1 cm^{-1}. This difference reflects the fact that the IDID model is not perfect. For example, neither the instantaneous-dipole/induced-quadrupole interaction nor changes in the repulsive short-range SF_6-Ar potential associated with vibrational stretching have been taken into account, and the SF_6 is treated as a rigid molecule during the simulation. On the assumption that use of a better frequency shift model would yield much the same pattern and relative peak positions, the effect of these missing terms will be approximated here by an empirical scaling and shifting of the frequency scale in the simulated spectrum of Fig. 6.2,

$$\Delta\nu_{\rm exp} \;=\; A\,\Delta\nu_{\rm sim} \;+\; B \tag{6.1}$$

where $\Delta\nu_{\rm exp}$ and $\Delta\nu_{\rm sim}$ are the frequency shifts in the experiment and in the simulations, respectively.

Taking account of this empirical scaling and shifting and the different population of different types of vacancy sites, we assume that the experimental spectrum may be represented in the following manner:

$$S_{\rm tot} \;=\; p_1\,S_1(\nu,\Gamma_1) \;+\; p_{2a}\,S_{2a}(\nu,\Gamma_{2a}) \;+\; p_{2b}\,S_{2b}(\nu,\Gamma_{2b}) \;+\; \cdots \tag{6.2}$$

Here, $S_{\rm tot}$ is the overall simulated spectrum which is to be compared with the experimental spectrum, S_i ($i \;=\; 1, 2a, 2b, \cdots$) is the simulated spectrum for Site **i**, p_i ($i \;=\; 1, 2a, 2b, \cdots$) is the corresponding population (or weight) in the total spectrum, and Γ_i is the corresponding FWHM. A non-linear least-squares fit to the experimental spectrum is used to determine the parameters ($A,\ B,\ \{p_i\},\ \{\Gamma_i\}$) in Eqs. 6.1 and 6.2.

After the experimental spectrum was digitized, it could be fitted to Eq. 6.2, using a non-linear least-squares technique. As described before, the partial derivative of the experimental spectrum with respect to the fitting parameters are required when performing this fit. From Eq. 6.2, one may obtain these derivatives

$$\frac{\partial S_{\rm tot}}{\partial p_i} \;=\; \frac{\partial\left(\sum_i p_i\,S_i\right)}{\partial p_i} \;=\; S_i \tag{6.3}$$

$$\frac{\partial S_{\rm tot}}{\partial \Gamma_i} \;=\; \frac{\partial\left(\sum_i p_i\,S_i\right)}{\partial \Gamma_i} \;=\; p_i\,\frac{\partial S_i}{\Gamma_i} \tag{6.4}$$

$$\frac{\partial S_{\rm tot}}{\partial A} \;=\; \frac{\partial\left(\sum_i p_i\,S_i\right)}{\partial A} \;=\; \sum_i p_i\,\frac{\partial S_i}{\partial A} \tag{6.5}$$

$$\frac{\partial S_{\rm tot}}{\partial B} \;=\; \frac{\partial\left(\sum_i p_i\,S_i\right)}{\partial B} \;=\; \sum_i p_i\,\frac{\partial S_i}{\partial B} \tag{6.6}$$

Table 6.2: Results of fitting experimental spectrum to a sum of simulated spectra. Large vacancy sites were neglected due to instability. Numbers in parenthesis are 95% confidence limit uncertainties in the last digit shown.

Site	**1**	**2a**	**2b**	**3a**	**3b**	**4a/4b/4d**	**4c**	**5a/5b**
Relative population	2.0(3)	0.04(1)	2.7(3)	5.8(3)	1.4(5)	1.8(2)	16.2(3)	4.7(3)
A	0.878(2)							
B	−4.55(1)							

6.3 Results and discussion

If the FWHM of the spectrum associated with each type of vacancy site is free to vary, there will be $(2\,N_{site} + 2)$ parameters to be determined. Since this fit is non-linear, it could be difficult to determine the optimum values for so many parameters. Therefore, the FWHM for each vacancy site was held at a constant value of 0.07 cm^{-1}, which is the average FWHM for all the peaks in Table 6.1. Since a non-linear least-squares fit may converge on different local minima due to different choices of initial trial parameter values, it is important to sample the parameter space thoroughly so that "good" trial values may be obtained. This was achieved by taking the following two steps. The first step was to perform linear least-squares fits, with the parameters A and B being held constant. One was able to attain a qualitative indication of combinations of A and B that gave local minima. By freeing up A and B, the second step was to perform non-linear least-squares fits with the trial values set to be close to those different local minima. These non-linear fits would determine the various local minima in the $\{A,\ B\}$ domain, and by comparing the values of the DSE's, one could find the global minima of the non-linear least-squares fit. Table 6.2 and Fig. 6.5 illustrate the results of fitting our version of the "experimental" spectrum (upper segment) to a sum of the simulated spectra, with the FWHM of each site fixed at a constant of 0.07 cm^{-1}. The lower segment of Fig. 6.5 shows the curve generated from the fit, in which the labels illustrate the peak assignments, e.g. 3b(2) means the second peak of the simulated spectrum for Site **3b**. Note that only Sites **1**, **2a**, **2b**, **3a**, **3b**, **4a/b/d**, **4c** and **5a/b** were considered here.

Comparing the upper and lower segments of Fig. 6.5, one can see that the main patterns of the experimental spectrum are successfully reproduced, and the peaks are successfully assigned to particular lattice vacancy types. The shoulder between peaks F and G, although absent in the "experimental" spectrum of Fig. 6.4, are reproduced by peaks 2a(2) and 3b(3). Peak A in the experimental spectrum is not reproduced however. We conclude that it may be due to the existence of SF_6 dimers or to SF_6 located at some lattice discontinuity site. Moreover, since the experimental spectrum shows no analog of 1(1) and the initial ge-

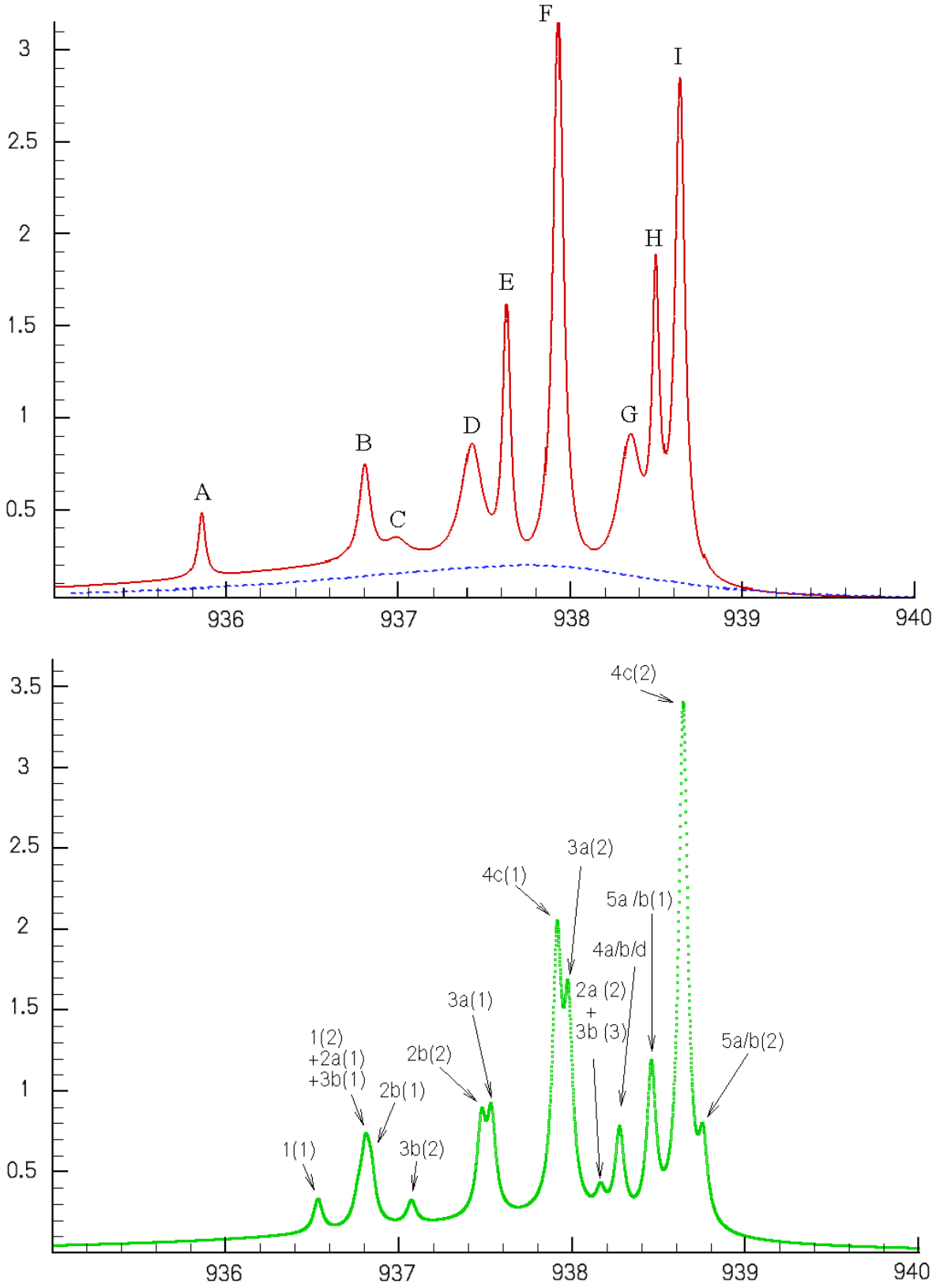

Figure 6.5: Upper: experimental spectrum. Lower: spectrum generated from the fitting results represented in Table 6.2. The peaks are labelled by different sites. For example, 3b(2) denotes the 2nd peak of Site **3b**.

ometry of Site **1** is expected to be heavily crowded, perhaps Site **1** should not be included. It may appear that to determine the values of 10 parameters by fitting 9 peaks is quite flexible. However, this is not true. Note Fig. 6.2 shows that relative positions of multiple peaks for a particular site, and positions of peaks for different sites are fixed.

It is clear, however, that this initial fit is not ideal. Possible reasons are:

1. The SF_6-Ar pair potential is not perfect for reproducing the position and orientation of the SF_6 molecule in the various matrix sites.

2. The IDID model is not perfect. For instance, no instantaneous-dipole/induced-quadrupole interactions are taken into account.

3. The SF_6 molecule is treated as a rigid molecule in the MC simulation.

For the above reasons, some modifications may be necessary. Assuming that the shortcomings of our frequency shift model are adequately accounted for by the frequency-shift scaling and shifting of Eq. 6.1, we will examine the effect of *ad hoc* changes to the SF_6-Ar pair potential. By modify the SF_6-Ar potential curve, the effect on the resulting average lattice structure may change the relative peak positions enough to give better agreement with experiment. The first type of modification consists of multiplying the strength of the SF_6-Ar pair potential by a factor of 1.1, while in the second, the SF_6-Ar potential is displaced to smaller distance by 0.1 Å. These two types trial modifications may be written as

$$\widetilde{V}_{SF_6-Ar} = V_{SF_6-Ar} \times 1.1 \tag{6.7}$$

$$\widetilde{R}_{SF_6-Ar} = R_{SF_6-Ar} - 0.1 \tag{6.8}$$

Comparison of columns 3 and 5 in Table 6.3 shows that the energy scaling of the SF_6-Ar pair potential, shown as Eq. 6.7 did not cause much change in the relative peak positions. Thus, this modification is expected to yield the same fitting results as did the original SF_6-Ar pair potential model. However, the second modification, shown as Eq. 6.8, did change the relative peak positions significantly. The "experimental" spectrum was then fit to a sum of the simulated spectra with these new peak positions. The results of this fit are listed in the last column of Table 6.3, and the spectrum generated using these fitting results is illustrated in Fig. 6.6.

The spectrum obtained by using this new potential model match the simulated one somewhat better than that obtained using the original potential function. For example, peaks 4c(1) and 3a(2) are closer

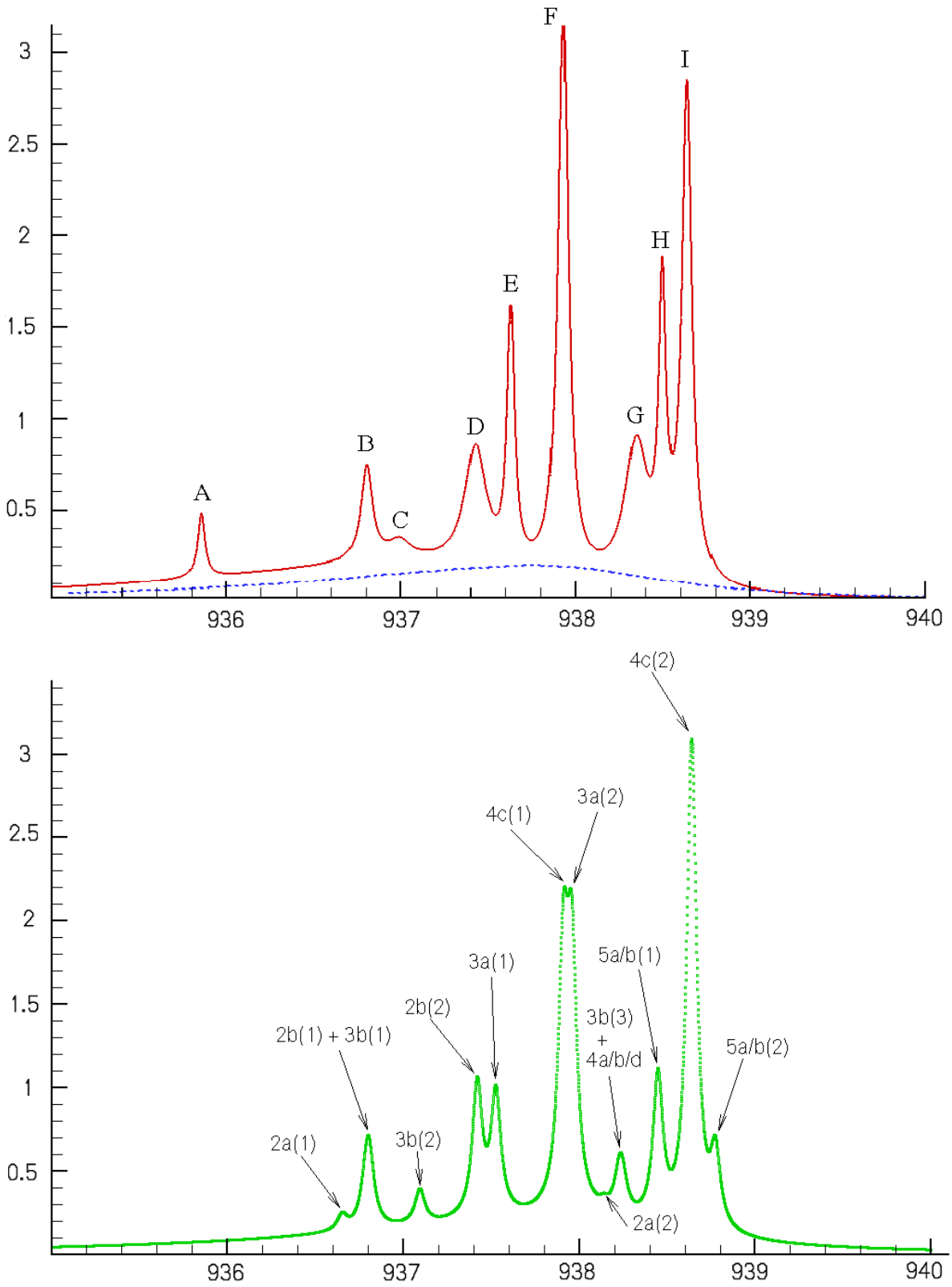

Figure 6.6: Upper: experimental spectrum. Lower: spectrum generated from the fitting results represented in Table 6.3. The peaks are labelled by different sites.

Table 6.3: Peaks for different SF_6-Ar potential models

		Original Model		$\widetilde{V} = V \times 1.1$	$\widetilde{R} = R - 0.1$	
Site	Peak	Γ (cm^{-1})	Population[a]	Γ (cm^{-1})	Γ (cm^{-1})	Population[b]
1	1	−7.88	2.0(3)[c]	−7.82	−7.56	d
	2	−7.57		−7.51	−7.24	
2a	1	−7.65	0.04	−7.62	−7.41	0.5(3)
	2	−6.02		−6.03	−5.86	
2b	1	−7.52	2.7(3)	−7.49	−7.25	4.0(3)
	2	−6.80		−6.81	−6.61	
3a	1	−6.74	5.8(3)	−6.71	−6.50	7.2(3)
	2	−6.23		−6.25	−6.05	
3b	1	−7.61	1.4(5)	−7.56	−7.27	2.0(4)
	2	−7.26		−7.21	−6.95	
	3	−6.02		−5.98	−5.77	
4a/b/d	1	−5.90	1.8(2)	−5.91	−5.75	0.6(2)
4c	1	−6.31	16.2(3)	−6.30	−6.10	14.6(3)
	2	−5.48		−5.49	−5.34	
5a/b	1	−5.68	4.7(3)	−5.70	−5.54	4.4(3)
	2	−5.35		−5.37	−5.20	

[a] This fit gives rise to $A = 0.878(2),\ B = -4.55(1)$.
[b] This fit gives rise to $A = 0.960(2),\ B = -4.24(1)$.
[c] Numbers in parenthesis are 95% confidence limit uncertainties.
[d] Site **1** was omitted in this fit.

together in Fig. 6.6 than they are in Fig. 6.5, resulting in a better fit to Peak F in the experimental spectrum. Peak 2b(2) and 3a(1) are more separated in Fig. 6.6 than they are in Fig. 6.5, giving rise to a better representation of Peaks D and E in the experimental spectrum. Moreover, the quality of fit, represented by $\bar{\sigma}_f$, is about ten percent better than the previous fit. Although this new model still did not give us perfect fitting results, it did improve the fit and provided suggestions for possible improvements to the SF_6-Ar pair potential.

Chapter 7

Summary and Conclusions

7.1 Summary

The ν_3 vibrational band of a free SF_6 molecule is triply degenerate. When an SF_6 molecule is trapped in an argon matrix, its vibrational frequencies are shifted, and if the perturbing environment is not spherically symmetric, the three-component ν_3 vibrational band will give rise to three distinct spectral peaks. However, the experimental spectrum of SF_6 in an argon matrix showed nine to eleven peaks. To our knowledge, no quantitative explanation of the fine structure of this spectrum has been proposed prior to this study. Employing a combination of IDID model developed by Eichenauer and Le Roy and Metropolis Monte Carlo simulations, this thesis has semi-quantitatively explained the experimental spectrum and provided assignments for the fine structure appearing there. Table 7.1 summarizes our assignments of the experimental spectral peaks to particular lattice sites.

In our analysis, SF_6 is treated as a three-dimensional harmonic oscillator. The instantaneous dipole

Table 7.1: Experimental spectral peak assignments

Peak	Assignments
A	–
B	2b(1), 3b(1)
C	3b(2)
D	2b(2)
E	3a(1)
F	3a(2), 4c(1)
G	3b(3), 4a/4b
H	5a(1)
I	4c(2)

arises from the ν_3 intramolecular vibration of SF_6 and its electric field induces dipole moments on surrounding argon atoms. The interaction between the instantaneous dipole and the induced dipole was assumed to provide the dominant contribution to the frequency shifts.

The anisotropic model developed by Pack *et al.* [45] was employed to represent the SF_6-Ar interaction potential. This model utilizes a Morse-Morse-Morse-Spline-Van der Waals radial form and reproduces the anisotropy by allowing the parameters of this radial potential to depend on the relative orientation of argon and the SF_6. For the Ar−Ar pairwise potential, a simple model was utilized to save computing time. The fact that both the SF_6-Ar and the Ar−Ar interaction potentials are reasonably well known is important to this simulation.

At low temperature, argon atoms have a perfect face-centered cubic configuration. Since an SF_6 molecule is much larger than an argon atom, it would appear that the way to readily admit the SF_6 molecule into the argon matrix is through the removal of one or more argon atoms. The vibrations of SF_6 in smaller vacancy sites are expected to be more restricted, causing the site to relax to form a more relaxed conformation. However, as the number of removed argon atoms increases, the substitutional site is expected to become increasingly unstable. For highly symmetric sites, the perturbations to the chromophore are expected to be symmetric, and not to split the ν_3 vibrational band. For planar sites, one may expect the vibrations within the plane to be doubly degenerate, while those perpendicular to the plane to be singly degenerate.

For any given SF_6-Ar arrangement, the frequency shifts of the ν_3 band of SF_6 can be calculated using the perturbation model and potential functions. At most temperatures, the number of energetically possible arrangements contributing to the thermal average is quite large. Thus, the Metropolis Monte Carlo procedure was utilized for averaging over the contributions. The relaxation of an argon matrix hosting an SF_6 molecule was simulated using the MC method. The SF_6 molecule is initially put at the center of the chosen vacancy site, and with about 1 500 argon atoms surrounding SF_6. During the simulation, the SF_6 molecule is allowed to rotate and translate, and nearby argon atoms are allowed to translate while the outer ones are frozen in perfect FCC configuration.

The ν_3 frequency shift distributions were then obtained by collecting the values for the frequency shifts after the system reached its equilibrium. As one finds in the simulated results, the ν_3 band of SF_6 in argon matrix are split into up to three components. By fitting these simulated spectra to a sum of Gaussian functions, the area ratio are proved to be 1 : 2 or 2 : 1 for the two-component case, and 1 : 1 : 1 for the three-component case. It is also clear that the simulated spectrum for a larger site has a smaller frequency

shift.

Due to the stochastic averaging procedure associated with the Metropolis MC method, the simulated spectra have Gaussian line shapes. In contrast, the experimental spectra have Lorentzian line shapes, due to the homogeneous "pressure" broadening caused by the argon atoms. Thus, Lorentzian spectra with the peak positions and area ratios obtained from the simulation results are generated.

Since the frequency shift model is not perfect, a scaling and shifting procedure is employed for mapping the domain of the simulated spectra onto that of the experimental spectrum. After utilizing this mapping, the experimental spectrum is fitted to a sum of the simulated Lorentzian spectra, using non-linear least-squares techniques. The experimental spectrum of the ν_3 vibrational band for SF_6 in argon matrix is successfully reproduced by combining the simulated spectra, and the peaks are assigned to different types of vacancy sites. Thus, the fine structure in experimental spectrum is assigned to peaks associated with particular vacancy sites.

7.2 Future work

The *ad hoc* scaling and shifting of frequency shifts show that the IDID model is not perfect. One may consider the instantaneous-dipole/induced-quadrupole interaction when calculating the frequency shifts. We would not expect to use the fitting results to determine the SF_6-Ar potential energy surface, but the modification shows that some changes in the pairwise potential can affect the resulting spectra. Moreover, the effect of the potential energy differences between every site may need to be studied.

Bibliography

[1] E. Whittle, D. A. Dows, and G. C. Pimentel, J. Chem. Phys. **22**, 1943 (1954).

[2] I. Norman and G. Porter, Nature **174**, 508 (1954).

[3] B. I. Swanson and L. H. Jones, in *Vibrational Spectra and Structure*, edited by J. R. Durig (Elsevier-Amsterdam-Oxford-New York, 1983), vol. 12, chap. 1, pp. 1–67.

[4] G. N. Lewis, D. Lipkin, and T. T. Magel, J. Am. Chem. Soc. **63**, 3005 (1941).

[5] G. N. Lewis and D. Lipkin, J. Am. Chem. Soc. **64**, 2801 (1942).

[6] W. E. Klotzbucher and G. A. Ozin, Inorg. Chem. **19**, 3767 (1980).

[7] B. W. Keelan and L. Andrews, J. Am. Chem. Soc. **103**, 829 (1981).

[8] B. I. Swanson and L. H. Jones, J. Chem. Phys. **74**, 3205 (1981).

[9] B. I. Swanson, L. H. Jones, S. A. Ekberg, and H. A. Fry, Chem. Phys. Lett. **126**, 455 (1986).

[10] L. H. Jones, B. I. Swanson, and S. A. Ekberg, Chem. Phys. Lett. **68**, 499 (1979).

[11] B. I. Swanson and L. H. Jones, Chem. Phys. Lett. **80**, 51 (1981).

[12] B. I. Swanson and L. H. Jones, J. Chem. Phys. **73**, 986 (1980).

[13] L. H. Jones and B. I. Swanson, J. Chem. Phys. **79**, 1516 (1983).

[14] H. E. Hallam, in *Vibrational Spectroscopy of Trapped Species*, edited by H. E. Hallam (Wiley and Sons, New York, 1973), chap. 3.

[15] A. J. Barnes, in *Vibrational Spectroscopy of Trapped Species*, edited by H. E. Hallam (Wiley and Sons, New York, 1973), chap. 4.

[16] R. N. Perutz and J. J. Turner, J. Am. Chem. Soc. **97**, 4791 (1975).

[17] B. Davies, A. McNeish, M. Poliakoff, M. Tranquille, and J. J. Turner, Chem. Phys. Lett. **52**, 477 (1977).

[18] M. Dubs and H. H. Gunthard, Chem. Phys. Lett. **47**, 421 (1977).

[19] M. Dubs and H. H. Gunthard, Chem. Phys. Lett. **64**, 105 (1979).

[20] N. J. Bristow, M. Poliakoff, P. B. Davies, and P. A. Hamilton, Chem. Phys. Lett. **84**, 462 (1981).

[21] C. W. F. T. Ĥistorius, J. Chem. Phys. **29**, 1328 (1958).

[22] R. S. McDowell and B. J. Krohn, Spectrochimica Acta. **42A**, 371 (1986).

[23] P. F. Bernath, *Spectra of Atoms and Molecules* (Oxford University Press, New York, 2005), 2nd ed.

[24] R. S. McDowell and B. J. Krohn, Spectrochimica Acta. **42A**, 351 (1986).

[25] L. H. Jones, B. I. Swanson, and S. A. Ekberg, Chem. Phys. Lett. **74**, 330 (1980).

[26] B. I. Swanson and L. H. Jones, J. Chem. Phys. **74**, 3216 (1981).

[27] D. Eichenauer and R. J. Le Roy, J. Chem. Phys. **88**, 2898 (1988).

[28] T. E. Gough, D. G. Knight, and G. Scoles, Chem. Phys. Lett. **97**, 155 (1983).

[29] T. E. Gough, M. Mengel, P. A. Rowntree, and G. Scoles, J. Chem. Phys. **83**, 4958 (1985).

[30] R. N. Barnett and K. B. Whaley, J. Chem. Phys. **99**, 9730 (1993).

[31] K. B. Whaley, Int. Rev. Phys. Chem. **13**, 41 (1994).

[32] S. Goyal, D. L. Schutt, and G. Scoles, Phys. Rev. Lett. **69**, 933 (1992).

[33] S. Goyal, D. L. Schutt, and G. Scoles, J. Chem. Phys. **97**, 2236 (1993).

[34] Y. K. Kwon, D. M. Ceperley, and K. B. Whaley, J. Chem. Phys. **104**, 2341 (1996).

[35] D. Blume, M. Lewerenz, F. Huisken, and M. Kaloudis, J. Chem. Phys. **105**, 8666 (1996).

[36] J. P. Toennies and A. F. Vilesov, Ann. Rev. Phys. Chem. **49**, 1 (1998).

[37] C. Callegari, K. K. Lehmann, R. Schmied, and G. Scoles, J. Chem. Phys. **115**, 10090 (2001).

[38] K. Nauta and R. E. Miller, J. Chem. Phys. **115**, 10254 (2001).

[39] R. S. Berry, Chem. Rev. **93**, 2379 (1993).

[40] L. Perera and F. R. Amar, J. Chem. Phys. **93**, 4884 (1990).

[41] S. Goyal, D. L. Schutt, and G. Scoles, J. Chem. Phys. **102**, 2302 (1995).

[42] S. R. Atrill and A. J. Stace, Phys. Chem. Chem. Phys. **2**, 823 (2000).

[43] B. Meyer, *Low Temperature Spectroscopy* (American Elsevier Publishing Company, 1971).

[44] N. Metropolis, A. W. Rosenbluth, M. N. Rosenbluth, A. H. Teller, and E. Teller, J. Chem. Phys. **21**, 1087 (1953).

[45] R. T. Pack, J. J. Valentini, and J. B. Cross, J. Chem. Phys. **77**, 5486 (1982).

[46] D. A. McQuarrie and J. D. Simon, *Physical Chemistry: A Molecular Approach* (University Science Books, Sausalito, California, 1997).

[47] A. Szabo and N. S. Ostlund, *Moden Quantum Chemistry: Introduction to Advanced Electronic Structure Theory* (Dover Publications, Inc., Mineola, New York, 1996), 2nd ed.

[48] R. Shankar, *Principles of Quantum Mechanics* (Kluwer Academic/Plenum Publishers, 1994), 2nd ed.

[49] V. C. Ewing and L. E. Sutton, Trans. Faraday Soc. **59**, 1241 (1963).

[50] D. Eichenauer and R. J. Le Roy, *Monte Carlo Simulation of Structural Properties and Infrared Spectra of SF_6-$(Ar)_n$ Complexes*, Appendix to University of Waterloo Chemical Physics Research Report CP-312 (1987).

[51] R. J. Le Roy and J. M. Hutson, J. Chem. Phys. **86**, 837 (1986).

[52] P. N. Schatz and D. F. Hornig, J. Chem. Phys. **21**, 1516 (1953).

[53] R. R. Teachout and R. T. Pack, At. Data Nu. Data Tables **3**, 195 (1971).

[54] J. A. Courtney and R. L. Armstrong, Can. J. Phys. **50**, 1252 (1972).

[55] P. F. Moulton, D. M. Larsen, J. N. Walpole, and A. Mooradian, Opt. Lett. **1**, 51 (1977).

[56] C. K. N. Patel and R. E. Slusher, Phys. Rev. Lett. **20**, 1087 (1968).

[57] C. C. Jensen, T. G. Anderson, C. Reiser, and J. I. Steinfeld, J. Chem. Phys. **71**, 3648 (1979).

[58] L. Zandee, J. Verberne, and J. Reuss, Chem. Phys. **26**, 1 (1977).

[59] P. Isnard, D. Robert, and L. Galatry, Mol. Phys. **39**, 501 (1980).

[60] P. Isnard, D. Robert, and L. Galatry, Mol. Phys. **43**, 483 (1981).

[61] R. T. Pack, Chem. Phys. Lett. **55**, 197 (1978).

[62] R. T. Pack, J. J. Valentini, C. H. Becker, R. J. Buss, and Y. T. Lee, J. Chem. Phys. **77**, 5475 (1982).

[63] R. A. Aziz and M. J. Slaman, Mol. Phys. **58**, 679 (1986).

[64] D. C. Young, *Computational Chemistry: A Practical Guide for Applying Techniques to Real-World Probelems* (Wiley-Interscience, 2001).

[65] M. P. Allen and D. J. Tildesley, *Computer Simulation of Liquids* (Clarendon Press, Oxford Science Publications, 1987).

[66] G. L. Pollack, Rev. Mod. Phys. **36**, 748 (1964).

[67] M. L. Klein, *Inert Gases: Potentials, Dynamics, and Energy Transfer in Doped Crystals* (Springer-Verlag, Berlin, 1984).

[68] R. H. Petrucci, W. S. Harwood, and F. G. Herring, *General Chemistry: Principles and Modern Applications* (Prentice Hall, New Jersey, 2002), 8th ed.

[69] J. J. Sylvestre, *Simulation of Matrix Shifts: SF_6 in an Ar Lattice*, Chemistry 492 Report (1995).

[70] W. H. Press, S. A. Teukolsky, W. T. Vetterling, and B. P. Flannery, *Numerical Recipes in Fortran 77: The Art of Scientific Computing* (Cambridge [England]; New York, NY, USA: Cambridge University Press, 1992), 2nd ed.

[71] R. J. Le Roy, *A Practical Guide to Least-Squares Fitting*, University of Waterloo Chemical Physics Research Report CP-628 (1997).

[72] R. J. Le Roy, J. Mol. Spectrosc. **191**, 223 (1998).